

EXPERIMENTAL STUDY OF SEPARATED RAMP-INDUCED SHOCK/BOUNDARY-
LAYER INTERACTION WITH UPSTREAM MICRO-VORTEX GENERATOR AT MACH

2.5

by

YUSI SHIH

Presented to the Faculty of the Graduate School of
The University of Texas at Arlington in Partial Fulfillment
of the Requirements
for the Degree of

DOCTOR OF PHILOSOPHY

THE UNIVERSITY OF TEXAS AT ARLINGTON

August 2014

Copyright © by YUSI SHIH

All Rights Reserved



Acknowledgements

This is an exciting moment that I have finished my Ph.D work and dissertation. First of all, tons of appreciations go to my advisor, Dr. Luca Massa. Without his guidance and support in my research, I would never achieve this work. Dr. Massa showed me the fundamental research of aerodynamics, and ignited my enthusiasm towards this fascinating subject. Under his advice, I found fluid mechanics have many similar aspects to theoretical physics. In fact, one story inspires me very much: theoretical physicist Arnold Sommerfeld supervised his Ph.D student, Werner Heisenberg, on his dissertation "On the Stability and Turbulence of Fluid Flow." in the University of Munich in 1923.

Secondly, I am grateful to all of my dissertation committee professors: Dr. Alan Bowling, Dr. Chen Luo, Dr. Daejong Kim, Dr. Donald R. Wilson, Dr. Frank Lu, and Dr. Nomura. Thank you for your advices on my research. These are very treasure to me and help me to think deeper to the subjects. Also, I would like to thank Lanie Gordon and Debi Barton. Lanie is a student employment staff and Debi is a graduate records staff in AE department. They are just like my family members--always give me helps and warm hugs when I need to.

Moreover, I wish to thank my office mates, Esteban and Rahul. It is because of them that we have such a friendly and dynamic office environment. A special thank goes to Kermit Beird and Sam Williams of the MAE Machine Shop, who are highly skilled in machining so many of my parts can be done nicely and quickly.

Finally, I am indebted to my loving family in Taiwan, for their love, constant motivation and encouragement throughout my life.

July 23, 2014

Abstract

EXPERIMENTAL STUDY OF SEPARATED RAMP-INDUCED SHOCK/BOUNDARY-LAYER INTERACTION WITH UPSTREAM MICRO-VORTEX GENERATOR AT MACH 2.5

Yusi Shih, PhD

The University of Texas at Arlington, 2014

Supervising Professor: Luca Massa

Shock wave/boundary layer interactions (SBLIs) are important issues for high-speed vehicles. SBLIs reduce the performance of aerodynamic surfaces and engine inlets, amongst a number of adverse effects. Micro-vortex generators (MVGs) are a flow control method with strong potential to mitigate the effects of SBLI by energizing the boundary layer through momentum transfers from the freestream. They have been implemented in actual configurations at low speeds. The present research includes a combined experimental and theoretical analysis of the evolution of the perturbation downstream the MVG, the formation of vortices, and their interaction with the shock front.

Experiments were performed with a baseline MVG configuration of 90° trailing edge on flat plate, ramp alone, and also with MVG mounted ahead of a 20° ramp. The surface flow visualization and particle image velocimetry (PIV) results are presented; the surface flow visualization shows a substantial suppression of SBLIs. A new method to quantify the effectiveness of the MVG on the shock recompression is presented. Moreover, the PIV results were used as the initial input values for the simulation work.

A theoretical analysis of the interaction of the MVG perturbation with the boundary layer is performed by assuming linear dynamics of the perturbation. The major assumption is that the interaction between MVG perturbation and the shear flow is

affected by transient growth as a result of the non-orthogonality of the linearized Navier-Stokes equations. A new method to perform the projection of the measured perturbation on the continuous modes of the boundary layer is presented. The method takes advantage of the biorthogonality of the direct and adjoint modes. The implementation of such a method using both the Chebyshev polynomials and a shooting algorithm is discussed. The results of the theoretical analysis are encouraging and display a similar trend as the experiments.

Both experimental and theoretical results yield perturbation decay not far downstream from the MVG: about 72 mm for experiments, and about 95 mm for simulation. The experiments display two distinguishable growths downstream of MVG, while the simulation predicted one small growth at the very beginning. Both works show trends that agree well with each other.

Table of Contents

Acknowledgements	iii
Abstract	iv
List of Illustrations	viii
List of Tables	xii
Chapter 1 Background	1
Chapter 2 Project Description	3
2.1 Starting The Tunnel With A High Degree Ramp	3
2.2 Boundary-Layer Survey.....	6
2.3 Micro-Vortex Generators	8
2.4 Test Methods And Schedule	10
Chapter 3 The Flow Model Of A MVG	11
3.1 Introduction	11
3.2 Flow Modeling	11
3.3 Flow Analysis.....	14
3.4 Velocity Maps And Discussion	19
Chapter 4 Particle Image Velocimetry Experiments	23
4.1 The Seeding System	23
4.2 Selection Of The Interrogation Area.....	26
4.3 Results For Flow Past A Flat Plate.....	28
4.4 Results For The 20° Ramp.....	35
4.5 Discussion	37
Chapter 5 The Experiment On Surface Flow Visualization.....	38
5.1 Introduction	38
5.2 The Method	38

5.2.1 The Surface Oil Flow Visualization (SFV).....	38
5.2.2 Image Processing	39
5.2.2.1 Define The “Exp Line”	39
5.2.2.2 Define A Few Lines For Comparison	45
5.2.2.3 Define The Index	47
5.3 The Discussion	52
Chapter 6 Transient (Algebraic) Growth Analysis Of MVG Disturbance	54
6.1 Introduction	54
6.2 The Continuous Eigenfunctions In The Free-Stream.....	56
6.3 The Eigenfunctions In The Boundary-Layer.....	61
6.4 Generate The Adjoint System	65
6.5 The Adjoint Linearized Navier-Stokes Equations And Their Solutions	69
6.6 Bi-Orthogonality Fabrication	76
6.7 Results And Discussion.....	82
Chapter 7 Conclusion And Future Work	92
Appendix A The Schlieren Optics Result	94
Appendix B MATLAB Program for Image Processing (PIV part).....	96
Appendix C MATLAB Program for Image Processing (SFV part)	100
Appendix D Boundary Layer Velocity Profile from PIV	103
Appendix E Pro-E drawings	119
Appendix F Matrices and Terms of the LNS Direct and Adjoint Equations	123
References.....	132
Biographical Information	134

List of Illustrations

Figure 1 SFV tests of tunnel started with large angle ramps	5
Figure 2 CAD rendition of the configuration of the 2-D separation area generator	6
Figure 3 The streamwise survey PIV setup	7
Figure 4 CAD rendition of the PIV test.....	8
Figure 5 The MVGs on the flat plate	9
Figure 7 CAD rendition of the oblique shock and the Mach cones offset.....	11
Figure 8 The oblique shock connected smoothly to the two Mach cones	12
Figure 9 Flow model of MVG based on the supersonic base flow theory	13
Figure 10 The four regions of the flow model of MVG	13
Figure 11 The angle of expansion fan (shown in green) was over 90°	15
Figure 12 Supersonic base flow combined with inviscid compressible flow theory.....	16
Figure 13 Flow development on the MVG surface	18
Figure 14 The velocity maps around the MVG	20
Figure 15 The arrangement of the laser sheets.....	22
Figure 16 The situation of free stream seeding in the test section	24
Figure 17 The underneath seeding system	25
Figure 18 The selection of interrogation area	27
Figure 19 The raw data boundary-layer velocity profile on the flat plate	29
Figure 20 Defining the flat plate surface	31
Figure 21 The fluctuating flat plate surface.....	32
Figure 22 The comparison of the locations distribution of fluctuated flat plate surface and the Gaussian distribution.....	33
Figure 23 The plot of all boundary-layer velocity profiles	34
Figure 24 The boundary-layer velocity profile on the 20° ramp.....	36

Figure 25 SFV preparasion	39
Figure 26 The uploaded image in RGB scale	40
Figure 27 The grayscale scaling operation	40
Figure 28 The zoom-in area with intensity gradient	41
Figure 29 The contrast enhanced operation	42
Figure 30 The pixels shown the intensity gradient area reduced	42
Figure 31 The edge sharpened operation.....	43
Figure 32 The pixels showing the distinct shapes and the “exp line”	44
Figure 33 The located “exp line”	45
Figure 34 The five defined lines	46
Figure 35 The zigzag samples with small fluctuates or large fluctuates.....	49
Figure 36 The disturbed boundary layer velocity profile 5 mm down-stream of MVG.....	54
Figure 37 An example of discrete and continuous eigenfunction solution for disturbance equations.....	59
Figure 38 The variation in wavenumber of the continuous eigenfunction	60
Figure 39 The branch plot of α in the complex plan.....	61
Figure 40 $k = 0.5$ for vorticity branch, acoustic branch, and entropy branch	63
Figure 41 The variation in wavenumber along the acoustic branch	64
Figure 42 The influence of Reynolds number on the disturbance in the boundary-layer .	66
Figure 43 The deviation velocity profile u and v from the boundary layer velocity profile 5 mm down-stream of MVG center line	79
Figure 44 The coefficient C of the vorticity, acoustic, entropy, and entropy-acoustic eigenvectors in the complex plane when $k = 0.2$	82
Figure 45 The coefficients C of the vorticity, acoustic, entropy, and entropy-acoustic eigenvectors in the complex plane at $k = 0.3, 1.7, 5.7,$ and 100	84

Figure 46 The MVG perturbation evolution (at $y=0.125$) downstream of the MVG, in the streamwise direction	87
Figure 47 The interaction of vorticity, acoustic, entropy, and entropy-acoustic modes and its outcome in the MVG perturbation	89
Figure 48 The comparison between the simulation and experiment work of MVG downstream perturbation	91

List of Tables

Table 1 The test configuration and method	10
Table 2 The upper and lower bound of flow velocities and Mach numbers.....	17
Table 3 Vertical fluctuations of the test surface	35
Table 4 The index and scaling of the five lines	49
Table 5 The index and scaling of the five lines with the index sensitive to the large fluctuates	51
Table 6 standard deviation is to estimate the effect of MVGs on separation area	52
Table 7 the energy storage in each mode	85

Chapter 1

Background

Attempts at flow separation control arising from adverse pressure gradients including those induced by shocks have proceeded for many decades. One solution for preventing subsonic separation is to use vortex generators (VGs). VGs function by entraining energetic freestream fluid from streamwise vortices into the sluggish, separated boundary-layer flow. However, vortex generators protruding into the freestream induce profile drag that reduces the overall benefit. In the transonic/supersonic regime, there is an additional penalty due to wave drag. To overcome the shortcomings of conventional vortex generators, the idea of “sub-boundary layer vortex generators,” nowadays known as MVGs (MVGs), was proposed first in the early 1970s. The height of a MVG is typically between 10% and 50% of the boundary layer.¹ These submerged protrusions therefore are expected to produce less drag.

Besides the low-profile within the boundary layer, the MVG used in present work has a skewed tetrahedral geometry. This geometry produces a CVP (CVP) at its two swept trailing edges.^{6,11} As the CVP goes downstream, a vortex ring or a hairpin vortex was observed.^{19,20} The mechanism to form a such formation is still controversy, but some suggested the Kelvin–Helmholtz instability may cause the formation happened.^{2,3} In the meantime, MVG keeps producing the CVP, hence eventually there are many of vortex ring or hairpin vortex in line and the train of them will be developed. The train of ring or hairpin vortices penetrate a separated shock / boundary layer interaction, creating a massive three-dimensional distortion that has been thought to be beneficial in practice, e.g., in reducing the size of the separation zone.

The objective of the present work is to examine quantitatively how the shock-induced separation is affected by MVG. We proposed a new developed statistical

method and also applied the eigenvalue problem to the linearized Navier-Stokes equations to evaluate the effectiveness of MVG downstream perturbation on the separation area and how the perturbation evolves. The primary investigation methods, surface flow visualization (SFV) and particle image velocimetry (PIV), will be described in the following chapter. The test configuration in the present work consisted of three MVGs mounted ahead of a 20° ramp on a flat test surface. The experiments were conducted at Mach 2.5. The experimental preparations and the preliminary results will be offered in the next few sections.

Chapter 2

Project Description

2.1 Starting The Tunnel With A High Degree Ramp

The present work was begun with how to start the tunnel with a ramp of high compression, of 16° and above to generate a separation area. After a series of modifications to the test section and the ramp, the tunnel was finally started with a 20° ramp with a nominal two-dimensional separation area. The progress is shown in Figure 1 and the final ramp configuration is shown schematically in Figure 2. In Figure 1, SFV was applied to different ramp configurations to check if the tunnel started or not.

The first problem faced was with unstart tunnel with a 25° ramp. The original thought was not to reduce the ramp angle but to increase the space on the top of the 25° ramp to allow the starting shock to be swallowed past the ramp constriction and into the supersonic diffuser. Based on this surmise, the entire flat plate (including the 25° ramp) was lowered down 50.8 mm by trial and error to increase the clearance to the ceiling to 152.4 mm. However this modification a highly wrinkled separation front as can be seen in Figure 1a. A big bulge and a distinct swirl were found in the middle of the separation area.

It was thought that the strong shock from the 25° ramp may induce significant interference from the tunnel sidewalls, in other words, causing additional, spurious shock/boundary layer interactions. The large subsonic regions from these spurious interactions may feed into the interaction of interest, thereby causing it to be severely distorted. Thus, it was thought that a lower ramp angle 20° may alleviate the distortion. The SFV result with the 20° ramp is shown in Figure 1b. Although the bulge and swirl were eliminated, several small swirls were discovered at the separation area.

The above result indicated that reducing sidewall interference further was necessary. Accordingly, the span of the ramp was reduced from 152.4 mm to 101.6 mm. The SFV result shown in Figure 1c displays a relatively smooth bulge in the middle and with the small swirls seen previously in Figure 1b having vanished. However, the separation area was still not deemed to be adequately two-dimensional. Hence, sharp, swept fences that protruded 17.8 mm ahead of the ramp were installed on both ends as shown in Figure 1d. A two-dimensional separation area was almost there.

In Figure 1e, a longer pair of fences extending 27.9 mm from the ramp was mounted for the same purpose. This was considered to be the final configuration, since a 33 mm flat separation front was measured from the experiment. A CAD schematic of the ramp with the long fences is shown in Figure 2. The two-dimensional separation area displayed in Figure 1e was located at in the between of the fences and the 20° ramp in Figure 2.

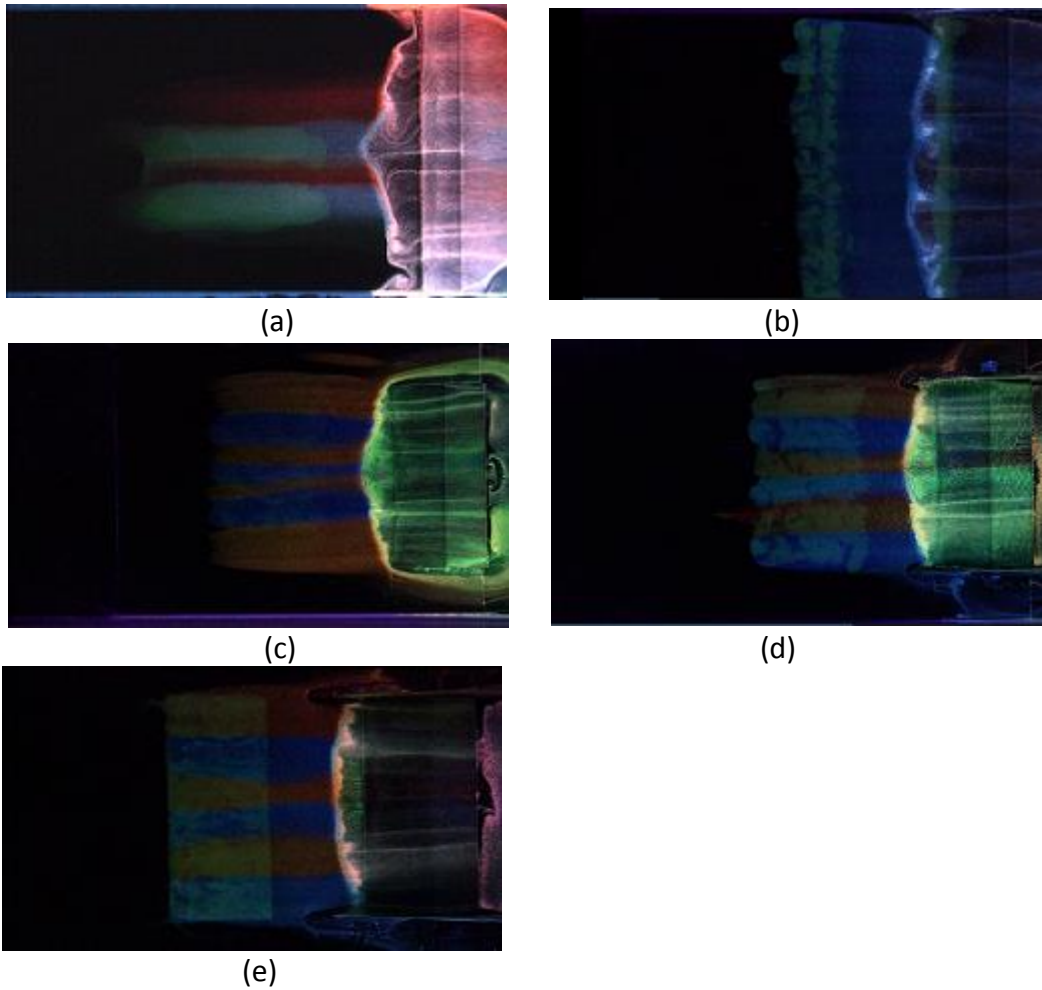


Figure 1 Surface flow visualizations to check that the tunnel started when ramps with large angles were installed and to determine the presence of an acceptable two-dimensional shock/boundary-layer interaction

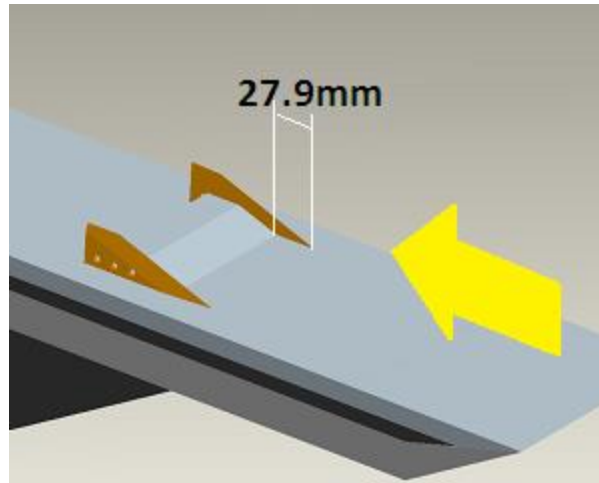


Figure 2 CAD rendition of the configuration of the two-dimensional separation area generator (20° ramp with fences).

2.2 Boundary-Layer Survey

The present work was begun with how to start the tunnel with a ramp of high compression, of 16° and above to generate a separation area. After a series of modifications to the test section and the ramp, the tunnel was finally started with a 20° ramp with a nominal two-dimensional separation area. The progress is shown in Figure 1 and the final ramp configuration is shown schematically in Figure 2. In Figure 1, SFV was applied to different ramp configurations to check if the tunnel started or not.

Particle image velocimetry (PIV) was used to survey the boundary layer. The PIV setup is shown in Figure 3. The setup in the present work was backward backward-scattering. Usually, for streamwise survey, the forward backward-scattering should be satisfied for experiments. However, it was difficult to apply the forward backward-scattering to present experiment because the separation area is lying in between the fences. Thus, the streamwise field of view of separation area was blocked by fences. The initial tries were to adjust the forward backward-scattering to the higher position so the field of view will not be blocked by fences. Nevertheless, the results in the velocity

vector calculation were poor due to the strong laser light reflection from the flat plate surface. With backward backward-scattering, there is no such a problem and also the field of view of separation area can be seen.

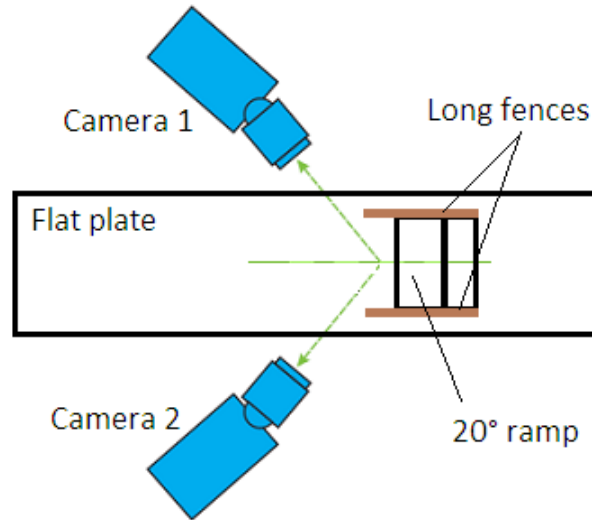


Figure 3 The streamwise survey PIV setup, top view. The two cameras were aimed into the test section (backward backward-scattering), and the laser is on the top of the test section. The green line in the middle is the laser light sheet.

The survey was carried out along the centerline of the flat plate in streamwise direction. Also, surveys are planned for three spanwise stations, at the incoming flow, at the MVG position (50 mm upstream the ramp corner), and at the separation area (within 20 mm from the ramp corner). Example schematics of the survey stations are shown in Figure 4.

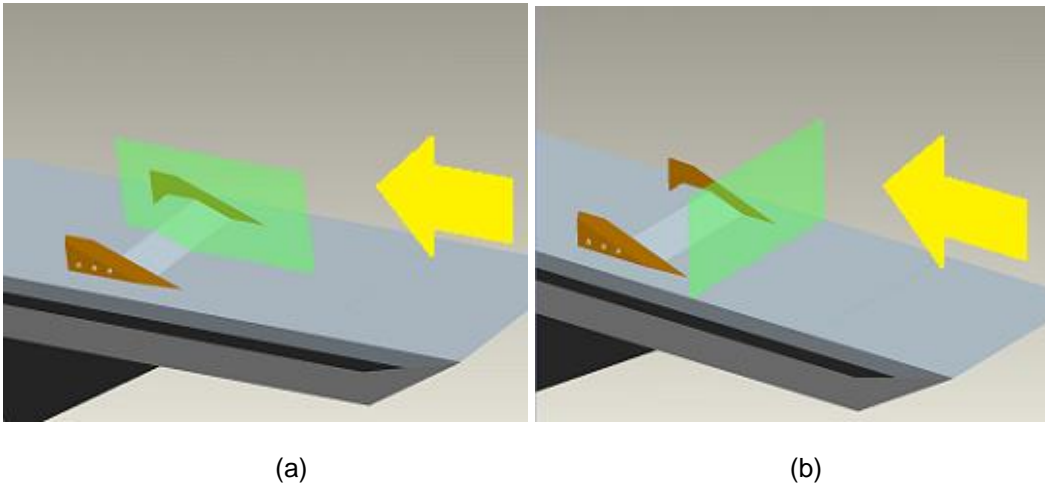


Fig. 4. CAD rendition of the PIV test: (a) streamwise and (b) spanwise station on the flat plate. The green is the laser sheet.

2.3 Micro-Vortex Generators

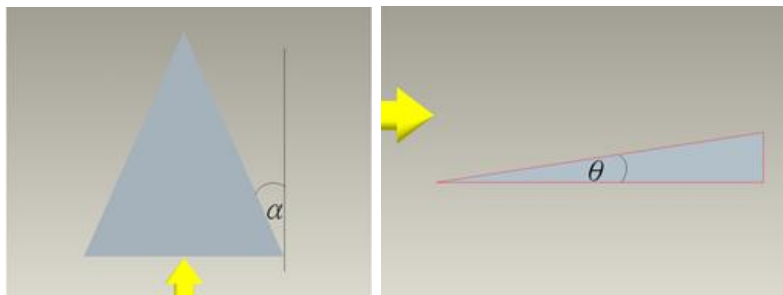
MVG, one of the potential flow control methods, has many kind of profiles.² The present work used was ramp type MVG. It was designed symmetrically in streamwise in a skewed tetrahedral profile, and has a leading declined angle and two swept-forward trailing edges. Form the top view, the MVG was presented in an isosceles triangle with $\alpha = 24^\circ$. From the side view, the MVG has a leading edge angle $\theta = 8.6^\circ$ with a vertical elevation angle at its back. Schematics are shown in Figure 5. The height of the MVG in the present experiment is 2 mm, representing about 40% of the height of the incoming boundary layer ($\delta \approx 5$ mm).⁴ The MVG has a chord of 12.95 mm long, and a leading edge that is 11.7 mm wide.^{5,6} The MVGs were made of epoxy using 3D printing at the University of Texas at Arlington Research Institute. Instead of five of MVGs on an insert bar like the previous research, the MVGs in the present experiment were made individually and were manually attached on the flat plate by silicone adhesive. The arrangement of MVGs on the flat plate is shown in Figure 5. Three MVGs in an array

were placed at 230 mm downstream of the flat plate leading edge and 50 mm upstream of the ramp corner. The center-to-center spacing between the MVGs was 20.5 mm.



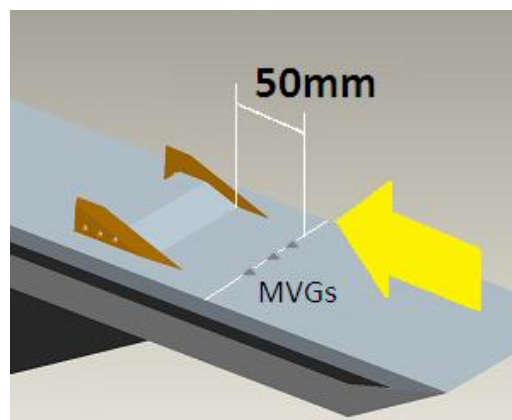
(a)

(b)



(c)

(d)



(e)

Figure 5 The MVGs on the flat plate: (a) side view, and (b) top view. CAD rendition of a single MVG: (c) top view, and (d) side view. (e) The layout of MVGs combined with ramp.

2.4 Test Methods And Schedule

Both SFV and PIV were arranged for the tests on 20° ramp and MVG combined with 20° ramp. Table 1 shows the test methods and schedule.

Table 1 The test configuration and method

	Surface flow visualization	Particle image velocimetry
Flat plate	Refer to previous study ⁴	Refer to previous study ⁴
MVG	Refer to previous study ⁴	Refer to previous study ⁴
20° Ramp	Completed	Completed
MVG combined with 20° ramp	Completed	Completed one station at 5 mm downstream of the MVG

Chapter 3

The Flow Model Of A MVG

3.1 Introduction

The purpose of this analysis was to develop a model of the supersonic flow past an MVG. The inviscid property and the theory of supersonic base flow will be used in the calculation. This section 3 was divided into three parts. The first part was modeling of flow field around the MVG. The section part was about the calculations based on the model. In the end, a velocity distribution map by this model was provided.

3.2 Flow Modeling

The incoming flow is at Mach 2.5. This flow produces two Mach cones and an oblique shock at the leading edge. The Mach angle is $\beta_c = 23.58^\circ$ that is smaller than the 24° sweep of the sides. The oblique shock angle is $\beta_s = 30.55^\circ$, based on the two-dimensional oblique shock wave theory. The discrepancy between these two angles can be seen in Figure 7. Thus, for continuity in three-dimension, the oblique shock has to weaken around the leading edge to merge to the Mach cone (Figure 8). The three-dimensionality of the flow introduces velocity gradients.

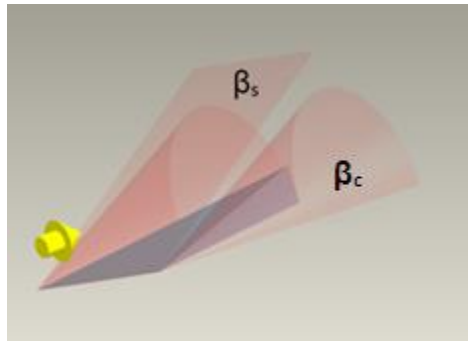


Figure 7 CAD rendition of the oblique shock and the Mach cones offset.

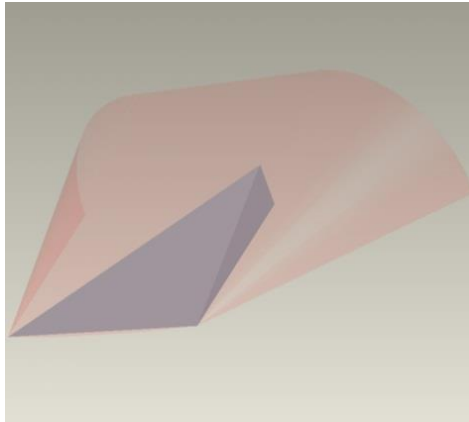


Figure 8 The oblique shock connected smoothly to the two Mach cones.

The theory of supersonic base flow was then proposed to approach the problem. Supersonic base flow is a typical subject which involved the interaction of an external hyperbolic region with a region where viscous effects are important.⁷ The theory results in an expansion fan at the base edge (the vertical elevation at the back of MVG), a reattachment shock wave around the reattachment point, and a recirculation region behind the base. Note that the two MVG trailing edges are actually two base planes to yield individual reattachment lines (where the reattachment shock originated). In this representation, the oblique shock at leading edge together with the Mach cones at two apices will be able to connect to each other to the reattachment lines to form a smooth envelope, shown in Figure 9.

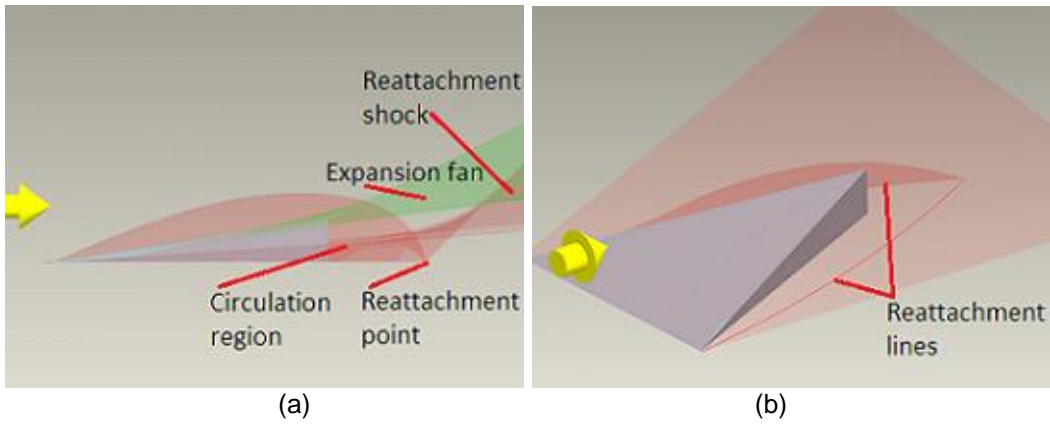


Figure 9 Flow model of MVG based on the supersonic base flow theory: (a) side view, and (b) top view (the expansion fan not shown).

Finally, the flow model was determined. For clear and convenient purposes, the near MVG space was divided into four regions, shown in Figure 10. The four regions are (1) the free stream flow before the oblique shock, (2) the flow over the MVG, (3) the flow after the expansion fan, and (4) the flow after the reattachment shock. For simplicity, the circulation region (3) was considered without circulation.

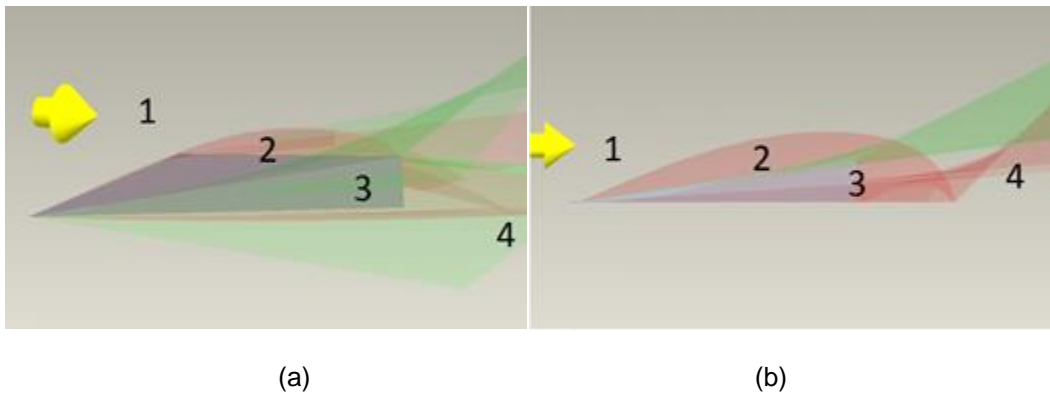


Figure 10 The four regions of the flow model of MVG: (a) downstream top view, and (b) side view.

3.3 Flow Analysis

A perfect gas is assumed. Also assume that the total temperature is 300 K in the plenum chamber. First, the free stream velocity v_1 can be determined by the speed of sound and the definition of Mach number. Thus, $v_1 = 569 \text{ m/s}$.

Secondly, in region 2, the Mach number M_2 and the velocity v_2 behind the oblique shock were calculated. Based on section 3.2, given $\theta = 8.6^\circ$, $M_1 = 2.5$, by Eqs. (1), (2), (3), (4), and the quantitative formulations of conical flow, the range of M_2 can be estimated as bounded between 2.14 and 2.32 and β_s is between 30.55° and 24.65° . Note that $M_2 = 2.14$ and $\beta_s = 30.55^\circ$ are the values for an infinite two-dimensional ramp, and $M_2 = 2.32$ and $\beta_s = 24.65^\circ$ are the values for the semi cone. In the present work, the former will be known as the lower bound case and the latter as the upper bound case. Substituting lower and upper bounds into the temperature ratio across the oblique shock (5) to calculate T_2 . By T_2 , speed of sound after the shock can be determined. With speed of sound and known M_2 , the velocity V_2 was solved, thus, $V_2 = 530.5 \text{ m/s}$ for the lower bound, and $V_2 = 552.4 \text{ m/s}$ for the upper bound. As a result, we have, after oblique shock, V_2 ranging from 530.5 to 552.4 m/s.

$$\tan \theta = 2 \cot \left[\frac{M_i^2 \sin^2 \beta_s - 1}{M_i^2 (\gamma + \cos 2\beta_s) + 2} \right] \quad (1)$$

$$M_{n,i} = M_i \sin \beta_s \quad (2)$$

$$M_{n,i+1}^2 = \frac{M_{n,i}^2 + \left[\frac{2}{\gamma - 1} \right]}{\left[\frac{2\gamma}{\gamma - 1} \right] M_{n,i}^2 - 1} \quad (3)$$

$$M_{i+1} = \frac{M_{n,i+1}}{\sin(\beta_s - \theta)} \quad (4)$$

$$\frac{T_{i+1}}{T_i} = \left[1 + \frac{2\gamma}{\gamma + 1} (M_{n,i}^2 - 1) \right] \left[\frac{(\gamma - 1)M_{n,i}^2 + 2}{(\gamma + 1)M_{n,i}^2} \right] \quad (5)$$

Next, the flow properties at the two side edges and at the tail corner should be determined. This part of the MVG causes flow turning at an angle over 81.35° . The Mach number after the expansion fan can be computed by the Prandtl-Meyer expansion Eqs. (6), (7), (8).

$$\mu_i = \sin^{-1} \frac{1}{M_i} \quad (6)$$

$$v(M_i) = \sqrt{\frac{\gamma+1}{\gamma-1}} \tan^{-1} \sqrt{\frac{\gamma-1}{\gamma+1} (M_i^2 - 1)} - \tan^{-1} \sqrt{M_i^2 - 1} \quad (7)$$

$$\theta_{i+1} = v(M_{n,i+1}) - v(M_i) \quad (8)$$

The Mach number M_3 was found over 10. This Mach number was too large to be reasonable. Also, the expansion fan spread out over 90° was believed to be too wide (Figure 11).

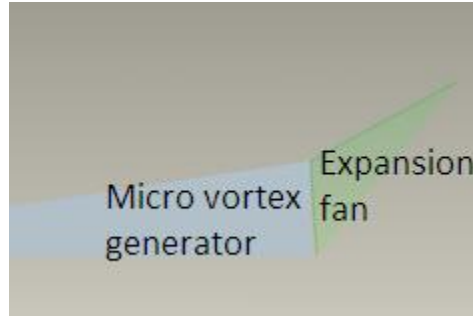


Figure 11 The angle of expansion fan (shown in green) was over 90° .

As claimed at the end of section 3.2, the theory of supersonic base flow was considered to be applied at this stage. According to the theory, the expansion fan will not spread out that extreme, and the reattachment shock will appear to be an oblique shock (Figure 12). The author's challenge was to find the reattachment point, and this theory seems to give a reasonable solution. Once the reattachment point is determined, the angles of expansion fan and the reattachment shock can be found. To find the reattachment point, a report ratio 2.5 of the distance D to the base height at Mach 2.46

was adopted.¹⁰ D is the distance from the base to the reattachment point, shown in Figure 12. The statement hinted that the tangent of ϕ should be 0.4, thus $\phi = \tan^{-1} 0.4 = 21.8^\circ$, see Figure 12. Therefore, the flow at the tail corner should firstly turn through $\theta = 8.6^\circ$, and then immediately turn downward 21.8° to the floor. It should be noted that the reattachment point changes its position with Mach and Reynolds numbers. For example, Mach number M_2 , 2.14 and 2.32 are possibly to have different ratio of the reattachment distance D to the base height. Nevertheless, the reattachment point is a statistical position of the reattachment shock (shock wave is always slashing around at a certain frequency). Therefore, in this present analysis the ratio was assumed to stay the same for both Mach number 2.14 and 2.32. Now by (6), (7), (8), the Mach number and the velocity after the expansion fan can be found at $M_3 = 3.63$ and $V_3 = 653.15 \text{ m/s}$ for lower bound, and $M_3 = 3.95$ and $V_3 = 668.1 \text{ m/s}$ for upper bound. Besides, the expansion fan was calculated spreading out at 42.2° for lower bound, and 41.2° for upper bound, shown in green area in Figure 12.

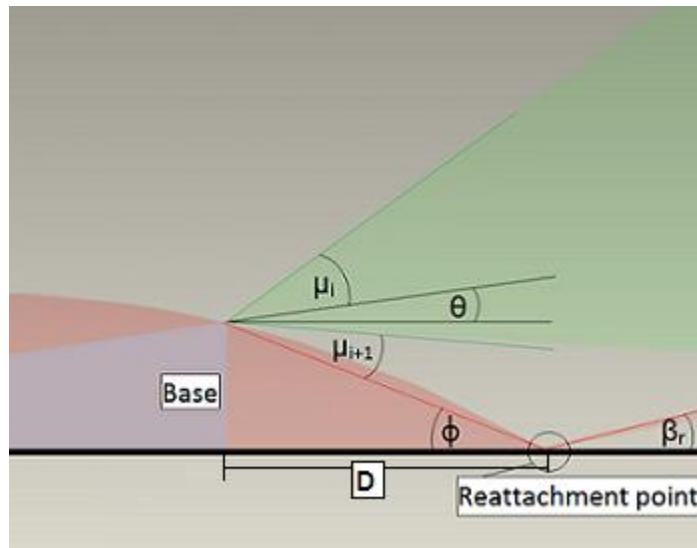


Figure 12 The supersonic base flow theory combined with inviscid compressible flow theory calculation.

The above calculation is for the tail corner. For the calculation of two trailing edges, the flow developed on the MVG top surface is similar to the pattern of oil surface visualization in the experiments,¹¹ and then expand at two trailing edges (Figure 13). The velocity calculations along surface pathway directions were only selected a few at 6°, 26°, 46°, and 66° away from the center line. The magnitude of velocities at 6°, 26°, 46°, and 66°, $V_{2,j}$, were descended due to the swept trailing edges.

$$V_{2,j} = \frac{V_2 \sin(\alpha)}{\sin(\alpha + j)}, \text{ where flow direction } j = 6^\circ, 26^\circ, 46^\circ, 66^\circ.$$

$j = 0$ for tail corner.

An important phenomenon was found immediately after applying the idea of pattern of oil surface visualization that there is a sonic boundary (a boundary of subsonic and supersonic flow) lying in between 26°-46° at the trailing edge. By the same steps and calculations done for tail corner, inputting θ_j and $M_{2,j}$, the Mach number $M_{3,j}$ and the velocity $V_{3,j}$ after the expansion fan can be found, shown in Table 2.

Table 2 The (a) upper and (b) lower bound of flow velocities and Mach numbers (the N/As were not calculated because of the $M_{2,j}$ already at subsonic conditions).

(a)

Flow directions j (°)	tail corner	6	26	46	66
$V_{2,j}$ (m/s)	530.5	431.5	281.7	229.6	215.8
$M_{2,j}$	2.14	1.74	1.14	0.93	0.87
θ_j (°)	8.6	8.59	7.78	6.03	3.54
$M_{3,j}$	3.63	2.98	2.2	N/A	N/A
$V_{3,j}$ (m/s)	653.15	613.49	538.01	N/A	N/A
Expansion fan(°)	42.2	45.9	64.2	N/A	N/A
βr_j (°)	14.27	18.31	29.12	N/A	N/A
$M_{4,j}$	2.26	1.88	1.31	N/A	N/A

$V_{4,j}$ (m/s)	493.03	488.03	350.94	N/A	N/A
-----------------	--------	--------	--------	-----	-----

Table 2 Continued (b)

Flow directions j (°)	tail corner	6	26	46	66
$V_{2,j}$ (m/s)	530.5	431.5	281.7	229.6	215.8
$M_{2,j}$	2.14	1.74	1.14	0.93	0.87
θ_j (°)	8.6	8.59	7.78	6.03	3.54
$M_{3,j}$	3.63	2.98	2.2	N/A	N/A
$V_{3,j}$ (m/s)	653.15	613.49	538.01	N/A	N/A
Expansion fan(°)	42.2	45.9	64.2	N/A	N/A
βr_j (°)	14.27	18.31	29.12	N/A	N/A
$M_{4,j}$	2.26	1.88	1.31	N/A	N/A
$V_{4,j}$ (m/s)	493.03	488.03	350.94	N/A	N/A

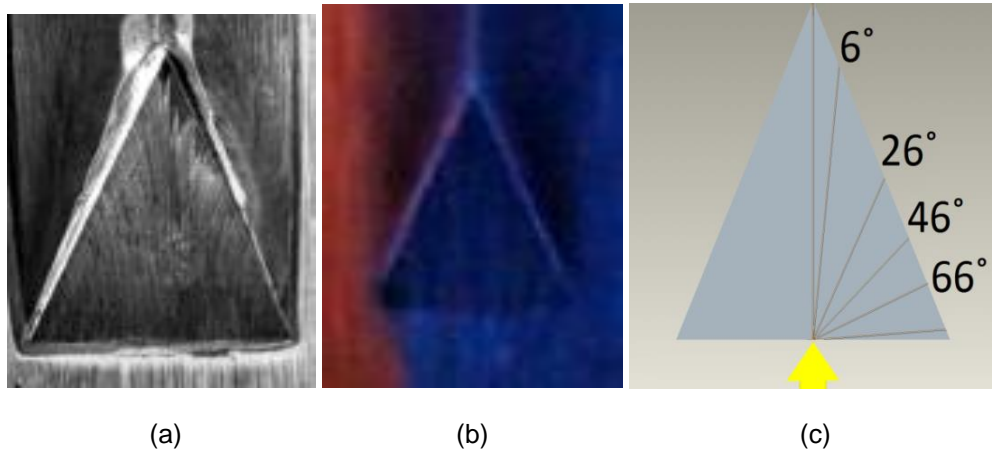


Figure 13. Flow development on the MVG surface: (a) the oil surface flow experiments,¹¹ (b) the experiment result of the present work, and (c) the selected pathways of flow development.

After flow passed through the expansion fan, it continued to propagate downstream to the reattachment point and then flow was deflected an angle of 21.8° by floor, result in forming a reattachment shock (Figure 12.). The flow V_3 was slowed down to V_4 behind the reattachment shock. Again using the oblique shock relations Eqs. (1),

(2), (3), (4), inputting $\phi = 21.8^\circ$ and M_3 , the Mach number M_4 , velocities V_4 after the reattachment shock, and the shock angle β_r can be calculated, results also shown in Table 2. It is noted that below $M_4 = 1.88$, the reattachment shock was detached. Therefore, the calculation was assumed of normal shocks in those areas.

By Table 2 and the velocity calculations completed in present section, finally the velocity maps can be plotted. The maps are shown and discussed in the following section.

3.4 Velocity Maps And Discussion

Figure 14 displays the velocity maps according to the present flow model. Special attention was paid to the yellow circle in this figure. Although a full velocity distribution around this circle could not be obtained, it is reasonable to picture that a round shear layer area is formed due to the momentum difference around the circle. This circle continued propagating downstream while it interacts with the surrounding flow may cause instability.

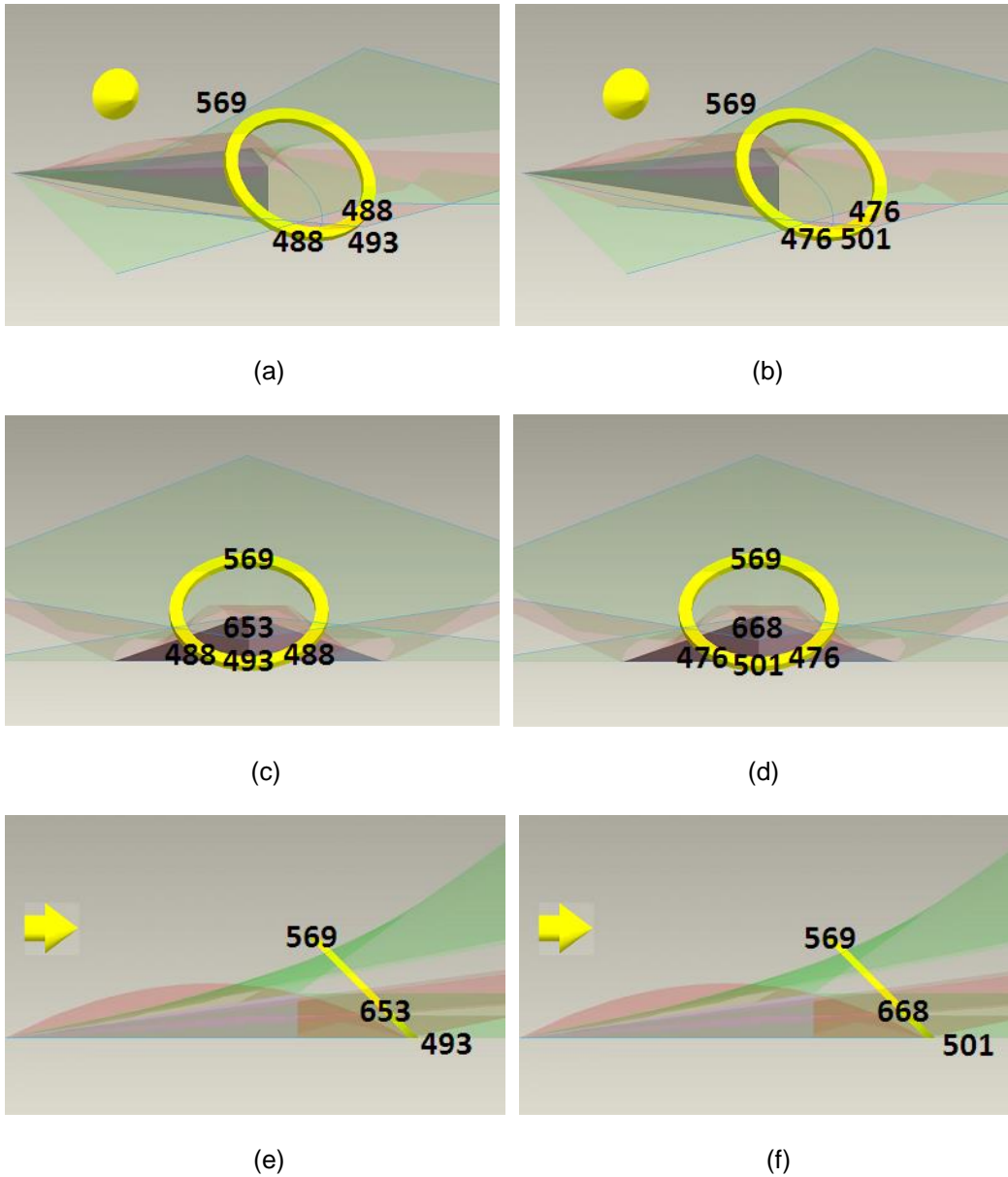
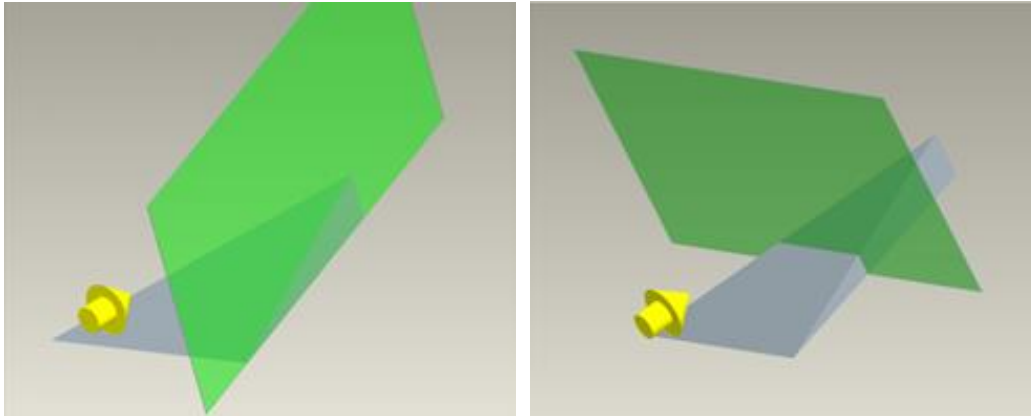


Figure 14 The velocity maps around the MVG. Unit in m/s. (a), (c), and (e) are lower bound. (b), (d), and (f) are upper bound. (c) and (d) are the MVG back view at downstream of the MVG, and the flow direction is point out the paper.

With flow properties in Table 2 and the velocity maps in Figure 14, the flow model proposed in the present section has five outputs to correlate with experiments. Firstly,

the free stream velocity. The free stream velocity V_1 was calculated by presuming the total temperature of 300 K, so any measured V_1 in the experiment can vary and should be based on the temperature in the measurement environment. The second point is the oblique shock angle β_s and the velocity V_2 after the shock. Starting from this point the calculated velocity was suggested to have upper and lower bound, and the velocity measurements were expected to be in this range. Thirdly, the angle of the expansion fan and the velocity V_3 after the expansion were of interest to be compared with the measurement one. Fourthly, the results of experiments should be compared with the assumed reattachment line, the reattachment shock angle β_r , and the velocity V_4 after the reattachment shock. The last point, also the most important point, belongs to the spanwise velocity measurement just downstream of the MVG. As shown in Figure 14, the velocity measurements will focus on the yellow round region.

Nevertheless, some technical issues arise when collecting such velocities data. For example, the survey of sonic boundary lain in between 26° - 46° at the trailing edge (referred to Figure 13). It will be better if the laser sheet can be aligned with one of the MVG trailing edges (Figure 15a). However, the laser, the cameras and the test section arrangement would be very difficult to do so. Hence, instead of aligning with the trailing edge, the laser sheet can be located at several spanwise positions on the MVG to search the sonic boundary (Figure 15b). Besides, the recirculation region near the base, the reattachment lines, and the position of the detached reattachment shock could be discovered by monitoring the velocity gradient along the spanwise surveys too.



(a)

(b)

Figure 15 The arrangement of the laser sheets: (a) along with the MVG trailing edge, and (b) along with the spanwise position.

Chapter 4

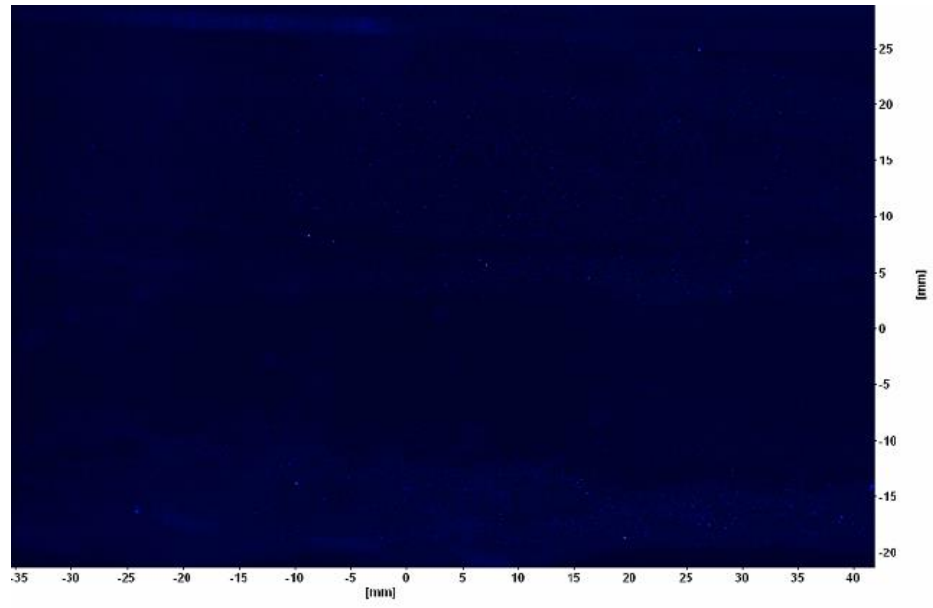
Particle Image Velocimetry Experiments

The PIV employed in the present work uses a New Wave Research Solo Model 120 double-pulsed Nd:YAG laser, two LaVision Image Intensive 3S cameras, and LaVision DaVis 7.1 software. Titanium dioxide particles nominal diameter 20nm was used as flow tracing particles. Usually, the most challenge tasks for PIV measurements are ensuring uniform seeding and selection of the interrogation area for velocity vector calculations. These two issues significantly affect the results of the measurements. In the following section 4.1 and 4.2, some details of our setup will be presented. The objective of PIV experiments was to obtain the boundary-layer velocity profiles. The experiments were arranged on the flow of flat plate, the incoming flow past the 20° ramp, and the flow past the combination of MVGs and the 20° ramp.

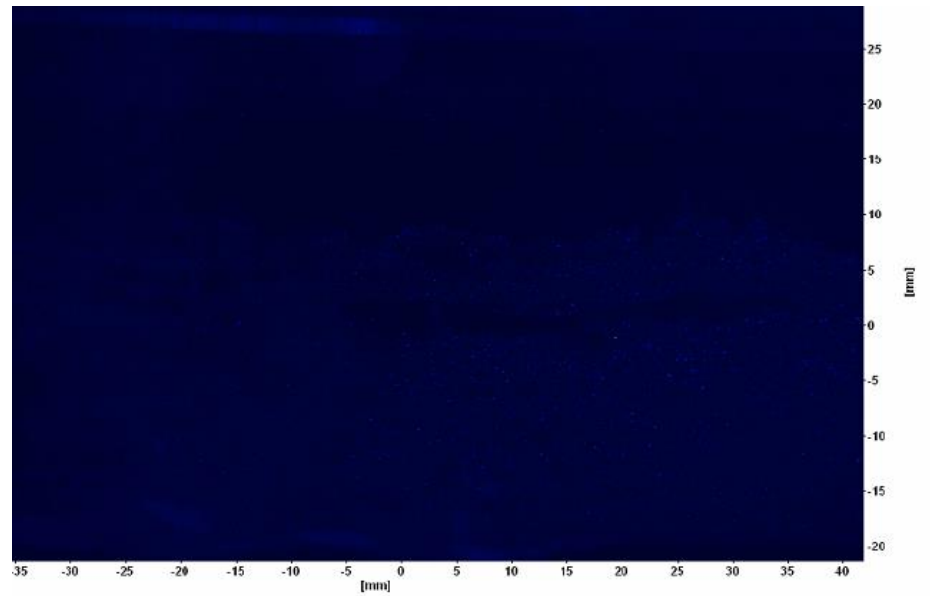
4.1 The Seeding System

The seeding operation was originally carried out from the plenum chamber, and the titanium dioxide particles were assumed to trace the flow faithfully.⁴ The titanium dioxide was delivered at 1200 kPa from a small pressurized cyclone to the plenum chamber during the test. The delivery pressure exceeded the stagnation pressure of 550 kPa.

Figure 16 shows the seeding situation in the test section. The seeding was observed to be non-uniform and also the seeds were not sufficient near the flat plate surface (at the bottom of the images). Thus, a new seeding method was designed and implemented.



(a)



(b)

Figure 16 The situation of free stream seeding in the test section. Image (b) is delayed by 0.2 s from image (a) then one at a time.

The new seeding system was arranged underneath the flat plate. A 5 mm diameter hole on the flat plate surface was made and connected to a tube underneath it. This tube was then connected to a hose outside of test section to the seeder, see Figure 17. During the tests, the titanium dioxide was introduced from the outside at ambient atmosphere pressure to the test section which was at lower pressure (around 53 kPa) to the flat plate surface by natural suction. The results can be seen in Figure 17d.



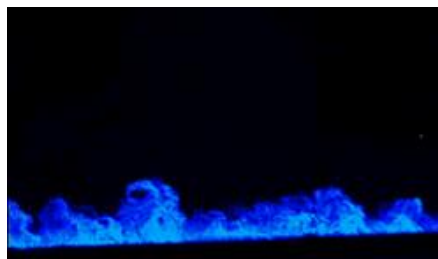
(a)



(b)



(c)



(d)

Figure 17 The underneath seeding system: (a) the pipe arrangement on the flip side of the flat plate, (b) the seeder (the blue box at the ground) setup at outside of the test section, (c) the 5 mm hole introducing titanium dioxide into the test section, and (d) the seeding situation during the test (instantaneous image, flow from right to left).

The PIV requires dense and uniform seeding in the flow, especially near flat plate surface. A result in Figure 16 was not acceptable because the PIV was not calculating any velocity vector due to the poor seeding. Figure 17d was considered a good result since it allowed the software to yield adequate velocity vectors.

4.2 Selection Of The Interrogation Area

The interrogation area is not an investigation window of interest, but an investigation window for the computer to calculate and determine the size and the direction of velocity vectors. Details can be found in the PIV user manual. Here, an example is offered for reference to understand a good and a bad result.

Some basic information is needed for the calculation (consider only the x direction): the pixel count of the CCD (1376 by 1040), the field of view (set in the present experiments to 65 by 45 mm), and the free stream velocity (569 m/s). The goal is to generate velocity vectors in the PIV which requires the generation of a single velocity vector in each interrogation area. The way an interrogation area can generate a velocity vector is by detecting the initial spot and the final spot of the group of titanium dioxide particles in a given amount of time (in fact, this is the time interval of the double pulse laser). For example, if a titanium dioxide particle was detected initially at the bottom of the interrogation area and subsequently detected at the top an upward velocity vector will be generated. If the time interval is, say, 0.9 μ s, the particle has traveled Δx

$$\Delta x = 569000 \text{ mm/s} \times (0.9 \times 10^{-6} \text{ s}) = 0.513 \text{ mm}$$

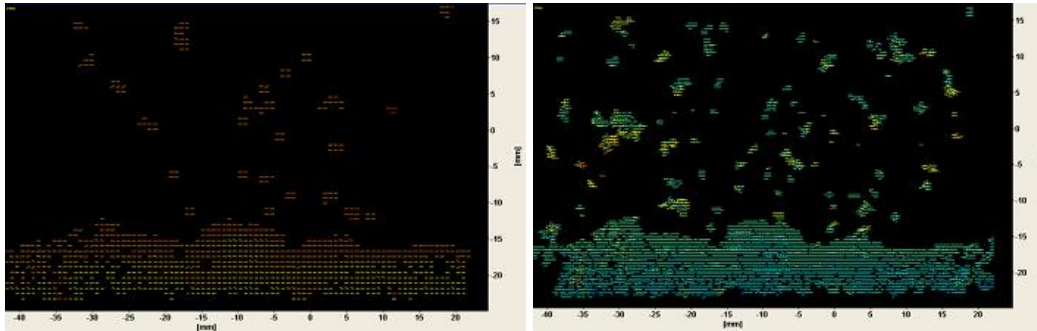
Actually, a pixel length is 0.0472 mm (65 mm / 1376 pixel = 0.0472 mm/pixel).

Therefore, a 32 x 32 pixel interrogation area has sides that are

$$0.0472 \text{ mm/pixel} \times 32 \text{ pixel} = 1.512 \text{ mm}$$

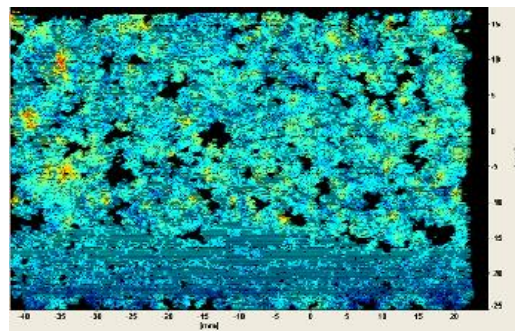
Likewise, a 16 x 16 pixel and an 8 x 8 interrogation area have sides of 0.756 mm and 0.378 mm respectively. Obviously, only the 32 x 32 pixel and the 16 x 16 pixel cases

provide sufficient resolution in exceeding Δx . The 8 x 8 pixel example is bad because the particle has already left the interrogation area. The following Figure 18 displays the situation of interrogation areas in the field of view. In Figure 18c, the velocity vectors are chaos and nothing can be seen or be calculated.



(a)

(b)



(c)

Figure 18 The selection of interrogation area: (a) the 32 x 32 case (b) the 16 x 16 case, and (c) the 8 x 8 case. In each case, lots of velocity vectors can be seen. Every vector displays here indicated one individual interrogation area. The smaller the numbers (such as 32 x 32, 16 x 16, and then 8 x 8), the more the interrogation area and vectors have in the field of view. However, 8 x 8 was not a good selection in the situation since it displays not too much but chaos.

4.3 Results For Flow Past A Flat Plate

After setting the interrogation area (in the case 32 by 32 case or 16 by 16, either one is ok) and calculations performed by DaVis 7.1, the velocity vectors were generated and field of views like in Figure 18 can be determined. The velocity profiles were then obtained from those field of views. The results of the flat plate at $x=0$ (203 mm downstream of the flat plate leading edge) are shown in Figure 19, where (a), (b), and (c) displayed the instantaneous profiles. The boundary-layer velocity profiles in Figure 19 showed large amounts of drop out due to bad vectors. After applying time and spacetime averaging of 75 images, general form of the boundary layer appears to be captured as shown in Figure 19(d) and (e).

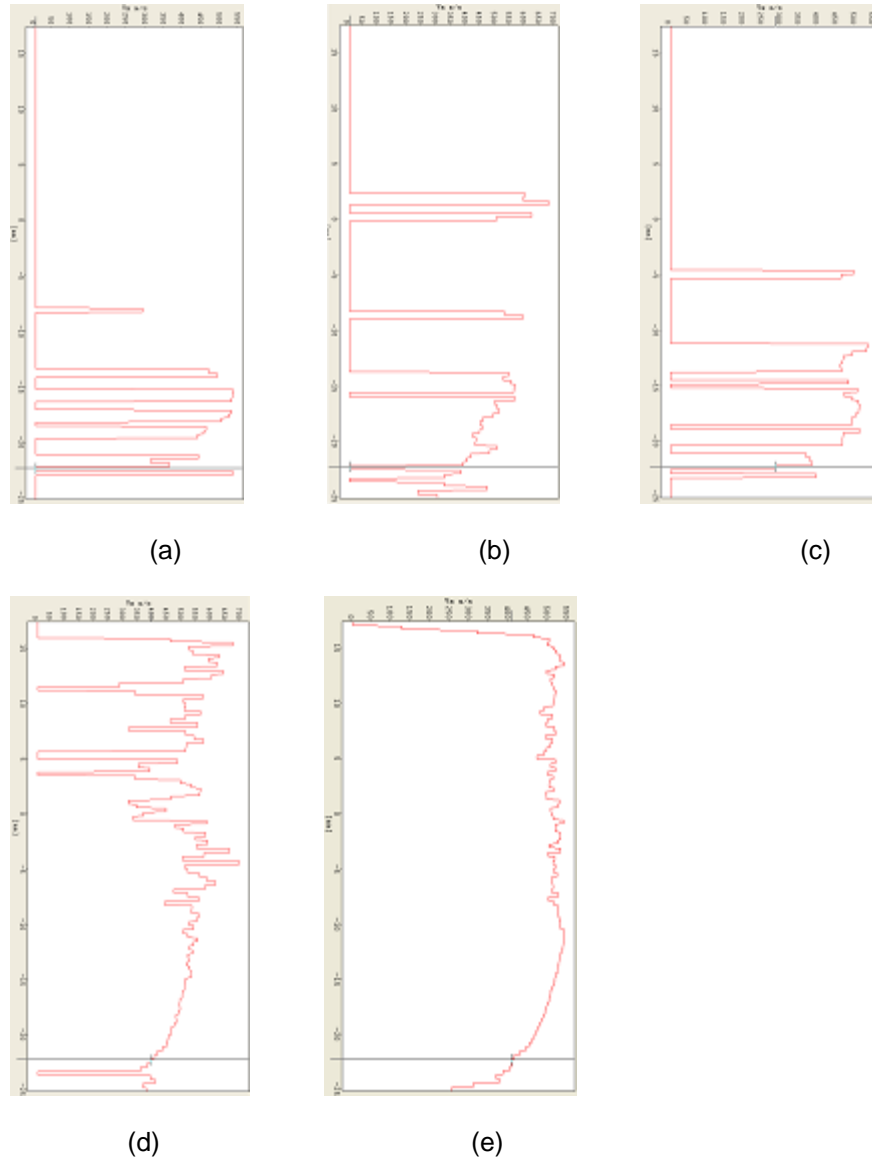
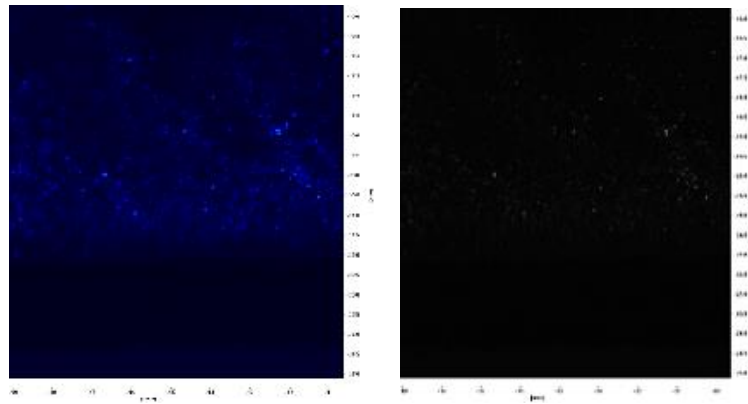


Figure 19 The raw data boundary-layer velocity profile on the flat plate: (a) a randomly chosen instantaneous image. (b) Another instantaneous image after 0.2 seconds. (c) Another instantaneous image after 0.4 seconds. (d) The image after time averaging of 75 images. Each of the images was 0.2 seconds apart. (e) The image after time averaging of 75 images and space averaging of neighborhood area of flow field. The flow direction in all images is from left to right. Same larger images can be referred in appendix D I.

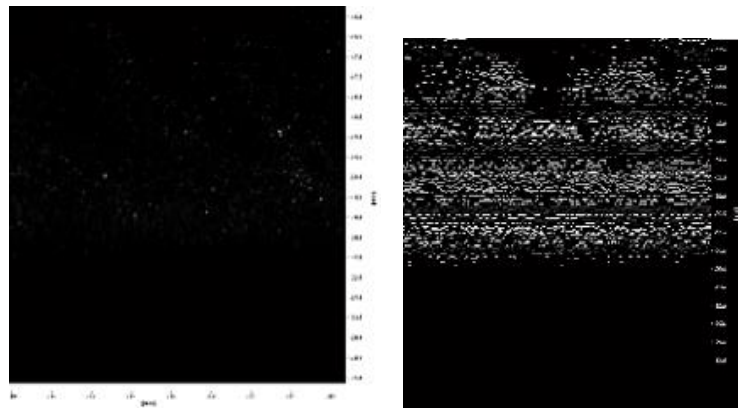
The bottom line in Figure 19 was found roughly to be the position of the flat plate surface. A further investigation to locate the flat plate surface and the boundary layer height is yet to be completed.

The method to define the flat plate surface was by image processing in MATLAB. The 800 time zoom-in view of PIV Image, like shown in Figure 20(a) in BMP format, was processed by MATLAB to identify the flat plate surface.



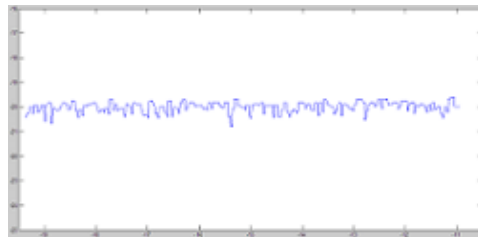
(a)

(b)



(c)

(d)



(e)

Figure 20 Defining the flat plate surface: (a) the original image after 800 time zoom-in, (b) the image after gray scaling operation, (c) the image after contrast enhancement operation, (d) applying the Sobel operation, and (e) the surface was found and defined.

To find the flat plate surface (the program can be found in the appendix B I), the strategy was first to turn the image into gray scale. Then contrast enhancement and Sobel operation were applied to define the surface boundary. After these three processes, the image showed the lower portion to be all black and the top portion area with lots of white spots as in Figure 20(d). The white spots indicate the location of dispersed titanium dioxide particles in the flow field or the bright surface, and the blackened lower area should be the flat plate. Based on this idea, the flat plate surface could be defined and found by searching the first non-zero number (the first white spot) from the bottom to the top in every column of Figure 20(d). By applying the MATLAB command **find** and plotting every first non-zero pixel in each column, the flat plate surface was presented in Figure 20(e).

The same strategy was applied to other 56 images (totally 57 images in the same experiment run). Consequently, the surface was found to be at 57 locations (some locations may repeat), shown in Figure 21. It was discovered that the surface were vertically fluctuating in the video recording, and now a quantitative way was offered here. Moreover, a few data (surfaces) were also seen at the upper side of Figure 21. Those data are not considered at this moment and will be removed.

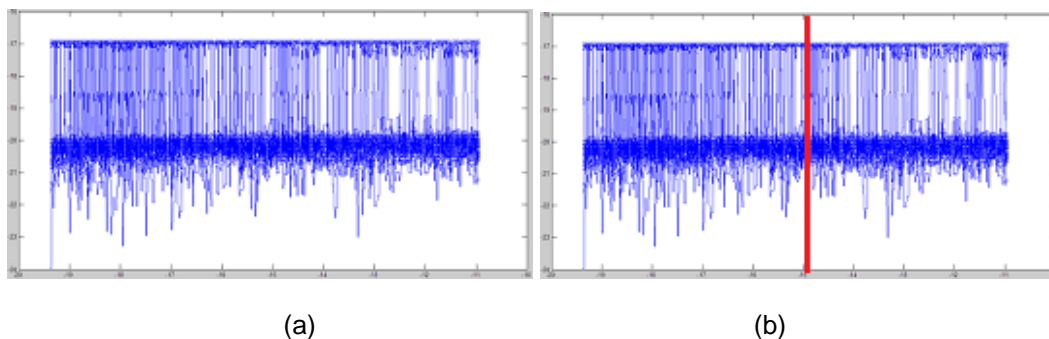


Figure 21. The fluctuating flat plate surface.

If the any specific location on the surface (x axis) is of interest, the spot can be evaluated individually in advance. An example is shown in Figure 21(b), a location at leading edge downstream of 203 mm ($x=-15.1429$ in the field of view in PIV cameras) on the flat plate was chosen for analysis. The distribution of vertical surface movement at $x=-15.1429$ was compared to the Gaussian distribution, and the result was shown in Figure 22. In Figure 22, the x axis represents the location of the flat plate surface, and the y axis represents the frequency. Obviously, the mode is not at the mean location.

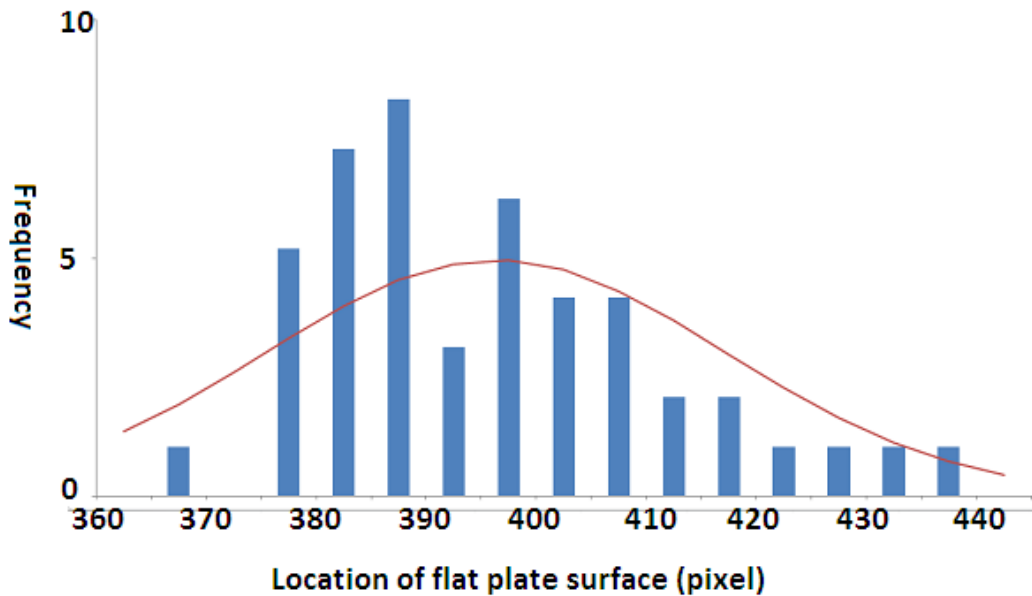


Figure 22. The comparison of the locations distribution of fluctuated flat plate surface (the blue bars) and the Gaussian distribution (the red curve). The smaller the pixel, the higher the location of flat plate surface is.

Next, attempts were made to obtain the boundary-layer velocity profiles. At this moment, the focus is on the flat plate surface, the boundary layer height will not be considered. Since the flat plate surface was found to fluctuate, the boundary-layer velocity profiles plotted were not real profiles unless all the profiles have the same reference position. In order to achieve this, a stitching process was applied to 57 images

in a single run. The stitching processing and the related programming can be referred to in Figure 23 (note the changing of y scale in Figure 23 c and d) and appendix B II. In the process, all the boundary-layer velocity profiles were stitched to the mean position.

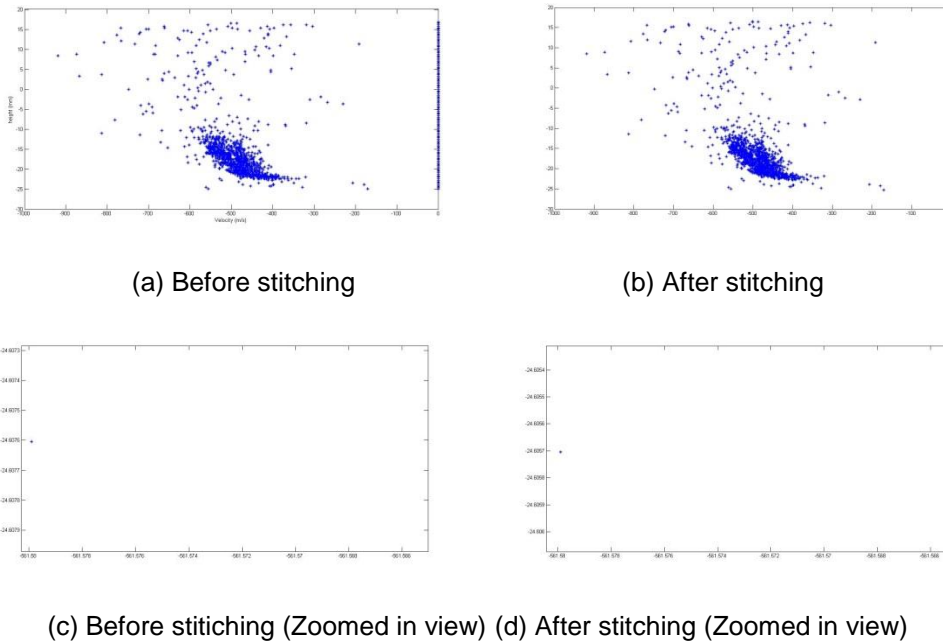


Figure 23 The plot of all boundary-layer velocity profiles from image #20-#76. Note that in (a) and (b), the two images almost identical was because the fluctuation was too small (0.0019 mm) to be seen after stitching. (c) and (d) were the zoom-in case from the same boundary-layer profile for reader's convenience to see the difference. In (c), the blue star was closed to $y=-24.6076$, and in (d), the same blue star was actually stitched down to be closed to $y=-24.6057$. Therefore, this selected boundary-layer velocity profile has 0.0019 mm difference higher to the reference (mean) boundary-layer velocity profile. The flow direction is from right to left in all (a), (b), (c), and (d).

Basically, the strategy was first to take the boundary-layer velocity profiles out from the text files of DaVis software at $x=-15.1429$ and using the mean value as the reference to stitch all other flat plate surface locations in the other 56 images. The results

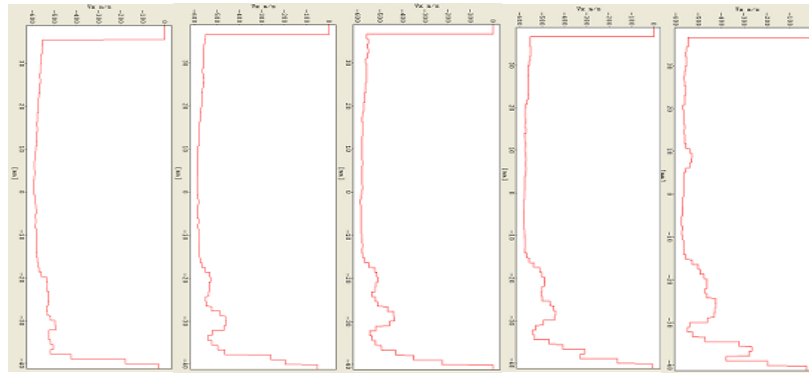
are plotted in Figure 23b, which shows all profiles with the surfaces adjusted to the same level. This stitching operation revealed that the boundary layer velocity profile can have an error of up to 10% if the flat plate's vertical movement is ignored (fluctuation may up to 0.5 mm and boundary layer is about 5 mm, Table 3).

Table 3 Vertical fluctuations of the test surface

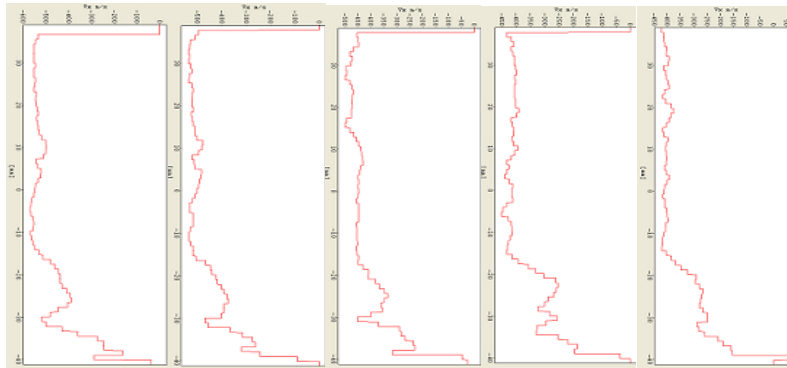
Difference from mean value (mm)	Counts	% of 5 mm BL
-0.1345	8	2.69
-0.1799	6	3.598
-0.2254	5	4.508
0	3	0
0.0473	3	0.946
-0.0436	2	0.872
0.0928	2	1.856
0.0019	2	0.038
0.3201	1	6.402
0.5473	1	10.946
-0.0436	1	0.872
0.2292	1	4.584
-0.089	1	1.78
0.2746	1	5.492
0.1837	1	3.674
-0.08	1	1.6

4.4 Results For The 20° Ramp

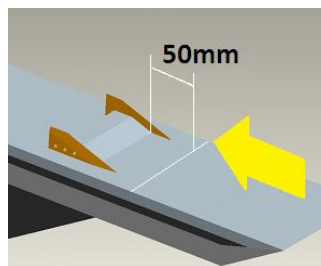
The boundary-layer velocity profiles of 20° ramp were obtained from velocity vector field of views and shown in Figure 24. In Figure 24, all the images shown were averaged from 439 images. The velocity profiles were taken every 5 mm from 50 mm upstream of the ramp corner to 5 mm upstream of the ramp corner.



(a) (b) (c) (d) (e)



(f) (g) (h) (i) (j)



(k)

Figure 24 The boundary-layer velocity profile on the 20° ramp (439 images averaged): (a) 50 mm upstream, (b) 45 mm upstream, (c) 40 mm upstream, (d) 35 mm upstream, (e) 30 mm upstream, (f) 25 mm upstream, (g) 20 mm upstream, (h) 15 mm upstream, (i) 10 mm upstream, and (j) 5 mm upstream of the ramp corner. (k) shows the location of 50 mm.

The 0 mm was set at the ramp corner. The flow direction is from right to left, refer to appendix D II for larger images. The negative sign in x axis means the flow is from right to left, and negative sign in y axis is due to the origin set in the free stream.

At 50 mm upstream, the profile appears to be that of a turbulent boundary layer. However, starting from 45 mm (Figure 24b), the profiles were affected by the strong shock/boundary-layer interaction. The separation bubble begins from 20 mm, which is in the Figure 24g. Although all (g), (h), (i), and (j) were in the separation bubble, only (j) was observed to have reverse flow at the very bottom. The reverse flow velocity measured was found to be 50 m/s. Originally, all (g), (h), (i), and (j) were expected to have the reverse flow due to the reason that they are inside the separation bubble. It is thought that the average on 439 images was still not enough to reveal the circulation inside the bubble.

4.5 Discussion

Attention was paid initially to the seeding issue and the interrogation area setup so as to produce good results. After that, boundary-layer velocity profiles were obtained for the flat plate. In order to define the boundary layer, the flat plate surface and the boundary-layer height should be determined. Section 4.3 details how to define flat plate surface, yet the boundary-layer height is still on working. Also, fluctuation phenomenon of the flat plate surface during the tests was discovered unexpectedly, and from our defining the surface the fluctuation was found to be $O(10\%)$ of the boundary-layer thickness. Hence, all the plotted boundary layer profiles in MATLAB were stitched to the same location according to their mean value. In the last section, the boundary-layer velocity profiles were obtained for the 20° ramp measurements. It was found that the profiles were affected from 45 mm upstream of the ramp corner. The future work will be placing the MVGs upstream (50 mm) of the ramp.

Chapter 5

The Experiment On Surface Flow Visualization

5.1 Introduction

In the present work, image processing was applied to surface oil flow visualization to capture features in the separation footprints of the 20° ramp and of MVGs combined with the ramp. Using image processing, the fuzzy (may due to the unsteadiness) but important separation line was revealed.

5.2 The Method

5.2.1 The Surface Oil Flow Visualization (SFV)

Creative use of SFVs by ultraviolet light and different fluorescent paints has effectively revealed numerous aspects of the complex flow field.¹² Figure 25 showed the preparation of the surface oil flow visualization. In the present work, a mixture of 2/6 fluorescent chalk + 1/6 kerosene + 3/6 silicone oil by volume was suitable. This mixture was not too thin, which leaves no footprint after test, and was also not too thick, whereby the paint would be too sticky to spread during the tests. More silicone oil than kerosene was used to reduce evaporation. Usually with just a little mixture for SFV in the low pressure condition in the wind tunnel, the kerosene vaporized very fast. The full image could not form under such a circumstance. Figure 26 shows a successful flow footprint.

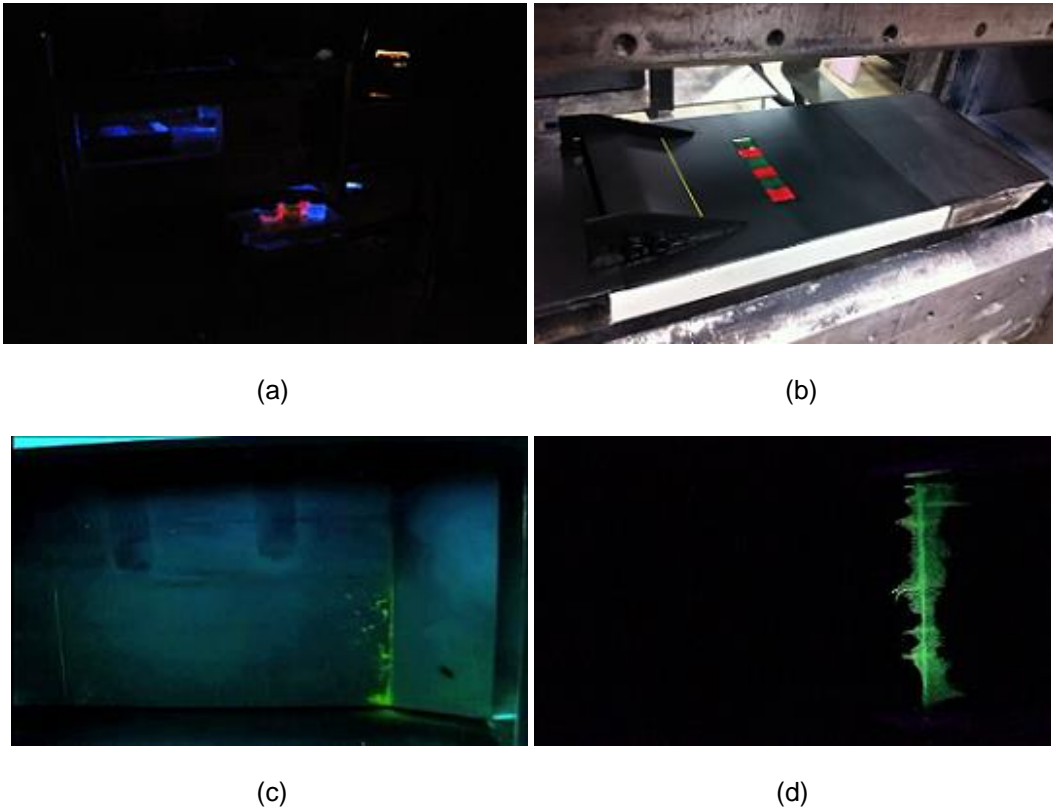


Figure 25 SFV was prepared by ultraviolet light and fluorescent paints: (a) Paints under the UV light, (b) preparation for tests, (c) result from a runny mixture, and (d) result from a sticky mixture.

5.2.2 Image Processing

5.2.2.1 Define The “Exp Line”

An image uploaded into MATLAB is shown in Figure 26. This image is recognized as pixels in MATLAB. Each pixel represents colors (RGB), red, green, and blue in three numbers and was stored in the assigned matrix B (see appendix C). Those three numbers individually show the RGB intensity. The command **imshow(B)** carried out the display of the image, and the command **imreadinfo** demonstrated the RGB numbers of each pixel and where the pixels are located, in (x,y), shown at the lower left corner in

Figure 26. Together these two commands showed the colored image. However, it is more precise to process the image in grayscale which only deals with the intensity without colors. Therefore another command **rbg2gray** was assigned to make the grayscale happened (Figure 27).

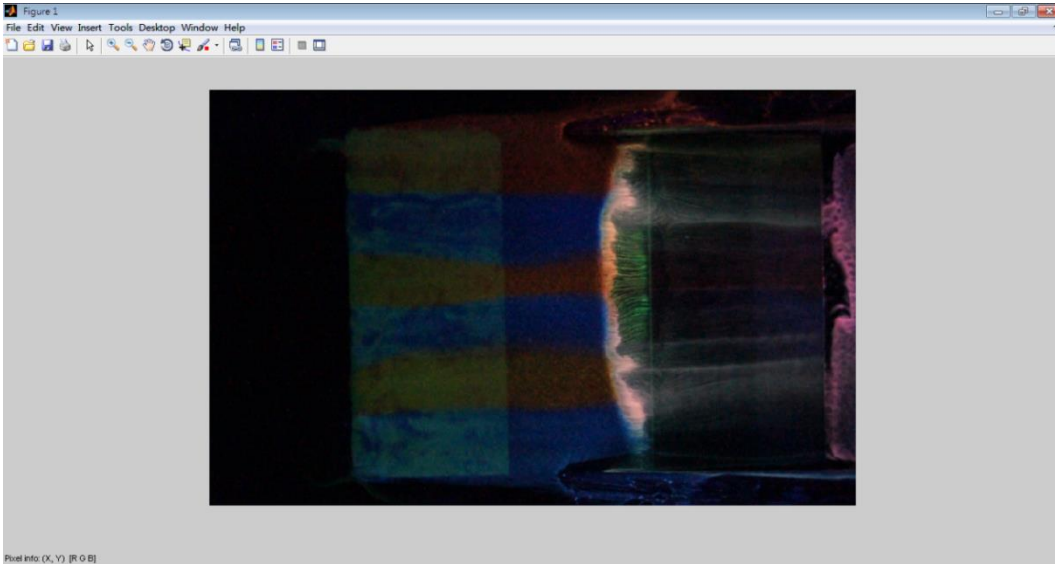


Figure 26 The uploaded image in RGB scale. The pixel information is at the lower left.

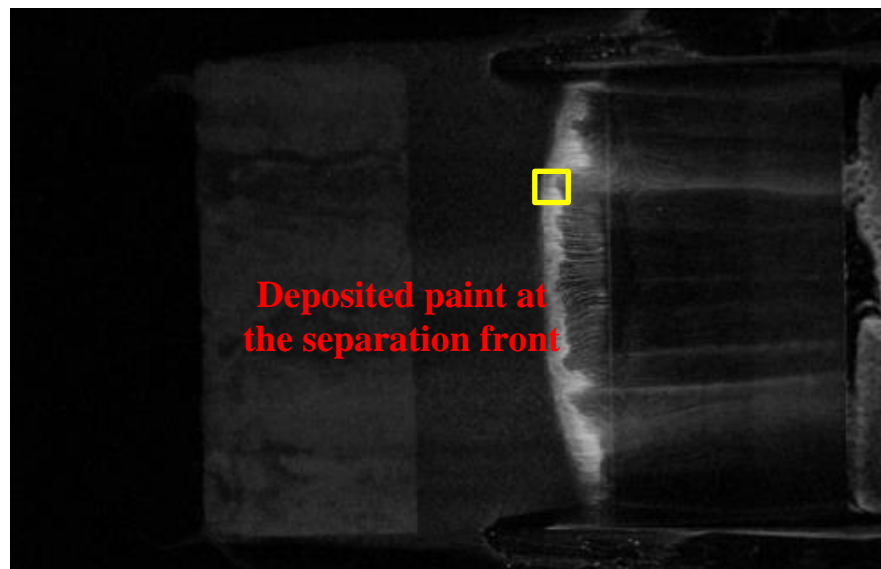


Figure 27 The grayscale scaling operation.

To find where the “exp line” is located, the attention was focused on the separation front where the mixture accumulated. As shown in Figure 27, the accumulation at the separation front is an irregular line which reflected more light than the surroundings so it appeared brighter in the image. However, if the image was zoomed in to the yellow rectangular area, shown in Figure 28, the irregular line is seen to be a thick area with many pixels on it. These pixels showed the intensity gradient across the middle of Figure 28. A more precise definition of the “exp line” across the intensity gradient is therefore needed.

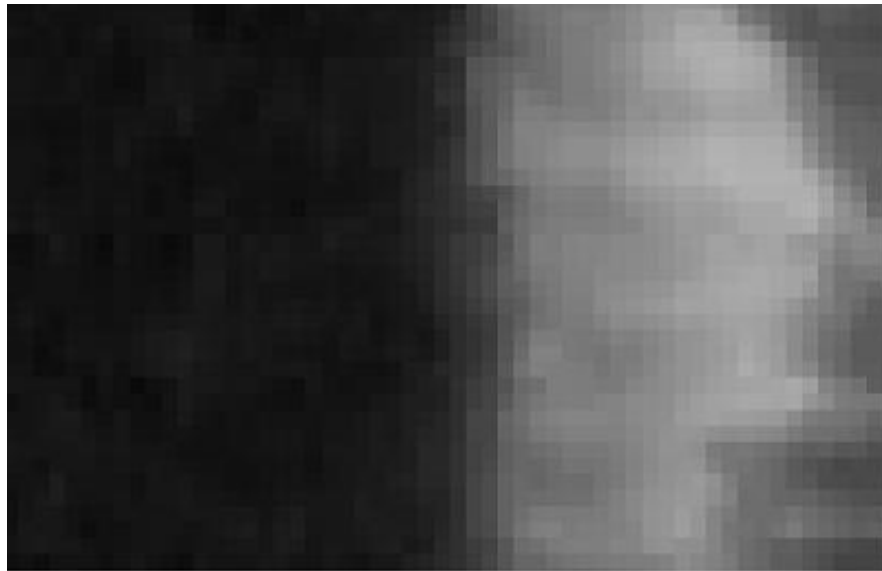


Figure 28 The zoom-in area with intensity gradient.

One way to do is to enhance the contrast (the command **imadjust**) as shown in Figure 29.

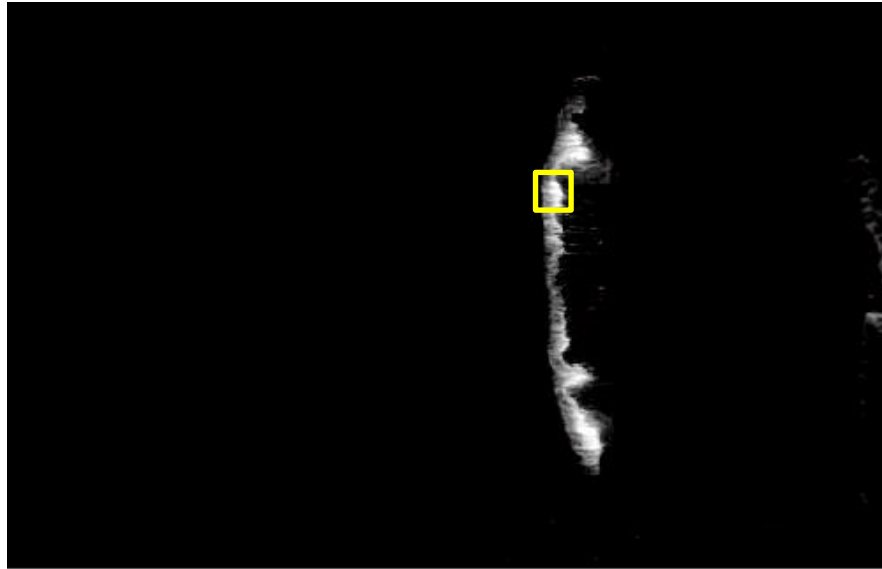


Figure 29 The contrast enhanced operation.

Again, if one checked the zoom-in view in the yellow rectangular area of Figure 29, it is not difficult to see the intensity gradient area reduced and the edge is found to be more distinct (Figure 30).

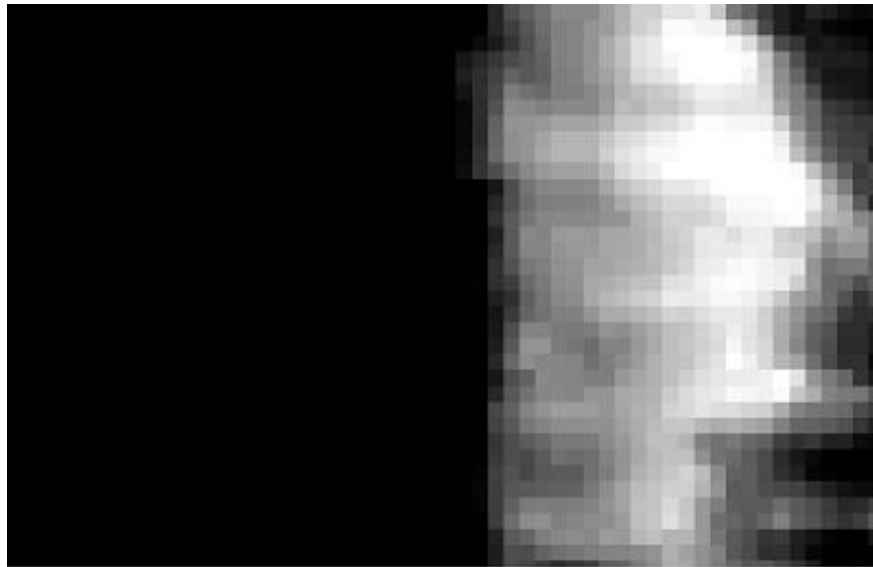


Figure 30 The pixels shown the intensity gradient area reduced (zoom-in view).

Next, the Sobel operator was used for precisely determining the location of the “exp line.” The Sobel operator is a mathematical algorithm commonly used for edge detection. The result is shown in Figure 31 after applying the Sobel operator to the command **filter2**.

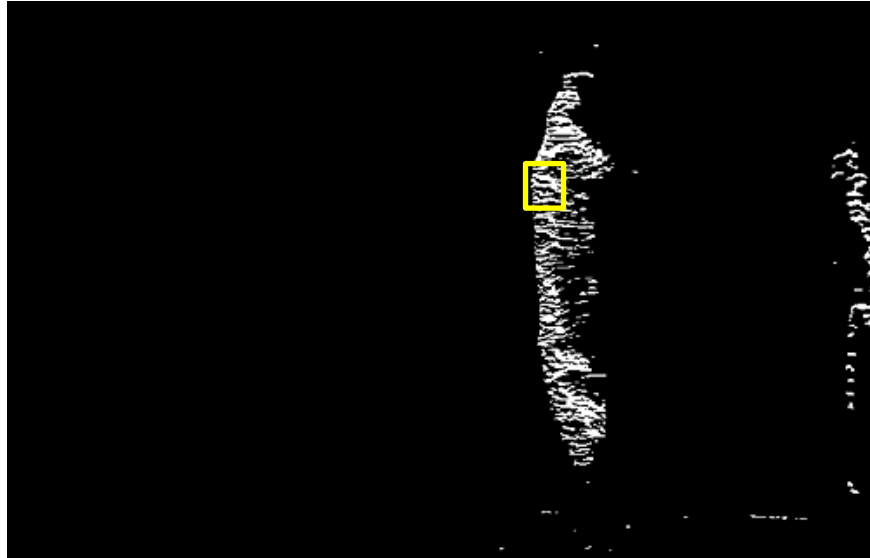


Figure 31 The edge sharpened operation.

Zooming in the same yellow rectangular area in Figure 31 reveals distinct black and white parts as shown in Figure 32. The “exp line” was defined in between these two parts.

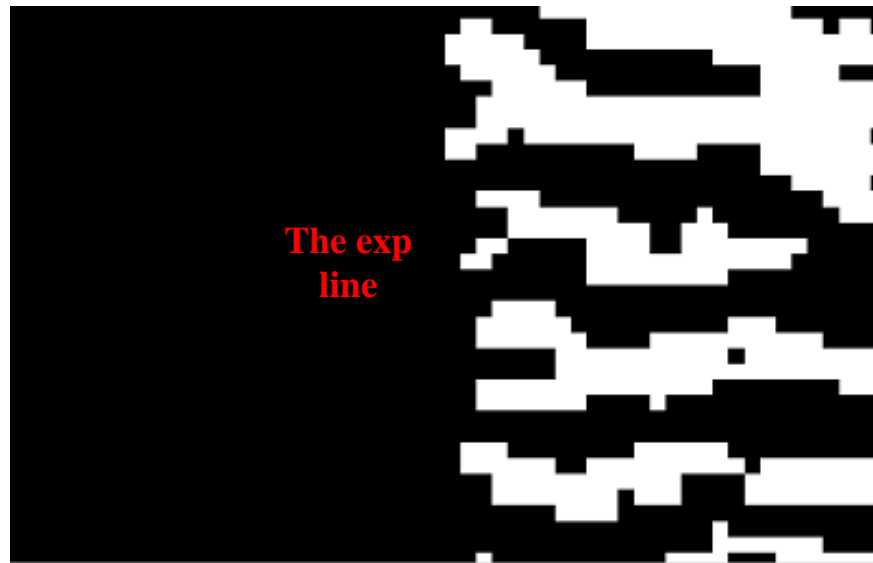


Figure 32 The pixels are now showing the distinct shapes and the “exp line” can be defined. This figure is the zoomed-in view.

Readers can also refer to appendix C II for the code fragment.

After the operations above, the “exp line” was defined and can be easily seen. In other words, the “exp line” is now clear and can be used for computation. In the matrix B, the pixels in the black region are represented by 0. On the other hand, those white pixels are represented by 1. The technique is as follows (appendix C III):

- 1) Using the command **find** to search the first non-zero pixel at the most upper row in the image.
- 2) Repeat the same operation for every row in the image. (Totally 398 rows)
- 3) Store the results in a vector. (Define the vector b)
- 4) Plot vector b against y. (Define y as y axis and b as x axis.)

Then one will obtain Figure 33.

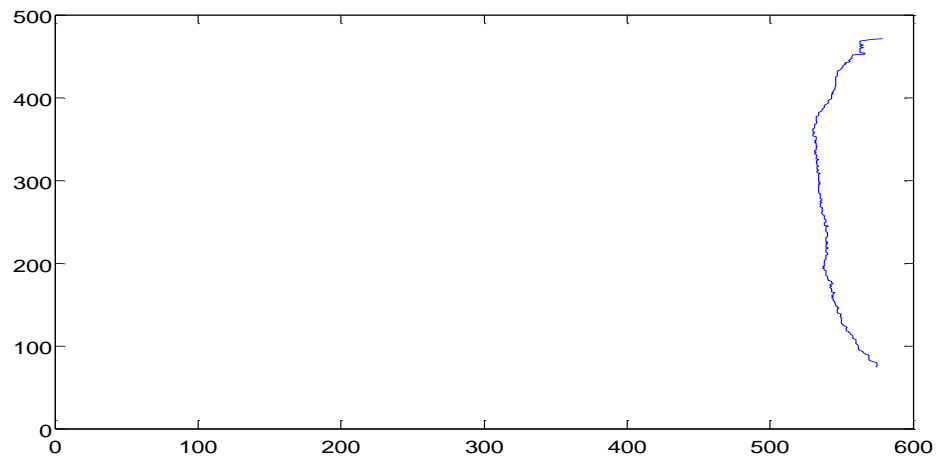


Figure 33 The located “exp line.

Also, the same image processing procedure was applied to the image of 20° ramp with three MVGs upstream. Thus, two “exp lines,” “exp line of 20° ramp” and “exp line of 20° ramp with three MVGs upstream” were obtained. Finally, one is able to define the index between a straight line and the “exp lines.” In fact, three other lines were designed and also the index was created to do the comparison.

5.2.2.2 Define A Few Lines For Comparison

In present paper, there were totally five lines defined: a straight line, a zigzag straight line, two “exp lines,” and an extreme zigzag line, see Figure 34.

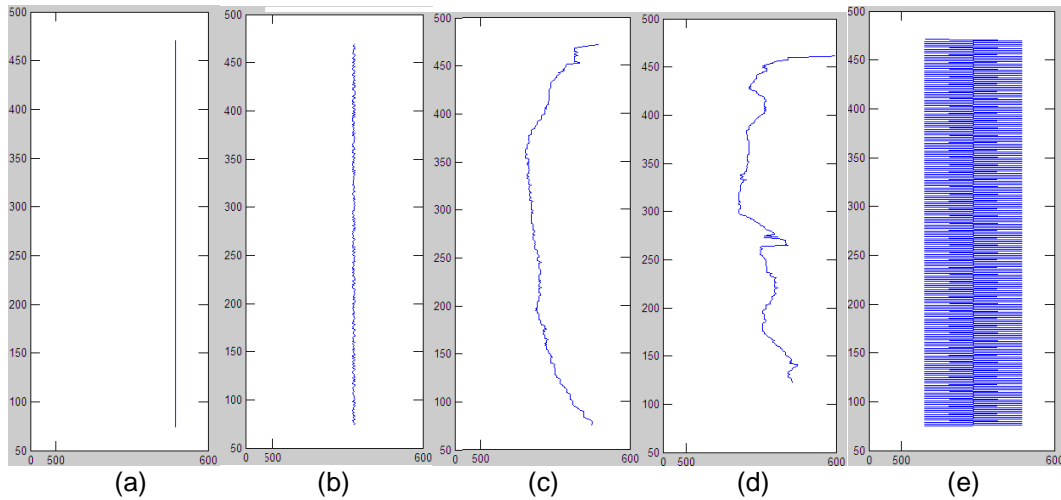


Figure 34 The five defined lines: (a) the straight line, (b) the zigzag straight line, (c) the “exp line of 20° ramp,” (d) the “exp line of 20° ramp with three MVGs upstream,” and (e) the extreme zigzag line.

First of all, a straight line can be easily defined by the code as shown in appendix C IV. Secondly, small fluctuation was applied to the straight line. The command **rand** was used for this purpose. The code fragment is reported in appendix C V. For an extreme zigzag line, one should assign a vector **z**. The numbers in **z** were designed in only 515 and 579 two integers in x axis, and keep repeating these two numbers down along y axis rotationally until **z** has totally 398 digit numbers. The numbers 515 and 579 were chosen based on being the same width as the “exp line of 20° ramp.” This defining way would be the most extreme fluctuated case in the 515-579 range that one can get limited by pixels. Again, y axis was set from 74 to 471, for totally range at 398 digit numbers. The reference code fragment is showing in appendix C VI.

5.2.2.3 Define The Index

Next, the index was defined and was applied to those five lines: The straight line, the zigzag straight line, the “exp line of 20° ramp,” the “exp line of 20° ramp with three MVGs upstream,” and the extreme zigzag line.

To define the index, two zigzag samples were designed. The zigzag sample refers how fluctuated a line can be. The index was defined as: the sum of all x direction fluctuations on that line. The fluctuation means how many pixels different in x direction between the y direction neighbor pixels of that line. For example, in Figure 35a, let the vertical 1, 2, 3,...,16, as y axis, the horizontal A, B, C,..., K, as x axis. The red zigzag sample represents a line with fluctuates. The index for Figure 35a was counted as:

$$(E,2) - (F,1) = 1$$

$$(F,3) - (E,2) = 1$$

$$(G,4) - (F,3) = 1$$

$$(F,5) - (G,4) = 1$$

$$(F,6) - (F,5) = 0$$

$$(F,7) - (F,6) = 0$$

$$(G,8) - (F,7) = 1$$

$$(F,9) - (G,8) = 1$$

$$(F,10) - (F,9) = 0$$

$$(F,11) - (F,10) = 0$$

$$(F,12) - (F,11) = 0$$

$$(F,13) - (F,12) = 0$$

$$(E,14) - (F,13) = 1$$

$$(F,15) - (E,14) = 1$$

$$(F,16) - (F,15) = 1$$

Add up all counts, the number is 9, the index was defined as 9 in this case. The other more fluctuated sample was also given as following: (Refer to Figure 35b)

$$(E,2) - (F,1) = 1$$

$$(D,3) - (E,2) = 1$$

$$(C,4) - (D,3) = 1$$

$$(B,5) - (C,4) = 1$$

$$(C,6) - (B,5) = 1$$

$$(G,7) - (C,6) = 4$$

$$(H,8) - (G,7) = 1$$

$$(J,9) - (H,8) = 2$$

$$(I,10) - (J,9) = 1$$

$$(H,11) - (I,10) = 1$$

$$(G,12) - (H,11) = 1$$

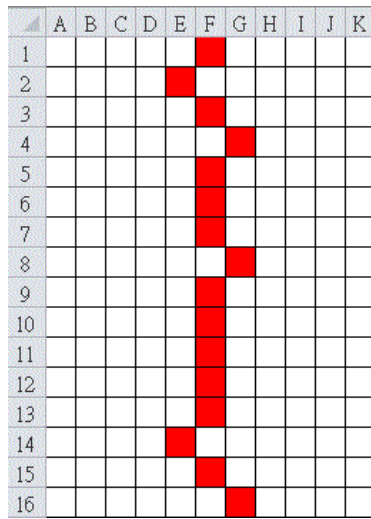
$$(G,13) - (G,12) = 0$$

$$(G,14) - (G,13) = 0$$

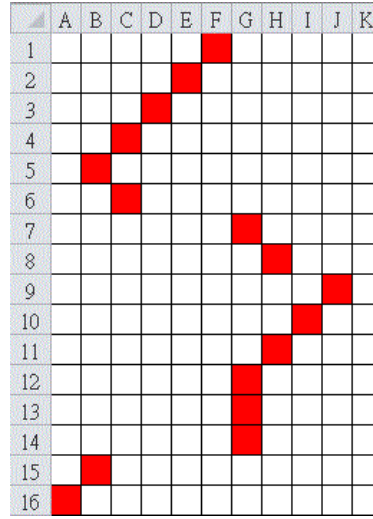
$$(B,15) - (G,14) = 5$$

$$(A,16) - (B,15) = 1$$

The total counts are 21. The index is therefore 21.



(a)



(b)

Figure 35 The zigzag samples with (a) small fluctuates, or (b) large fluctuates.

Apply the index (counts only from $y = 200$ to $y = 350$, between the two red bars, because the segment is the straightest one in the “exp line of 20° ramp.”) to those five lines, one had Table 4:

Table 4. The index and scaling of the five lines (this index seems to be sensitive to the small fluctuates.)

Index	0	60	105	132	9536
Scaling	0	0.63	1.10	1.38	100

The code fragment for index is reported in appendix C VII.

After defining the index (the counts), the scaling was the next step. The total counts of each case was taken to be linearly scaled from 0 to 100 (Take 9536 of the extreme zigzag line case as 100 and 0 of the straight line case as 0 for linear scaling). The results were not so expected because the case zigzag straight line is thought to be more similar to the straight line than the “exp line of 20° ramp” is, but the results showed the opposite way. Therefore, this index was concluded to be more sensitive to smaller fluctuates. An index is needed to be defined to more sensitive to large fluctuates.

For an index which is more sensitive to the large fluctuates, the strategy was attempting to sum of x direction pixels difference on a line in every other seven elements along the negative y direction. For example, again in Figure 35a:

$$(G,8) - (F,1) = 1$$

$$(F,9) - (E,2) = 1$$

$$(F,10) - (F,3) = 0$$

$$(F,11) - (G,4) = 1$$

$$(F,12) - (F,5) = 0$$

$$(F,13) - (F,6) = 0$$

$$(E,14) - (F,7) = 1$$

$$(F,15) - (G,8) = 1$$

$$(G,16) - (F,9) = 1$$

The index (total counts) is 6. And for the more fluctuates example again in Figure 35b,

$$(H,8) - (F,1) = 2$$

$$(J,9) - (E,2) = 5$$

$$(I,10) - (D,3) = 5$$

$$(H,11) - (C,4) = 5$$

$$(G,12) - (B,5) = 5$$

$$(G,13) - (C,6) = 4$$

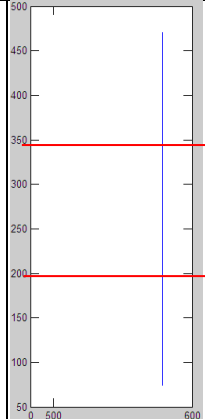
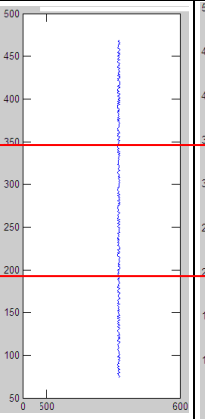
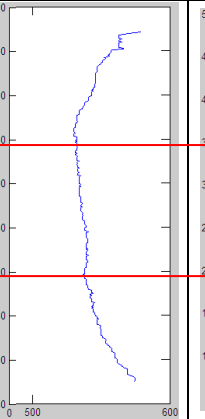
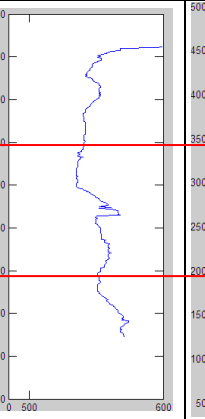
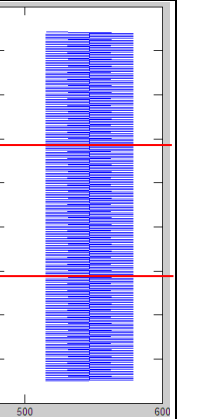
$$(G,14) - (G,7) = 0$$

$$(B,15) - (H,8) = 6$$

$$(A,16) - (J,9) = 9$$

The index is 41. Apply the index to those five lines, one had Table 5:

Table 5: The index and scaling of the five lines with the index sensitive to the large fluctuates

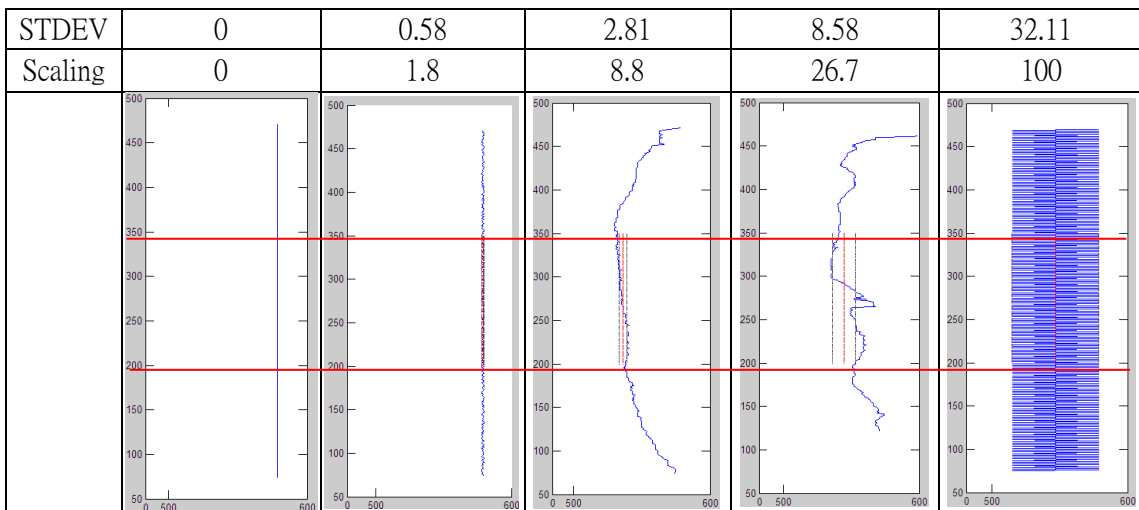
Index	0	99	108	456	9216
Scaling	0	1.07	1.17	4.95	100
					

The code fragment for index is reported in appendix C VIII.

The improvement can be seen as expected. The zigzag straight line is more similar to the straight line than “exp line of 20° ramp” is. From the results, one can estimate the effect of three MVGs on the separation area, just simply monitoring the index. Nevertheless, this method to estimate the effect of three MVGs on the separation area highly depends on its sensitive on large or small fluctuations. A more reliable method to carry out the estimation is needed.

The most basic and well-known statistical method, standard deviation, was then considered. By calculating the mean value of all five lines, one can easily obtain the standard deviation of these lines, and then do the estimation of how much effect of three MVGs on the separation area. Results showed in Table 6.

Table 6 standard deviation is to estimate the effect of MVGs on separation area. The red vertical dash lines indicate the mean values of each line, and two black vertical dash lines around each mean value are their standard deviations. The higher the standard deviation value, the more the line fluctuates.



5.3 The Discussion

In section 5, two indexes were defined to compare how straight or how fluctuated the “exp lines” are. The “exp lines” were compared to other three lines, and two totally different results were found. One result showed the “exp line of 20° ramp” is more similar to the straight line than zigzag straight line is. That was not expected. Therefore, this index was found to be more sensitive to small fluctuations. The other result based on the other index which is more sensitive to large fluctuations showed zigzag straight line is more similar to the straight line than the “exp line of 20° ramp” is. This result was thought

to be more reasonable, and has shown the three MVGs have an effect of index = 4.95 on the separation area, if the best straight case was index = 0 and the worst straight case was index = 100.

To be more precisely estimating the effect of three MVGs on the separation area, the standard deviation was applied. The standard deviation showed the three MVGs have an effect of 26.7 on the separation area, if the best straight case was 0 and the worst straight case was 100.

Chapter 6

Transient (Algebraic) Growth Analysis Of MVG Disturbance

6.1 Introduction

In order to understand the down-stream evolution (growth or decay) of the disturbance caused by MVG, the linearized perturbation growth problem is being investigated. From section 4, we obtained 350 of MVG down-stream boundary layer velocity profiles (5 mm down-stream of MVG). In Figure 36, the disturbed velocity profile is shown, after averaging of 350 profiles and operating of MATLAB command **polyfit** on power two and power three.

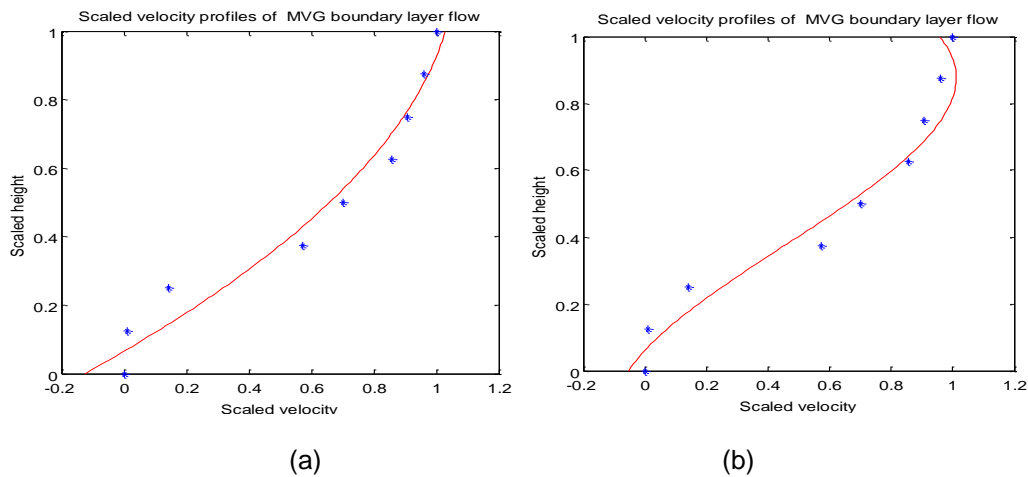


Figure 36 The disturbed boundary layer velocity profile 5 mm down-stream of MVG. Each blue star point is averaged from 350 instantaneous images. Red curve is the curve fitting in MATLAB with (a) power of 2, and (b) power of 3. Both height and velocity are linearly scaled as $y/\text{boundary-layer thickness}$ and $\text{boundary layer velocity}/\text{free-stream velocity}$.

The growth of a perturbation in the linearized regime of small deviations from the mean can be of two kinds: modal and transient¹³. Modal growth refers to the exponential growth of the direct modes, i.e. spatially developing wave solutions that can exist on their

own. Modal growth is important in transition studies where the magnitude of the initial perturbation is small and a single dominant (Tollmien-Schlichting) wave leads the transition process. Algebraic growth, conversely, refers to the growth of a combination of modes each of which decays spatially. Transient growth occurs because of the non-normality of the linearized equations (they are not self-adjoint), which implies the non-orthogonality of the basis for the invariant space of the perturbation. Transient growth is the main growth stage when the initial perturbation is large (as in the case of the MVG under consideration). In this case, the modal growth can be bypassed thanks to the much more efficient (albeit valid for short distances) transient growth mechanism.

The determination of transient growth can be divided in three steps: determination of the disturbance equations, integration of the equations in the boundary-layer and projection of the MVG disturbance on the basis formed by the modes. The first step is to define (Reynolds averaging) and solve the eigenvalue problem of disturbance field in the free-stream from linearized Navier-Stokes equations. We will call them disturbance equations for simplicity. The solutions of the disturbance equations are typically discrete eigenfunctions, known as Tollmien-Schlichting solutions. However, only discrete eigenfunctions could not form a complete set, mathematically. Grosch et al. suggested that there should be continuous eigenfunctions existed, and they are also solutions to the disturbance equations.¹⁴ In the present work, only the continuous eigenfunctions were considered and the frequency was set to be zero because we consider the spatial problem, not the temporal one, from our experimental data. Hence, we have no discrete eigenfunctions due to frequency the $\omega = 0$. Next, we solved the disturbance equations in the boundary-layer, where the mean properties, such as mean velocity, mean temperature and viscosity, vary with y axis. Each of the solution has both polynomials and sinusoidal exponential parts so all of the solutions are regarded as

improper eigenfunctions.¹⁴ The final step is to project the MVG disturbance onto those improper eigenfunctions and find out the coefficients. With knowing the coefficients, we will understand if the MVG disturbance is able to grow up or decay further downstream.

6.2 The Continuous Eigenfunctions In The Free-Stream

Assume zero-pressure-gradient along with streamwise, start from linearizing the two-dimensional compressible Navier-Stokes equations, the continuity equation, the energy equation, and the equation of state, one can obtain linearized equations (9b)- (9e).

$$\frac{\partial \rho}{\partial t} + \rho_s \frac{\partial u}{\partial x} + U_s \frac{\partial \rho}{\partial x} + \frac{\partial}{\partial y} (\rho_s v) = 0 \quad (9a)$$

$$\begin{aligned} & \rho_s \left(\frac{\partial u}{\partial t} + U_s \frac{\partial u}{\partial x} + v \frac{\partial U_s}{\partial y} \right) \\ = & -\frac{\partial \pi}{\partial x} + \frac{1}{Re} \left\{ \mu_s \frac{\partial}{\partial x} \left(r \frac{\partial u}{\partial x} + m \frac{\partial v}{\partial y} \right) + \frac{\partial}{\partial y} \left[\mu_s \left(\frac{\partial u}{\partial y} + \frac{\partial v}{\partial x} \right) + \mu \frac{\partial U_s}{\partial y} \right] \right\} \end{aligned} \quad (9b)$$

$$\begin{aligned} & \rho_s \left(\frac{\partial v}{\partial t} + U_s \frac{\partial v}{\partial x} \right) \\ = & -\frac{\partial \pi}{\partial y} + \frac{1}{Re} \left\{ \mu_s \frac{\partial}{\partial x} \left[\left(\frac{\partial u}{\partial y} + \frac{\partial v}{\partial x} \right) + \mu \frac{\partial U_s}{\partial y} \right] + \frac{\partial}{\partial y} \left[\mu_s \left(m \frac{\partial u}{\partial x} + r \frac{\partial v}{\partial y} \right) \right] \right\} \end{aligned} \quad (9c)$$

$$\begin{aligned} & \rho_s \left(\frac{\partial \theta}{\partial t} + U_s \frac{\partial \theta}{\partial x} + v \frac{\partial T_s}{\partial y} \right) \\ = & (\gamma - 1) M^2 \left\{ \frac{\partial \pi}{\partial t} + U_s \frac{\partial \pi}{\partial x} + \frac{1}{Re} \left[\mu_s 2 \left(\frac{\partial u}{\partial y} + \frac{\partial v}{\partial x} \right) \frac{\partial U_s}{\partial y} + \mu' \left(\frac{\partial U_s}{\partial y} \right)^2 \right] \right\} \\ & + \frac{1}{PrRe} \left[\mu_s \frac{\partial^2 \theta}{\partial x^2} + \frac{\partial}{\partial y} \left(\mu_s \frac{\partial \theta}{\partial y} + \mu \frac{\partial T_s}{\partial y} \right) \right] \end{aligned} \quad (9d)$$

$$\frac{\pi}{P_s} = \frac{\theta}{T_s} + \frac{\rho}{\rho_s} \quad (9e)$$

Following Fedorov and Tumin, (9b)- (9e) can be written for the disturbance vector function in matrix-operator form

$$\frac{\partial}{\partial y} \left(L_0 \frac{\partial A}{\partial y} \right) + \frac{\partial A}{\partial y} = H_{10} \frac{\partial A}{\partial t} + H_{11} A + H_2 \frac{\partial A}{\partial x} + H_3 \frac{\partial^2 A}{\partial x \partial y} + H_4 \frac{\partial^2 A}{\partial x^2} \quad (10)$$

Where the disturbance vector $A = \left[u \frac{\partial u}{\partial y} v \pi \theta \frac{\partial \theta}{\partial y} \right]^T$.

Then by assuming the plane wave $e^{i(\alpha x - \omega t)}$ as small perturbation in free stream, and substituting the plane wave into Eq. (10), the nonhomogeneous system of disturbance ordinary differential equations can be obtained as Eq. (11) below. The result would have been the same, if Fourier and Laplace transform were applied to Eq. (10) by requiring that the plane wave vanishes at infinity.

$$\frac{\partial}{\partial y} \left(L_0 \frac{\partial A}{\partial y} \right) + \frac{\partial A}{\partial y} = H_{10} \omega A - H_{10} A + H_{11} A + i\alpha H_2 A + i\alpha H_3 \frac{\partial A}{\partial y} + i\alpha^2 H_4 A \quad (11)$$

In Eq. (11), the elements in matrix A are function of ω and α . Eq. (11) can also be recast into a homogeneous system for standard stability ordinary differential equation for two-dimensional compressible boundary-layers,

$$\frac{\partial A}{\partial y} = H_0 A \quad (12)$$

The tricky part for recasting Eq. (11) into Eq. (12) happen in x and y momentum equations. For x momentum equation, the term $i\alpha H_3 \frac{\partial A}{\partial y}$ in Eq. (11) has to be substituted by continuity equation, Eq. (9a), to make sure there is no y derivative terms on the right hand side. For y momentum equation, turn the term $\frac{\partial}{\partial y} \left(L_0 \frac{\partial A}{\partial y} \right)$ into no y derivative terms by using twice of the continuity equation, Eq. (9a), and the equation of state, Eq. (9e). Also, the term $\frac{\mu_s}{Re} (m + 1)$ has to be arranged in H_2^{42} for easier calculations, otherwise it adds a difficulty (a y derivative term will be on the right hand side of y momentum equation) when that term was arranged in H_3^{41} . All the matrices shown above, L_0 , H_{10} , H_{11} , H_2 , H_3 , H_4 , and H_0 , can be found in Appendix F.

The next step is to solve the homogeneous Eq. (12) in the free-stream. It is a standard eigenvalue problem. As mentioned in the section 6.1, the continuous eigenfunctions will be searched for. Assuming the solution form as $e^{\lambda y}$, then λ here should be pure imaginary number for continuous modes. The conditions $\lambda \neq 0$, applies to discrete eigenfunctions. As an example, the difference between discrete eigenfunction and continuous eigenfunction is plotted in Figure 37. Where at $y \rightarrow \infty$ the magnitude $e^{\lambda y}$ is damped out for discrete eigenfunction, known as Tollmien–Schlichting solution, oppositely, at $y \rightarrow \infty$, the magnitude $e^{\lambda y}$ is bounded for continuous eigenfunction. The Tollmien–Schlichting solution can be represented as a physical wave, but continuous eigenfunction is a pure mathematical device only. The continuous eigenfunction alone cannot be represented any physical wave, but the superposed of them can be represented a physical perturbation. Substituting $e^{\lambda y}$ into Eq. (12), one can obtain the eigenvalues λ from the characteristic equation $\det||H_0 - \lambda I|| = 0$, for $y \rightarrow \infty$. These six eigenvalues are:

$$\lambda_{1,2} = \pm \sqrt{\alpha^2 + iRe(\alpha - i\omega)} \quad (13a)$$

$$\lambda_{3,4} = \pm \sqrt{\frac{b_{22} + b_{33}}{2} - \frac{\sqrt{(b_{22} - b_{33})^2 + 4b_{23}b_{32}}}{2}} \quad (13b)$$

$$\lambda_{5,6} = \pm \sqrt{\frac{b_{22} + b_{33}}{2} + \frac{\sqrt{(b_{22} - b_{33})^2 + 4b_{23}b_{32}}}{2}} \quad (13c)$$

Where $b_{22} = H_0^{42}H_0^{24} + H_0^{43}H_0^{34} + H_0^{46}H_0^{64}$, $b_{23} = H_0^{42}H_0^{25} + H_0^{43}H_0^{35} + H_0^{46}H_0^{65}$, $b_{32} = H_0^{64}$,
 $b_{33} = H_0^{65}$.

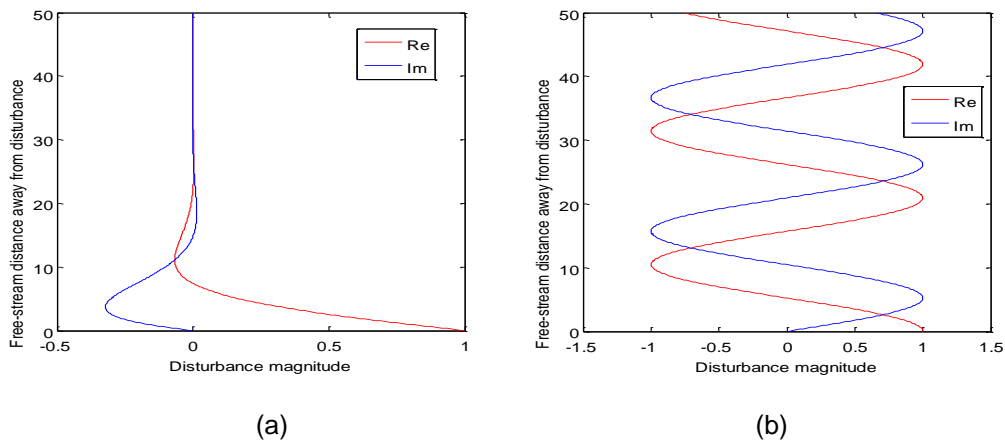


Figure 37 An example of (a) discrete eigenfunction solution, and (b) the continuous eigenfunction solution for disturbance equations. The discrete eigenfunction will eventually vanish at infinity in the free-stream, where continuous eigenfunction will be bounded.

By setting $\lambda = ik$, where k is set to be pure real number, the complex wavenumbers α for spatial instability problem were able to be calculated numerically. With a given k , one can obtain an α . A continuous spectrum λ is therefore formed by varying k . We found that the larger the value of k is ($\alpha(k)$ is found proportional to k), the lower the wavelength that $e^{\lambda y}$ exhibits. The plot (Re=500, reference from Grosch et al.) showing how $\alpha(k)$ affects the continuous eigenfunction $e^{\lambda y}$ are displayed in Figure 38.

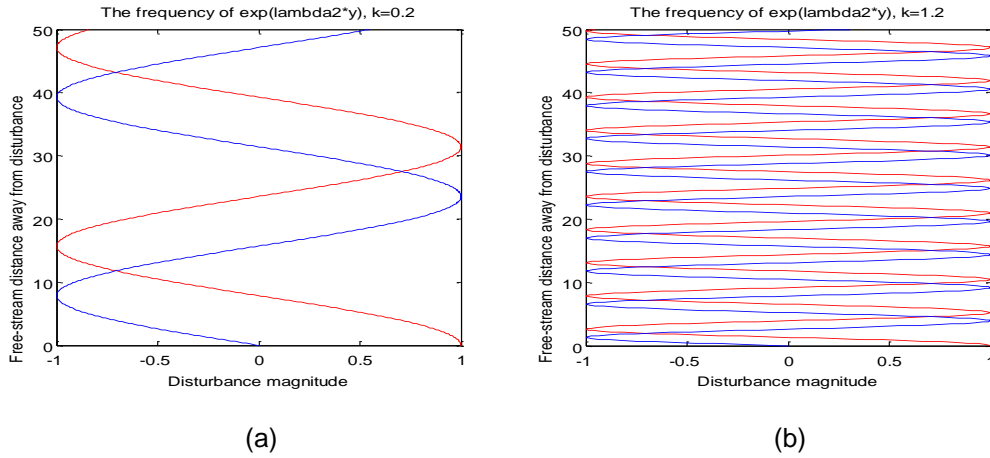


Figure 38 The variation in wavenumber of the continuous eigenfunction $e^{\lambda_2 y}$ with (a) $k = 0.2$ and (b) $k = 1.2$.

We expect that there are five branch-cuts in the α complex plane indicating where the free-stream perturbation is harmonic (i.e. λ is purely imaginary), as shown in Figure 39. The vorticity branch (green star) from $\lambda_{1,2}$ (Eq. 13a), the acoustic branches (red cross) from $\lambda_{3,4}$ (Eq. 13b), and the entropy branches (blue circle) from $\lambda_{5,6}$ (Eq. 13c). However, one of the acoustic branches and entropy branches coincide. Therefore, there are, effectively, four branches only. Figure 39 also shows branches plotted at $Re=500$ and $Re=381,470$ (typical of our wind tunnel experiments) for α .

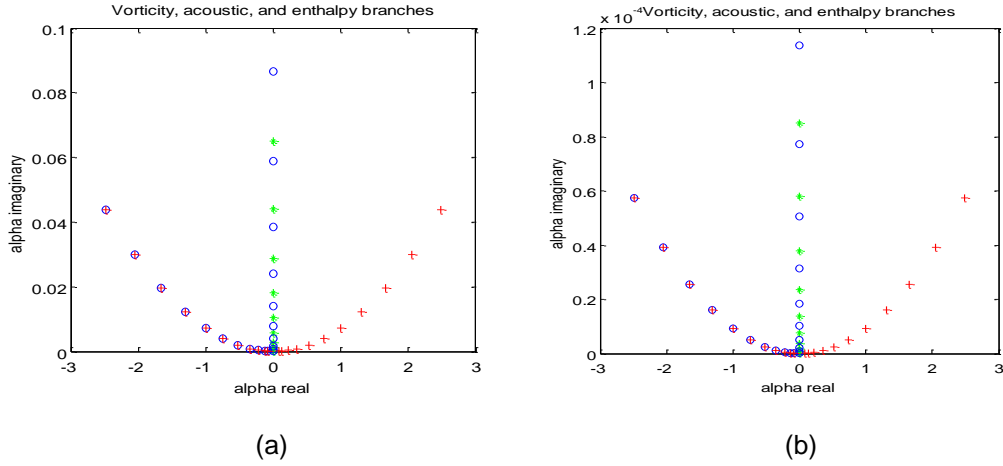


Figure 39 The branch plot of α in the complex plan: (a) $Re=500$, and (b) $Re=381,470$. The vorticity branch (green start) from $\lambda_{1,2}$, the acoustic branches (red cross) from $\lambda_{3,4}$, and the enthanpy branches (blue circle) from $\lambda_{5,6}$. Each branch has unlimited and continuous numbers but only ten of α plotted here.

6.3 The Eigenfunctions In The Boundary-Layer

In the present section, the continuous eigenfunctions found in section 6.2 will be applied to the disturbance equations and then integrated into the boundary layer.

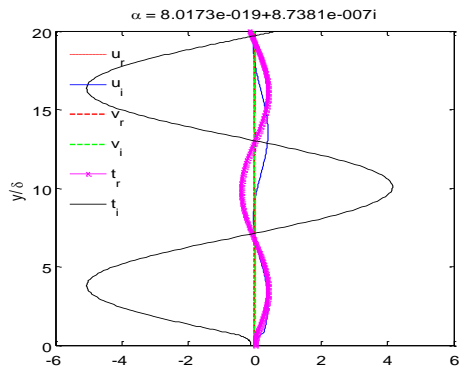
As the perturbation penetrates into boundary-layer, it will be affected by the gradient velocity profile at normal-wall direction. In other words, the U_s , T_s , and μ_s are not constant anymore in the H_0 matrix in Eq. (12). To solve Eq. (12), we again consider it as an eigenvalue problem. However, this time we assume a new form of solution and impose the free-stream boundary condition to Eq. (12). The solution form is assumed to be $H_0 A$, where A contains the continuous eigenfunction solution part we got from the free-stream, and multiplying a new variable ϕ_0 . Thus, the form of A is $\phi_0 e^{iky}$. Substituting A into Eq. (12) and rearranging the equation, we have

$$\lambda \phi_0 = -i H_0 \phi_0 \quad (14)$$

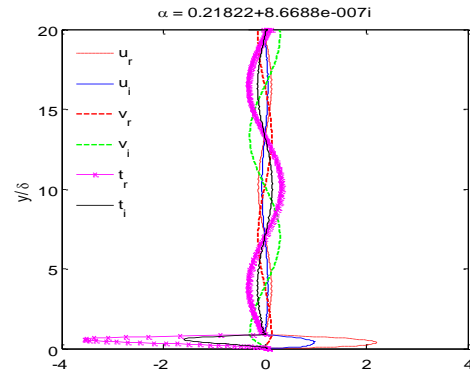
The $-i$ term can be absorbed into H_0 . On the other hand, the boundary condition at wall shall be that the magnitude $\phi_0 e^{iky}$ vanishes, and also, at the boundary-layer edge is that the magnitude e^{iky} , where $\phi_0 = 1$. Finally with Eq. (14), it is obvious an eigenvalue problem.

Next, to solve Eq. (14), the Chebyshev polynomial and collocation points method is applied. By expanding the eigenvector ϕ_0 with Chebyshev polynomials, ϕ_0 can be found by determining the coefficients in front of each Chebyshev basis. The Eq. (14) was solved numerically by plugging in all the free-stream properties. In the present work, the 20000 of collocation points were chosen to match the power two and three of the experimental curve modified by MATLAB command **polyfit**. Experimental curve can be referred in Figure 36.

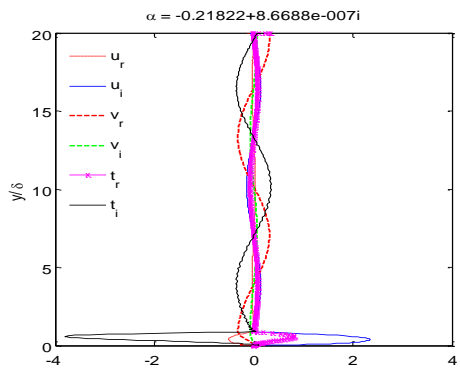
Figure 40 shows an investigation how the new eigenvector $\phi_0 e^{iky}$ behaves in the boundary-layer, at our experimental Reynolds number (381,470). We notice that the acoustic and entropy disturbance can penetrate into the boundary-layer, but not the vorticity one: vorticity signal is sheltered by boundary-layer. However, in Fedorov and Tumin their work, only the acoustic disturbance can penetrate into the boundary-layer but other two are sheltered by the boundary-layer. Moreover, in figure 41, we show that how different wavenumbers affect the disturbance in the boundary-layer (Reynolds number 381,470). If the k is larger (larger α) in the free-stream, then the disturbance (here the acoustic one for example) shrinks in the boundary-layer: boundary-layer acts as a low pass filter. In last Figure (Figure 42), the influence of Reynolds number on the disturbance in the boundary-layer is displayed. The result shows that a higher Reynolds number leads to an increase of the disturbance in the boundary-layer: high shear stress in boundary-layer amplifies the signal.



(a)

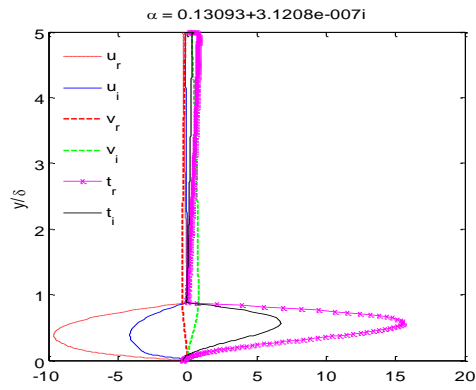


(b)

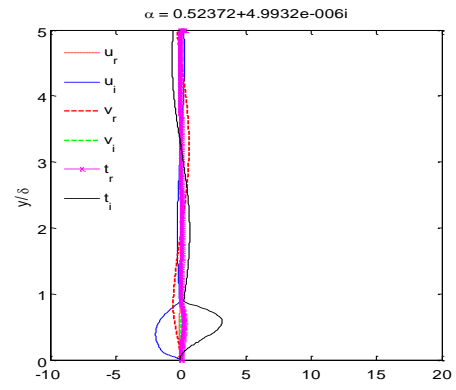


(c)

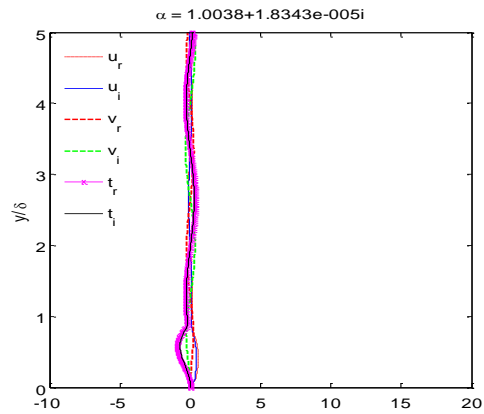
Figure 40 $k = 0.5$ for (a) vorticity branch, (b) acoustic branch, and (c) entropy branch. The y axis is normalized by boundary-layer thickness (at around 1) and the x axis is the magnitude of $e^{\lambda y}$ in the free-stream and of $\phi_0 e^{iky}$ in the boundary-layer. In the legend: u is the streamwise velocity component, v is the normal component and t is temperature perturbation.



(a)



(b)



(c)

Figure 41 The variation in wavenumber along the acoustic branch with (a) $k = 0.3$, (b) $k = 1.2$, and (c) $k = 2.3$. The y axis is normalized by boundary-layer thickness (at around 1) and the x axis is the magnitude of $e^{\lambda y}$ in the free-stream and of $\phi_0 e^{iky}$ in the boundary-layer. Note that the scale in y axis is from 0 to 5 boundary-layer thicknesses.

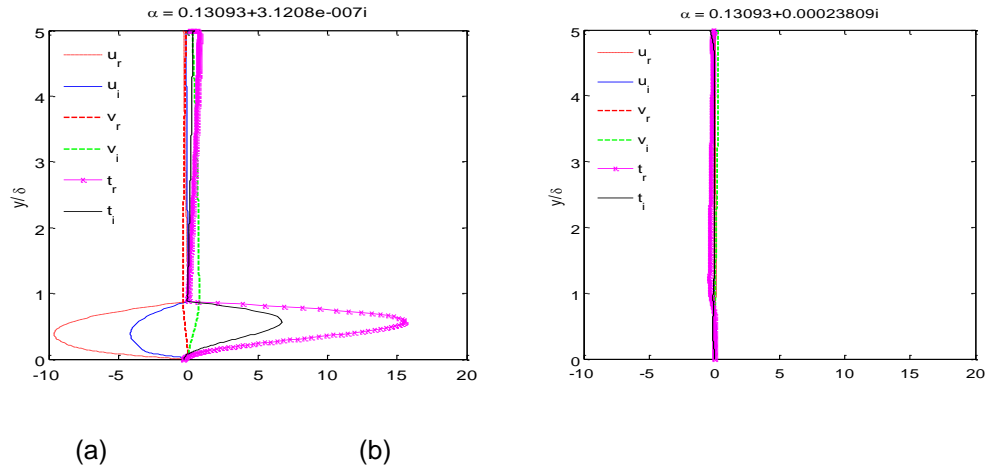


Figure 42 The influence of Reynolds number on the disturbance in the boundary-layer. The acoustic branch is taken for example. (a) $Re = 381,470$ and (b) $Re = 500$. The y axis is normalized by boundary-layer thickness (at around 1) and the x axis is the magnitude of $e^{\lambda y}$ in the free-stream and of $\phi_0 e^{iky}$ in the boundary-layer. Note that the scale in y axis is from 0 to 5 boundary-layer thickness.

6.4 Generate The Adjoint System

At all of the wavenumbers α , the vorticity, acoustic, and enthalpy branch cuts shown in Figure 39 have their own eigenvectors. These eigenvectors (modes) are regarded as basis (they can form a vector space) and the MVG disturbance from our experiment will be projected onto these basis. By calculating the coefficients of such projections, one can estimate how the sum of those modes results in a transient growth induced by the combination of fast decaying and slow persistent modes. Therefore, the MVG disturbance growth or decay downstream can be explained in terms of algebraic interaction of modes.

In order to calculate the coefficients, the orthogonality property between basis are critical. However, the matrix H_0 in the homogeneous system Eq. (12) is not a self-adjoint matrix, thus, its eigenvectors are not orthogonal to each other. Non-orthogonal

projections are difficult, thus a way to build up an orthogonality property into the basis has to be considered.

A bi-orthogonality condition can be reviewed in several papers.^{15, 16, 17} According to Salwen and Grosch (1981), the direct eigenvectors and adjoint eigenvectors from the linearized Navier-Stokes equations can be “orthogonal” to each other in some conditions. In the present case, it means the dot product of a direct eigenvector, a weight vector, and an adjoint eigenvector with different α will be equal to zero. Oppositely, the dot product will be equal to unity when α is the same. This is called the bi-orthogonality property between the direct system and the adjoint system. To take advantage of the bi-orthogonality condition, the adjoint eigenvectors must be found first.

The adjoint eigenvectors should be obtained from the solutions of the adjoint system of linearized Navier-Stokes equations. To find the equations, a mathematical tool known as the “Euler-Lagrange identity” is used. The left hand side is

$$\langle A, \left(\frac{\partial \hat{A}}{\partial y} + H_0 \hat{A} \right) \rangle = \nabla \cdot (A, \hat{A}). \quad (14)$$

In Eq. (14), time variation is not considered. The Euler-Lagrange identity states that the dot product of a direct vector and the adjoint system of equations is equal to the divergence of the dot product of the direct and the adjoint vectors. The expression in parentheses on the left hand side of Eq. (14) is found to be the adjoint system of the linearized Navier-Stokes equations if the parenthesis equals to zero. The divergence term, also called bilinear concomitant, is set to be zero by choosing a suitable boundary condition. Therefore, the left hand side dot product can be zero.

To derive the Euler-Lagrange identity, integration by parts should be applied to the direct system of the linearized Navier-Stokes equations. Suppose, first, that we have

the dot product $\langle \hat{A}, \left(\frac{\partial A}{\partial y} + H_0 A \right) \rangle$, thus, the continuity, x momentum, y momentum, and energy equations become

$$\iint_{x y} \hat{\pi} \cdot \left[\rho_s \frac{\partial u}{\partial x} + U_s \frac{\partial \rho}{\partial x} + \frac{\partial}{\partial y} (\rho_s v) \right] dy dx = 0 \quad (9ab)$$

$$\begin{aligned} \iint_{x y} \hat{u} \cdot \left[\rho_s \left(U_s \frac{\partial u}{\partial x} + v \frac{\partial U_s}{\partial y} \right) + \frac{\partial \pi}{\partial x} \right. \\ \left. - \frac{1}{Re} \left\{ \mu_s \frac{\partial}{\partial x} \left(r \frac{\partial u}{\partial x} + m \frac{\partial v}{\partial y} \right) + \frac{\partial}{\partial y} \left[\mu_s \left(\frac{\partial u}{\partial y} + \frac{\partial v}{\partial x} \right) + \mu \frac{\partial U_s}{\partial y} \right] \right\} \right] dy dx \\ = 0 \end{aligned} \quad (9bb)$$

$$\begin{aligned} \iint_{x y} \hat{v} \cdot \left[\rho_s \left(U_s \frac{\partial v}{\partial x} \right) + \frac{\partial \pi}{\partial y} - \frac{1}{Re} \left\{ \mu_s \frac{\partial}{\partial x} \left[\left(\frac{\partial u}{\partial y} + \frac{\partial v}{\partial x} \right) + \mu \frac{\partial U_s}{\partial y} \right] + \frac{\partial}{\partial y} \left[\mu_s \left(m \frac{\partial u}{\partial x} + r \frac{\partial v}{\partial y} \right) \right] \right\} \right] dy dx \\ = 0 \end{aligned} \quad (9cb)$$

$$\begin{aligned} \iint_{x y} \hat{\theta} \\ \cdot \left[\rho_s \left(U_s \frac{\partial \theta}{\partial x} + v \frac{\partial T_s}{\partial y} \right) - (\gamma - 1) M^2 \left\{ \frac{\partial \pi}{\partial t} + U_s \frac{\partial \pi}{\partial x} + \frac{1}{Re} \left[\mu_s 2 \left(\frac{\partial u}{\partial y} + \frac{\partial v}{\partial x} \right) \frac{\partial U_s}{\partial y} + \mu' \left(\frac{\partial U_s}{\partial y} \right)^2 \right] \right\} \right. \\ \left. - \frac{1}{Pr Re} \left[\mu_s \frac{\partial^2 \theta}{\partial x^2} + \frac{\partial}{\partial y} \left(\mu_s \frac{\partial \theta}{\partial y} + \mu \frac{\partial T_s}{\partial y} \right) \right] \right] dy dx \\ = 0 \end{aligned} \quad (9db)$$

where

$$\rho = \rho_s \left(\frac{\pi}{P_s} - \frac{\theta}{T_s} \right). \quad (9e)$$

The equation of state, Eq. (9e) is used here for expressing the density variable appearing in the continuity equation Eq. (9ab) into pressure and temperature variables.

The sum of all four equations makes a new long equation that represents the dot product of $\langle \hat{A}, \left(\frac{\partial A}{\partial y} + H_0 A \right) \rangle$, which is then expressed as $\iint_{x,y} \{ \hat{u}[x \text{ momentum eq.}] + \hat{v}[y \text{ momentum eq.}] + \hat{\pi}[\text{continuity eq.}] + \hat{\theta}[\text{energy eq.}] \} dydx = 0$. The goal is to turn $\langle \hat{A}, \left(\frac{\partial A}{\partial y} + H_0 A \right) \rangle$ into Euler-Lagrange identity, Eq. (14) by integration by parts. Take as an example the very first term, i.e., $\iint_{x,y} \hat{u}[x \text{ momentum eq.}] dydx$, that is Eq. (9bb):

$$\begin{aligned}
 & \iint_{y,x} \hat{u} \rho_s U_s \frac{\partial u}{\partial x} dx dy \\
 &= \int_y \hat{u} \rho_s U_s u dy - \iint_{y,x} \hat{u} \rho_s u \frac{\partial U_s}{\partial x} dx dy - \iint_{y,x} \hat{u} u U_s \frac{\partial \rho_s}{\partial x} dx dy \\
 & \quad - \iint_{y,x} u \rho_s U_s \frac{\partial \hat{u}}{\partial x} dx dy \tag{14.1}
 \end{aligned}$$

The first term on right hand side is the bilinear concomitant (the divergence term), which is the term $\nabla \cdot (A, \hat{A})$ in Eq. (14). It is zero because there is no perturbation, such as u, v, π , and θ , at the wall and the boundary layer edge. This is a consequence of the boundary conditions for boundary layer flow. Then, the second and third terms are neglected because they are free stream properties with respect to x derivatives. The only term left is the last one, representing $\langle A, \left(\frac{\partial \hat{A}}{\partial y} + H_0 \hat{A} \right) \rangle$ in Eq. (14), with $\frac{\partial \hat{A}}{\partial y} = 0, A = u, H_0 = \rho_s U_s$, and $\hat{A} = \frac{\partial \hat{u}}{\partial x}$ in this example. After collecting all the u terms in all four equations, including the last term in Eq. (14.1), an expression is formed in a square bracket multiplied by u . By the same procedure, the variables v, π , and θ are factored out

forming three other equations, one per each variable. The long equation is expressed here in a symbolic form, $\iint_{x,y} \{u[\text{adjoint } x \text{ momentum eq if this expression is zero}] + v[\text{adjoint } y \text{ momentum eq if this expression is zero}] + \pi[\text{adjoint continuity eq if this expression is zero}] + \theta[\text{adjoint energy eq if this expression is zero}]\} dydx = 0$. Usually along the lines that the integral can be satisfied for any arbitrary choice of domain only if the integrand is equal to zero. Since this long equation in the curly bracket is equal to zero (only 0 can be integrated equal to 0) and u , v , π , and θ are all non-zero numbers, the only chance to obtain the adjoint system is for each individual expression in the square brackets to be zero. Therefore, in these four square brackets, the first expression is defined as the full adjoint x momentum equation, the second expression is defined as the full adjoint y momentum equation, the third one as the full adjoint continuity equation, and the fourth one as the full adjoint energy equation. After dropping the terms related to x derivatives of free stream properties, the four adjoint linearized Navier-Stokes equations are presented in a parallel form in the following section.

6.5 The Adjoint Linearized Navier-Stokes Equations And Their Solutions

The adjoint linearized Navier-Stokes system is composed of four equations; Eq. (15a) is the adjoint continuity equation, Eq. (15b) is the adjoint x momentum equation, Eq. (15c) is the adjoint y momentum equation, and, finally, Eq. (15d) is the adjoint energy equation.

$$\frac{\partial \hat{u}}{\partial x} + U_s \frac{\partial \hat{\theta}}{\partial x} - \frac{\partial \hat{v}}{\partial y} + \frac{\rho_s U_s}{P_s} \frac{\partial \hat{\pi}}{\partial x} = 0 \quad (15a)$$

$$-\rho_s U_s \frac{\partial \hat{u}}{\partial x}$$

$$\begin{aligned}
&= \rho_s \frac{\partial \hat{\pi}}{\partial x} - \frac{1}{Re} \left\{ \mu_s \frac{\partial}{\partial x} \left(r \frac{\partial \hat{u}}{\partial x} + m \frac{\partial \hat{v}}{\partial y} \right) \right. \\
&+ \left. \frac{\partial}{\partial y} \left[-\mu_s \left(\frac{\partial \hat{u}}{\partial y} + \frac{\partial \hat{v}}{\partial x} \right) + 2(\gamma - 1) M^2 \mu_s \hat{\theta} \frac{\partial U_s}{\partial y} \right] \right\} \quad (15b)
\end{aligned}$$

$$\begin{aligned}
&U_s \frac{\partial \hat{v}}{\partial x} \\
&= -\frac{\partial \hat{\pi}}{\partial y} + \frac{1}{\rho_s Re} \left\{ \mu_s \frac{\partial}{\partial x} \left[\left(\frac{\partial \hat{u}}{\partial y} + \frac{\partial \hat{v}}{\partial x} \right) - 2(\gamma - 1) M^2 \hat{\theta} \frac{\partial U_s}{\partial y} \right] + \frac{\partial}{\partial y} \left[\mu_s \left(m \frac{\partial \hat{u}}{\partial x} + r \frac{\partial \hat{v}}{\partial y} \right) \right] \right\} + \hat{u} \frac{\partial U_s}{\partial y} \\
&+ \hat{\theta} \frac{\partial T_s}{\partial y} \quad (15c)
\end{aligned}$$

$$\begin{aligned}
&-\rho_s U_s \frac{\partial \hat{\theta}}{\partial x} \\
&= \left\{ \frac{-\rho_s U_s}{T_s} \frac{\partial \hat{\pi}}{\partial x} + \frac{1}{Re} \left[\frac{\partial \mu_s}{\partial \theta} \left(\frac{\partial \hat{u}}{\partial y} + \frac{\partial \hat{v}}{\partial x} \right) \frac{\partial U_s}{\partial y} - (\gamma - 1) M^2 \frac{\partial \mu_s}{\partial \theta} \left(\frac{\partial U_s}{\partial y} \right)^2 \hat{\theta} \right] \right\} \\
&- \frac{1}{Pr Re} \left[\mu_s \frac{\partial^2 \hat{\theta}}{\partial x^2} \right. \\
&+ \left. \frac{\partial}{\partial y} \left(\mu_s \frac{\partial \hat{\theta}}{\partial y} + \frac{\partial \mu_s}{\partial \theta} \frac{\partial T_s}{\partial y} \hat{\theta} \right) \right] \quad (15d)
\end{aligned}$$

The set equations (15) can be translated in the matrix-vector form shown in Eq.

(16)

$$\frac{\partial}{\partial y} \left(L_0 \frac{\partial \hat{A}}{\partial y} \right) + \frac{\partial \hat{A}}{\partial y} = H_{11} \hat{A} + H_2 \frac{\partial \hat{A}}{\partial x} + H_3 \frac{\partial^2 \hat{A}}{\partial x \partial y} + H_4 \frac{\partial^2 \hat{A}}{\partial x^2}, \quad (16)$$

where the disturbance vector is $\hat{A} = \left[\hat{u} \frac{\partial \hat{u}}{\partial y} \hat{v} \hat{\pi} \hat{\theta} \frac{\partial \hat{\theta}}{\partial y} \right]^T$. Applying the plane wave

solution method turns Eq. (16) into Eq. (17),

$$\frac{\partial}{\partial y} \left(L_0 \frac{\partial \hat{A}}{\partial y} \right) + \frac{\partial \hat{A}}{\partial y} = H_{11} \hat{A} + i\alpha H_2 \hat{A} + i\alpha H_3 \frac{\partial \hat{A}}{\partial y} + i\alpha^2 H_4 \hat{A} \quad (17)$$

With the same operations as in section 6.2, the nonhomogeneous adjoint system of disturbance (i.e., ordinary differential Eq. (17)) is recasted into the homogeneous one given in Eq. (18).

$$\frac{\partial \hat{A}}{\partial y} = -H_0^T \hat{A} \quad (18)$$

The method for recasting Eq. (17) into Eq. (18) in x and y momentum equations are similar to what was explained in section 6.2. Additional details regarding the implementation are shown below. Since the elements in the disturbance vector \hat{A} have been arranged as $\hat{A} = \left[\hat{u} \frac{\partial \hat{u}}{\partial y} \hat{v} \hat{\pi} \hat{\theta} \frac{\partial \hat{\theta}}{\partial y} \right]^T$, the x momentum equation, Eq. (15b), should be placed in the second column on both sides of Eq. (18). Along with this logic, the continuity, y momentum, and energy equations should be inserted in the third, fourth, and the last columns in both sides of Eq. (18). First notice that in the second column, the element $\frac{\partial \hat{u}}{\partial y}$ should be on the left hand side of Eq. (18), therefore in Eq. (17), the term $\frac{\partial^2 \hat{u}}{\partial y^2}$ was moved to the left hand side and all other terms were collected on the right hand side. Now the x momentum equation looks like

$$\begin{aligned} \mu_s \frac{\partial^2 \hat{u}}{\partial y^2} &= -\rho_s U_s \frac{\partial \hat{u}}{\partial x} + \rho_s \frac{\partial \hat{\pi}}{\partial x} \\ &- \frac{1}{Re} \left\{ \mu_s \frac{\partial}{\partial x} \left(r \frac{\partial \hat{u}}{\partial x} + m \frac{\partial \hat{v}}{\partial y} \right) - \frac{\partial \mu_s}{\partial y} \frac{\partial \hat{u}}{\partial y} \right. \\ &\left. + \frac{\partial}{\partial y} \left[-\mu_s \frac{\partial \hat{v}}{\partial x} + 2(\gamma - 1) M^2 \mu_s \hat{\theta} \frac{\partial U_s}{\partial y} \right] \right\} \end{aligned} \quad (15ba)$$

After expanding, applying the plane wave solutions, sorting out those components \hat{u} , $\frac{\partial \hat{u}}{\partial y}$, \hat{v} , $\hat{\pi}$, $\hat{\theta}$, $\frac{\partial \hat{\theta}}{\partial y}$, and dividing by μ_s , Eq. (15ba) becomes:

$$\begin{aligned}
\frac{\partial^2 \hat{u}}{\partial y^2} = & \left[0 \cdot \hat{u} - \frac{1}{\mu_s} \frac{\partial \mu_s}{\partial y} \cdot \frac{\partial \hat{u}}{\partial y} + 0 \cdot \hat{v} + 0 \cdot \hat{\pi} + \left(\frac{2(\gamma - 1)M^2}{\mu_s} \frac{\partial \mu_s}{\partial y} \frac{\partial U_s}{\partial y} + 2(\gamma - 1)M^2 \frac{\partial^2 U_s}{\partial y^2} \right) \cdot \hat{\theta} \right. \\
& \left. + 2(\gamma - 1)M^2 \frac{\partial U_s}{\partial y} \cdot \frac{\partial \hat{\theta}}{\partial y} \right] \\
& + i\alpha \left[\frac{\rho_s Re U_s}{\mu_s} \cdot \hat{u} + 0 \cdot \frac{\partial \hat{u}}{\partial y} + \left(-\frac{1}{\mu_s} \frac{\partial \mu_s}{\partial y} \right) \cdot \hat{v} + \frac{\rho_s Re}{\mu_s} \cdot \hat{\pi} + 0 \cdot \hat{\theta} + 0 \cdot \frac{\partial \hat{\theta}}{\partial y} \right] \\
& + i\alpha \frac{\partial}{\partial y} \left[0 \cdot \hat{u} + 0 \cdot \frac{\partial \hat{u}}{\partial y} + (-m - 1) \cdot \hat{v} + 0 \cdot \hat{\pi} + 0 \cdot \hat{\theta} + 0 \cdot \frac{\partial \hat{\theta}}{\partial y} \right] \\
& + i\alpha^2 \left[-r \cdot \hat{u} + 0 \cdot \frac{\partial \hat{u}}{\partial y} + 0 \cdot \hat{v} + 0 \cdot \hat{\pi} + 0 \cdot \hat{\theta} + 0 \cdot \frac{\partial \hat{\theta}}{\partial y} \right] \quad (15bb)
\end{aligned}$$

Eq. (15 bb) is of the same form as Eq. (17) (at the second column in Eq. (18)), where on the left hand side L_0 is zero, and on the right hand side H_{11} , H_2 , H_3 , and H_4 are the first, second, third, and fourth square brackets. Now, in order to remove the y derivative term $-i\alpha(m+1) \frac{\partial \hat{v}}{\partial y}$ (here it is $i\alpha H_3 \frac{\partial \hat{A}}{\partial y}$), the continuity equation $\frac{\partial \hat{v}}{\partial y} = i\alpha \left[1 \cdot \hat{u} + 0 \cdot \frac{\partial \hat{u}}{\partial y} + 0 \cdot \hat{v} + \frac{\rho_s U_s}{P_s} \cdot \hat{\pi} + U_s \cdot \hat{\theta} + 0 \cdot \frac{\partial \hat{\theta}}{\partial y} \right]$ (this is after expanding, applying the plane wave solutions, and sorting out those components), was multiplied by $-i\alpha(m+1)$ and substituting for the term $-i\alpha(m+1) \frac{\partial \hat{v}}{\partial y}$:

$$\begin{aligned}
\frac{\partial^2 \hat{u}}{\partial y^2} = & \left[0 \cdot \hat{u} - \frac{1}{\mu_s} \frac{\partial \mu_s}{\partial y} \cdot \frac{\partial \hat{u}}{\partial y} + 0 \cdot \hat{v} + 0 \cdot \hat{\pi} + \left(\frac{2(\gamma - 1)M^2}{\mu_s} \frac{\partial \mu_s}{\partial y} \frac{\partial U_s}{\partial y} + 2(\gamma - 1)M^2 \frac{\partial^2 U_s}{\partial y^2} \right) \cdot \hat{\theta} \right. \\
& \left. + 2(\gamma - 1)M^2 \frac{\partial U_s}{\partial y} \cdot \frac{\partial \hat{\theta}}{\partial y} \right] \\
& + i\alpha \left[\frac{\rho_s Re U_s}{\mu_s} \cdot \hat{u} + 0 \cdot \frac{\partial \hat{u}}{\partial y} + \left(-\frac{1}{\mu_s} \frac{\partial \mu_s}{\partial y} \right) \cdot \hat{v} + \frac{\rho_s Re}{\mu_s} \cdot \hat{\pi} + 0 \cdot \hat{\theta} + 0 \cdot \frac{\partial \hat{\theta}}{\partial y} \right] \\
& + \left[-i\alpha(m+1) \cdot i\alpha \left(1 \cdot \hat{u} + 0 \cdot \frac{\partial \hat{u}}{\partial y} + 0 \cdot \hat{v} + \frac{\rho_s U_s}{P_s} \cdot \hat{\pi} + U_s \cdot \hat{\theta} + 0 \cdot \frac{\partial \hat{\theta}}{\partial y} \right) \right] \\
& + i\alpha^2 \left[-r \cdot \hat{u} + 0 \cdot \frac{\partial \hat{u}}{\partial y} + 0 \cdot \hat{v} + 0 \cdot \hat{\pi} + 0 \cdot \hat{\theta} + 0 \cdot \frac{\partial \hat{\theta}}{\partial y} \right] \quad (15bc)
\end{aligned}$$

After collecting all \hat{u} terms together, all $\frac{\partial \hat{u}}{\partial y}$ terms together, all \hat{v} terms together,

etc., it becomes:

$$\begin{aligned}
\frac{\partial}{\partial y} \left(\frac{\partial \hat{u}}{\partial y} \right) &= \left[i\alpha \frac{\rho_s Re U_s}{\mu_s} + \alpha^2(m+1) + i\alpha^2(-r) \right] \hat{u} + \left[-\frac{1}{\mu_s} \frac{\partial \mu_s}{\partial y} \right] \frac{\partial \hat{u}}{\partial y} + \left[i\alpha \left(-\frac{1}{\mu_s} \frac{\partial \mu_s}{\partial y} \right) \right] \hat{v} \\
&+ \left[i\alpha \frac{\rho_s Re}{\mu_s} + \alpha^2(m+1) \frac{\rho_s U_s}{P_s} \right] \hat{\pi} \\
&+ \left[\left(\frac{2(\gamma-1)M^2}{\mu_s} \frac{\partial \mu_s}{\partial y} \frac{\partial U_s}{\partial y} + 2(\gamma-1)M^2 \frac{\partial^2 U_s}{\partial y^2} \right) + \alpha^2(m+1)U_s \right] \hat{\theta} \\
&+ \left[2(\gamma-1)M^2 \frac{\partial U_s}{\partial y} + \right] \frac{\partial \hat{\theta}}{\partial y}
\end{aligned} \tag{15bd}$$

Finally, Eq. (15bd) is at the second column of the form Eq. (18).

Moreover, at the fourth column, the term $\frac{\partial \hat{\pi}}{\partial y}$ is identified on the left hand side of Eq. (18), thus, the y momentum equation is to be implemented in this column. Therefore, in Eq. (17), the terms $\frac{\partial \hat{\pi}}{\partial y}$ and $\frac{\partial}{\partial y} \left(\frac{r\mu_s}{\rho_s Re} \frac{\partial \hat{v}}{\partial y} \right)$ are moved to the left hand side, the term $U_s \frac{\partial \hat{v}}{\partial x}$ is moved to the right hand side, and all other terms remain on the right hand side. Now the y momentum equation looks like

$$\begin{aligned}
&-\frac{\partial}{\partial y} \left(\frac{r\mu_s}{\rho_s Re} \frac{\partial \hat{v}}{\partial y} \right) + \frac{\partial \hat{\pi}}{\partial y} = -U_s \frac{\partial \hat{v}}{\partial x} \\
&+ \frac{1}{\rho_s Re} \left\{ \mu_s \frac{\partial}{\partial x} \left[\left(\frac{\partial \hat{u}}{\partial y} + \frac{\partial \hat{v}}{\partial x} \right) - 2(\gamma-1)M^2 \hat{\theta} \frac{\partial U_s}{\partial y} \right] + \frac{\partial}{\partial y} \left[\mu_s \left(m \frac{\partial \hat{u}}{\partial x} \right) \right] \right\} + \hat{u} \frac{\partial U_s}{\partial y} \\
&+ \hat{\theta} \frac{\partial T_s}{\partial y}.
\end{aligned} \tag{15ca}$$

Expanding, applying the plane wave solutions, and sorting out the components \hat{u} ,

$\frac{\partial \hat{u}}{\partial y}$, \hat{v} , $\hat{\pi}$, $\hat{\theta}$, $\frac{\partial \hat{\theta}}{\partial y}$, Eq. (15ca) becomes:

$$\begin{aligned}
& -\frac{\partial}{\partial y} \left(\frac{r\mu_s}{\rho_s Re} \frac{\partial \hat{v}}{\partial y} \right) + \frac{\partial \hat{\pi}}{\partial y} \\
& = \left[\frac{\partial U_s}{\partial y} \cdot \hat{u} + 0 \cdot \frac{\partial \hat{u}}{\partial y} + 0 \cdot \hat{v} + 0 \cdot \hat{\pi} + \frac{\partial T_s}{\partial y} \cdot \hat{\theta} + 0 \cdot \frac{\partial \hat{\theta}}{\partial y} \right] \\
& + i\alpha \left[\frac{m}{\rho_s Re} \frac{\partial \mu_s}{\partial y} \cdot \hat{u} + \frac{\mu_s(m+1)}{\rho_s Re} \cdot \frac{\partial \hat{u}}{\partial y} + (-U_s) \cdot \hat{v} + 0 \cdot \hat{\pi} \right. \\
& + \frac{1}{\rho_s Re} \left(-2(\gamma-1)M^2\mu_s \frac{\partial U_s}{\partial y} \right) \cdot \hat{\theta} + 0 \cdot \frac{\partial \hat{\theta}}{\partial y} \left. \right] \\
& + i\alpha \frac{\partial}{\partial y} \left[0 \cdot \hat{u} + 0 \cdot \frac{\partial \hat{u}}{\partial y} + 0 \cdot \hat{v} + 0 \cdot \hat{\pi} + 0 \cdot \hat{\theta} + 0 \cdot \frac{\partial \hat{\theta}}{\partial y} \right] \\
& + i\alpha^2 \left[0 \cdot \hat{u} + 0 \cdot \frac{\partial \hat{u}}{\partial y} + \frac{\mu_s}{\rho_s Re} \cdot \hat{v} + 0 \cdot \hat{\pi} + 0 \cdot \hat{\theta} + 0 \cdot \frac{\partial \hat{\theta}}{\partial y} \right] \tag{15cb}
\end{aligned}$$

Eq. (15 cb) is of the same form as Eq. (17) (see, the fourth column), where on the left hand side L_0 has the element $-\frac{r\mu_s}{\rho_s Re}$, and on the right hand side H_{11} , H_2 , H_3 , and H_4 contented elements in the first, second, third, and fourth parentheses. At this moment, remove the second order y derivative term $-\frac{\partial}{\partial y} \left(\frac{r\mu_s}{\rho_s Re} \frac{\partial \hat{v}}{\partial y} \right)$ (which is the term $\frac{\partial}{\partial y} \left(L_0 \frac{\partial \hat{A}}{\partial y} \right)$) away from Eq. (15cb) turns Eq. (15cb) into Eq. (18). With this idea, again the continuity equation $\frac{\partial \hat{v}}{\partial y} = i\alpha \left[1 \cdot \hat{u} + 0 \cdot \frac{\partial \hat{u}}{\partial y} + 0 \cdot \hat{v} + \frac{\rho_s U_s}{P_s} \cdot \hat{\pi} + U_s \cdot \hat{\theta} + 0 \cdot \frac{\partial \hat{\theta}}{\partial y} \right]$ is applied and substituting into this term $-\frac{\partial}{\partial y} \left(\frac{r\mu_s}{\rho_s Re} \frac{\partial \hat{v}}{\partial y} \right)$.

$$\begin{aligned}
& -\frac{\partial}{\partial y} \left(\frac{r\mu_s}{\rho_s Re} \left(i\alpha \left[1 \cdot \hat{u} + 0 \cdot \frac{\partial \hat{u}}{\partial y} + 0 \cdot \hat{v} + \frac{\rho_s U_s}{P_s} \cdot \hat{\pi} + U_s \cdot \hat{\theta} + 0 \cdot \frac{\partial \hat{\theta}}{\partial y} \right] \right) \right) + \frac{\partial \hat{\pi}}{\partial y} \\
& = \left[\frac{\partial U_s}{\partial y} \cdot \hat{u} + 0 \cdot \frac{\partial \hat{u}}{\partial y} + 0 \cdot \hat{v} + 0 \cdot \hat{\pi} + \frac{\partial T_s}{\partial y} \cdot \hat{\theta} + 0 \cdot \frac{\partial \hat{\theta}}{\partial y} \right] \\
& + i\alpha \left[\frac{m}{\rho_s Re} \frac{\partial \mu_s}{\partial y} \cdot \hat{u} + \frac{\mu_s(m+1)}{\rho_s Re} \cdot \frac{\partial \hat{u}}{\partial y} + (-U_s) \cdot \hat{v} + 0 \cdot \hat{\pi} \right. \\
& + \frac{1}{\rho_s Re} \left(-2(\gamma-1)M^2\mu_s \frac{\partial U_s}{\partial y} \right) \cdot \hat{\theta} + 0 \cdot \frac{\partial \hat{\theta}}{\partial y} \left. \right] \\
& + i\alpha \frac{\partial}{\partial y} \left[0 \cdot \hat{u} + 0 \cdot \frac{\partial \hat{u}}{\partial y} + 0 \cdot \hat{v} + 0 \cdot \hat{\pi} + 0 \cdot \hat{\theta} + 0 \cdot \frac{\partial \hat{\theta}}{\partial y} \right] \\
& + i\alpha^2 \left[0 \cdot \hat{u} + 0 \cdot \frac{\partial \hat{u}}{\partial y} + \frac{\mu_s}{\rho_s Re} \cdot \hat{v} + 0 \cdot \hat{\pi} + 0 \cdot \hat{\theta} + 0 \cdot \frac{\partial \hat{\theta}}{\partial y} \right] \tag{15cc}
\end{aligned}$$

Performing the derivative of y on the first term of Eq. (15cc), rearranging, and collecting all \hat{u} terms together, all $\frac{\partial \hat{u}}{\partial y}$ terms together, all \hat{v} terms together, etc., leads to

$$\begin{aligned}
\frac{\partial}{\partial y} (\hat{\pi}) & = \frac{1}{1 - \frac{rU_s\mu_s}{P_s Re}} \left\{ \left[\frac{\partial U_s}{\partial y} + i\alpha \frac{(m+r)\partial\mu_s}{\rho_s Re} \right] \hat{u} + \left[i\alpha \frac{\mu_s(m+r+1)}{\rho_s Re} \right] \frac{\partial \hat{u}}{\partial y} \right. \\
& + \left[i\alpha(-U_s) + i\alpha^2 \frac{\mu_s}{\rho_s Re} \right] \hat{v} + \left[i\alpha \frac{\partial \mu_s}{\partial y} \frac{rU_s}{P_s Re} \right] \hat{\pi} \\
& + \left[\frac{\partial T_s}{\partial y} + i\alpha \frac{1}{\rho_s Re} \left(-2(\gamma-1)M^2\mu_s \frac{\partial U_s}{\partial y} + rU_s \frac{\partial \mu_s}{\partial y} \right) \right] \hat{\theta} \\
& \left. + \left[i\alpha \frac{r\mu_s U_s}{\rho_s Re} \right] \frac{\partial \hat{\theta}}{\partial y} \right\}. \tag{15cd}
\end{aligned}$$

Finally, Eq. (15cd) is at the fourth column of the form Eq. (18).

Meanwhile, the energy equation is relatively simple. One can easily expand and arrange Eq. (15d) into the matrix-vector form of Eq. (17), and collect all \hat{u} terms together, all $\frac{\partial \hat{u}}{\partial y}$ terms together, all \hat{v} terms together, etc. to gain Eq. (18) (note the term $\frac{\partial \hat{\theta}}{\partial y}$ is in the sixth column):

$$\begin{aligned}
\frac{\partial}{\partial y} \left(\frac{\partial \hat{\theta}}{\partial y} \right) &= [0] \hat{u} + \left[\frac{Pr}{\mu_s} \frac{\partial \mu_s}{\partial \theta} \frac{\partial U_s}{\partial y} \right] \frac{\partial \hat{u}}{\partial y} + \left[i\alpha \frac{Pr}{\mu_s} \frac{\partial \mu_s}{\partial \theta} \frac{\partial U_s}{\partial y} \right] \hat{v} + \left[i\alpha \left(-\frac{Pr Re \rho_s U_s}{T_s \mu_s} \right) \right] \hat{\pi} \\
&+ \left[-\frac{(\gamma - 1) M^2 Pr}{\mu_s} \frac{\partial \mu_s}{\partial \theta} \left(\frac{\partial U_s}{\partial y} \right)^2 + i\alpha \left(\frac{Pr Re \rho_s U_s}{\mu_s} \right) + \alpha^2 \right] \hat{\theta} \\
&+ \left[-\frac{1}{\mu_s} \frac{\partial \mu_s}{\partial y} + \frac{1}{\mu_s} \frac{\partial \mu_s}{\partial y} \frac{\partial T_s}{\partial y} \right] \frac{\partial \hat{\theta}}{\partial y} \quad (15dd)
\end{aligned}$$

Finally the leading order of the adjoint system of linearized Navier-Stokes equations is shown in Eq. (18). With it the adjoint eigenvectors \hat{A} can be calculated by following the same method used in section 6.4. All the adjoint matrices, L_0 , H_{10} , H_{11} , H_2 , H_3 , H_4 , and H_0 , can be found in Appendix F.

6.6 Bi-Orthogonality Fabrication

Since the eigenvectors \hat{A} are available now, the bi-orthogonality between the direct A and adjoint \hat{A} eigenvectors can be defined.

Bi-orthogonality is essentially a kind of dot product. Therefore, the goal is to derive a dot product which equals to zero for the direct A and adjoint \hat{A} eigenvectors, when their wavenumbers α are different. In the first step, the matrix H_0 in the direct system, Eq. (12), should be sorted out into three matrices $H_{\alpha 0}$, $H_{\alpha 1}$, and $H_{\alpha 2}$ characterized by being without α terms, with α terms, and with α^2 terms. Thus:

$$\frac{\partial A}{\partial y} = (H_{\alpha 0} + \alpha H_{\alpha 1} + \alpha^2 H_{\alpha 2}) A \quad (19)$$

Then, multiplying the adjoint eigenvector \hat{A} from the left and integrating from 0 to infinity with respect to y

$$\int_0^{\infty} \hat{A} \frac{\partial A}{\partial y} dy = \int_0^{\infty} (\hat{A} H_{\alpha 0} A + \hat{A} \alpha H_{\alpha 1} A + \hat{A} \alpha^2 H_{\alpha 2} A) dy. \quad (20)$$

And if the spatial wave number of the adjoint mode differs from the direct analog, say α' , Eq. (20) becomes Eq. (21):

$$\int_0^{\infty} \hat{A} \frac{\partial A}{\partial y} dy = \int_0^{\infty} (\hat{A}H_{\alpha 0}A + \hat{A}\alpha'H_{\alpha 1}A + \hat{A}\alpha'^2H_{\alpha 2}A)dy \quad (21)$$

Subtracting Eq. (20) from Eq. (21), those terms without α and α' are cancelled with each other. The terms left are

$$(\alpha' - \alpha) \int_0^{\infty} \hat{A}H_{\alpha 1}A dy + (\alpha'^2 - \alpha^2) \int_0^{\infty} \hat{A}H_{\alpha 2}A dy = 0 \quad (22)$$

Dividing Eq. (22) by $(\alpha' - \alpha)$,

$$\int_0^{\infty} \hat{A}H_{\alpha 1}A dy + (\alpha' + \alpha) \int_0^{\infty} \hat{A}H_{\alpha 2}A dy = 0 \quad (22I)$$

Obviously, if $(\alpha' + \alpha)$ can be made to be removed, then $\int_0^{\infty} \hat{A}(H_{\alpha 1} + H_{\alpha 2})A dy = 0$.

This can be the bi-orthogonality condition, with $H_{\alpha 1} + H_{\alpha 2}$ as a weight function. Unfortunately, it is found that α appears not only at the nominator, but also at denominator in the matrix H_0 (H_0 can be found in Appendix F). Therefore, another way to sort out without α terms, with α terms, and with α^2 terms is needed. The other method to achieve the bi-orthogonality was adopted from Denissen.¹⁵ His bi-orthogonality is

$$i(\alpha - \alpha') \int_0^{\infty} \hat{\mathbf{A}}_{\alpha'} \mathbf{H} \mathbf{A}_{\alpha} dy = \begin{cases} 0, & \text{when } \alpha' \neq \alpha \\ \text{unity}, & \text{when } \alpha' = \alpha \end{cases} \quad (23)$$

where $\hat{\mathbf{A}}_{\alpha'}$ contains four more elements than $\hat{A}_{\alpha'}$ does. Thus, the augmented eigenvectors $\hat{\mathbf{A}}_{\alpha'}$ is $\hat{\mathbf{A}}_{\alpha'} = \left[\hat{u} \frac{\partial \hat{u}}{\partial y} \hat{v} \hat{\pi} \hat{\theta} \frac{\partial \hat{\theta}}{\partial y} \frac{\partial \hat{u}}{\partial x} \frac{\partial \hat{v}}{\partial x} \frac{\partial \hat{\pi}}{\partial x} \frac{\partial \hat{\theta}}{\partial x} \right]^T$. The same situation, the direct eigenvectors \mathbf{A}_{α} has these four more elements than A_{α} does. It is $\mathbf{A}_{\alpha} = \left[u \frac{\partial u}{\partial y} v \pi \theta \frac{\partial \theta}{\partial y} \frac{\partial u}{\partial x} \frac{\partial v}{\partial x} \frac{\partial \pi}{\partial x} \frac{\partial \theta}{\partial x} \right]^T$. Up to this point, the author had found out that the α happened in the denominator is due to the compressible problem and the way that we

are following Fedorov to recast the direct system into ODEs. Notice, the α and its related terms in the denominator in the matrix \mathbf{H} have been removed due to the high Reynolds number in the experiment ($Re = 381470$). In the future, a clever way to avoid the α in the denominator needs to be investigated for compressible problem.

In the beginning of section 6.4, we were planning to project the MVG disturbance from our experiment onto the eigenvectors of Eq. (12), and calculate the coefficients of such projections. By using bi-orthogonality defined at Eq. (23), the coefficients can be efficiently determined. The projections of the MVG disturbance A_0 on the eigenvectors A_j of Eq. (12) is expressed as

$$A_0 = \sum_{j=4} A_j. \quad (24)$$

In other words, the MVG disturbance A_0 can be sum of vorticity eigenvectors ($j = 1$), acoustic eigenvectors ($j = 2$), entropy eigenvectors ($j = 3$), and entropy- acoustic eigenvectors ($j = 4$) along with their branch cuts Γ of eigenvalues α . Since there are six solutions (refer to Eq. (13)) from the linearized Navier-Stokes equations, the summation should be $j = 6$. However, as shown in Figure 39, there is only one vorticity branch, and also one branch of entropy and acoustic are exactly the same so there are only four branches left. The MVG disturbance A_0 can only be expanded by these four eigenvectors.

Now, by applying the bi-orthogonality to Eq. (24), the only term left on the right hand side is the term with the same α . So it results that,

$$\int_0^{\infty} \widehat{\mathbf{A}}_{\alpha} \mathbf{H} \mathbf{A}_0 dy = C \int_0^{\infty} (\widehat{\mathbf{A}}_{\alpha} \mathbf{H} \mathbf{A}_{\alpha}) dy + 0 + 0 + 0. \quad (25)$$

Therefore, the amplitude of the projection C can be calculated as:

$$C = \frac{\langle \hat{\mathbf{A}}_\alpha, \mathbf{H}\mathbf{A}_0 \rangle}{unity}. \quad (26)$$

However, the vector $\hat{\mathbf{A}}_\alpha$ and \mathbf{A}_0 are still in the dimension of 1×10 and 10×1 and matrix \mathbf{H} in 10×10 . The system should be shifted back to \hat{A}_α 1×6 and so. According to Denissen¹⁵, the following equation works

$$C = \frac{\langle \hat{A}_\alpha, \frac{\partial H_0}{\partial \alpha} A_0 \rangle}{unity}. \quad (26i)$$

To calculate the coefficient C in the Eq. (26i), we should input the information of A_0 , $\frac{\partial H_0}{\partial \alpha}$, and \hat{A}_α . The denominator, i.e., *unity*, is set to 1 in the present work. Next, consider the MVG disturbance vector $A_0 = \left[u \frac{\partial u}{\partial y} v \pi \theta \frac{\partial \theta}{\partial y} \right]^T$. The first and third elements u and v are from the PIV experiments: the measured streamwise/wall normal velocity minus the averaged streamwise/wall normal velocity. The operation to the u and v is shown in Figure 43.

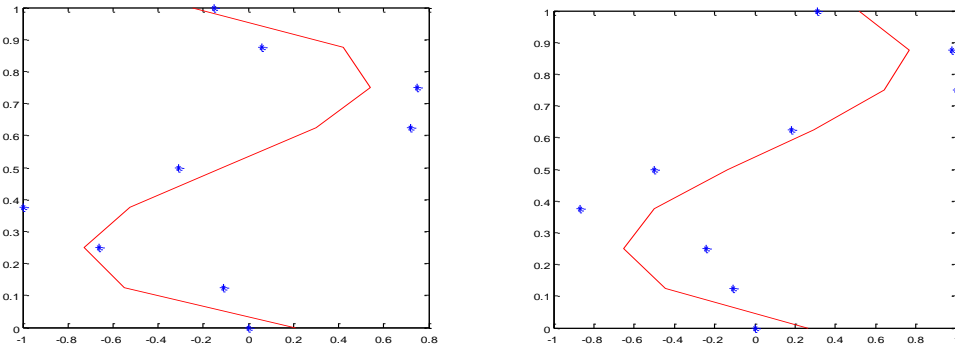


Figure 43 The deviation velocity profile u and v from the boundary layer velocity profile 5 mm down-stream of MVG center line. Each blue star point is averaged from 350 instantaneous images. The red curve is MATLAB **polyfit** with power of 3. Both height and velocity are linearly scaled as $y/\text{boundary-layer thickness}$ and $\text{boundary layer velocity}/\text{free-stream velocity}$.

Then, by Morkovin's strong Reynolds analogy, the element θ can be defined. The pressure perturbation π element is assumed to be 1 in the present work. With all six elements known, the MVG disturbance vector A_0 is determined. The matrix $\frac{\partial H_0}{\partial \alpha}$ in Eq. (26i) is calculated from the direct system of Eq. (12). The final step to calculate the projection coefficients is to find out the adjoint eigenvectors \hat{A} . The following method (shooting method) was used to generate \hat{A} in the present work.

Different than in the free stream, in boundary layer the H_0 matrix in Eq. (18), $\frac{\partial \hat{A}}{\partial y} = -H_0 \hat{A}$, is a function of y . This equation is the standard form of first order linear differential equation $z' + Pz = Q$ with $P = H_0$ and $Q = 0$. To solve such an equation, the Chebyshev polynomials method and shooting method are commonly used. The Chebyshev polynomials method has been used in the section 6.3, so here only the shooting method is described.

Before using the shooting method, the matrix H_0 must be prepared. The terms that cause the H_0 matrix to vary along y in the boundary layer are all the free stream properties U_s , T_s , and μ_s , and their first order derivatives $\frac{\partial U_s}{\partial y}$, $\frac{\partial T_s}{\partial y}$, $\frac{\partial \mu_s}{\partial \theta}$, and $\frac{\partial \mu_s}{\partial y}$. Oppositely, all U_s , T_s , and μ_s equal to 1, and their first order derivatives equal to 0 in the free stream. In section 6.1 (Figure 36), we have already defined the boundary layer velocity profile $U_s(y)$, which is function of y . By using the MATLAB commands **syms** and **diff**, the first order derivative $\frac{\partial U_s}{\partial y}$ can be determined. Then, by Morkovin's strong Reynolds analogy and MATLAB commend **syms** and **diff**, we can define $\frac{\partial T_s}{\partial y}$ from $U_s(y)$. The last two terms $\frac{\partial \mu_s}{\partial \theta}$ and $\frac{\partial \mu_s}{\partial y}$ were defined from Sutherland's formula and also MATLAB commend **syms** and **diff**. These first order y derivative terms can be found in Appendix F. Now

substituting all of them into the H_0 matrix and the shooting method can be started. First of all, it is assumed a solution of the form $\phi_0 e^{-iky}$, where

$$\phi_0 e^{-iky} = \begin{cases} 0 & \text{at wall} \\ e^{-iky} & \text{at the boundary layer - free stream edage} \end{cases} \quad (27)$$

to meet the asymptotic conditions in the free stream. Also, and the boundary conditions are assumed to be $u = v = \pi = \theta = 0$, because of zero perturbations at the wall, and $\frac{\partial u}{\partial y} = \frac{\partial \theta}{\partial y} = 1$, due to the variation could be largest at the wall. With the solution form and the boundary conditions, we can “shoot” the solution.

The shooting method is essentially for initial value problem. Hence, in the present work, the boundary conditions are regarded to be the initial conditions to solve the problem. Moreover, Eq. (18), $\frac{\partial \hat{A}}{\partial y} = -H_0 \hat{A}$, is a first order system, so the Euler’s method was approached the problem. The Euler’s method reads

$$z_{i+1} = z_i + z' \Delta z \quad (28)$$

The initial conditions should be placed in the term z_i , and the assumed solution form inserted in the term z' . The term Δz is the time step: it can be chosen to be dense or thin. The denser the time step, the more accurate the solution can be determined. With the iterations of Eq. (28), z_{i+1} will be piled up and form the solution

$$\hat{A} = \left[u_{i+i} \frac{\partial u}{\partial y_{i+1}} \quad v_{i+i} \quad \pi_{i+i} \quad \theta_{i+i} \quad \frac{\partial \theta}{\partial y_{i+1}} \right].$$

Once the vector \hat{A} , the matrix $\frac{\partial H_0}{\partial \alpha}$, and the vector A_0 , are determined by integrating from wall $y = 0$ up to infinity in the free stream ($y = 10$ in the present work) along y , we can determine the amplitude of the projection C of each mode. The results are shown in the next section.

6.7 Results And Discussion

The first result is in the following, Figure 44. It shows the projection coefficient C of all four eigenvectors (the vorticity, acoustic, entropy, and entropy-acoustic) when wavenumbers are low ($k = 0.2$).

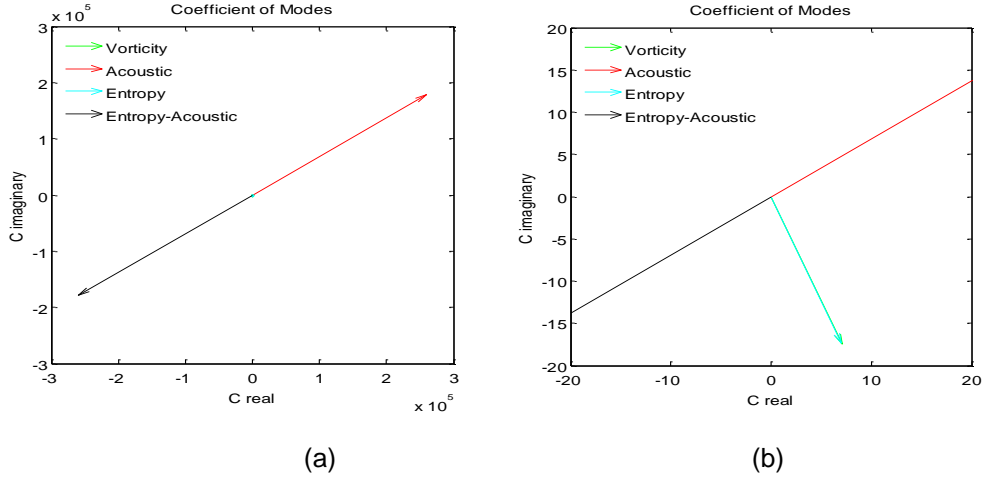


Figure 44 The coefficient C of the vorticity (green), acoustic (red), entropy (cyan), and entropy-acoustic (black) eigenvectors in the complex plane when $k = 0.2$: (a) is 10^3 times zoomed out of (b).

At low wavenumber, the acoustic coefficient is the same magnitude but a phase degree π ahead to the entropy-acoustic coefficient. Therefore, it is possible that the acoustic signal can be observed earlier than the entropy-acoustic signal in experiments. Also, the acoustic signal appears earlier than vorticity and entropy signals almost at $\frac{3}{2}\pi$ and its amplitude is much larger than them. Moreover, if we calculate the percentage numbers of all four coefficients, in this case we have the vorticity coefficient magnitude of $\sqrt{(7.8681)^2 + (-1.9364 \times 10)^2} = 20.9$, acoustic coefficient magnitude of 3.5013×10^4 , entropy coefficient magnitude of 20.76, and entropy-acoustic coefficient magnitude of 3.5014×10^4 , the percentage numbers are almost 0 for the vorticity, almost 0 for the

entropy, however, both 50% for acoustic and entropy-acoustic. This means the energy are all stored in the acoustic and entropy-acoustic modes, and these two modes equally split the energy.

Next, we would like to see how the coefficient and energy storing response to the wavenumber. We selected another four larger wavenumbers ($k = 0.3, 1.7, 5.7,$ and 100) along the branch cuts to be examined. As a reminder, the variable k is used to parameterize the wavenumber α , as mentioned in the section 6.2. For readers' convenience, the plot of branch cuts of the direct system is displayed again here.

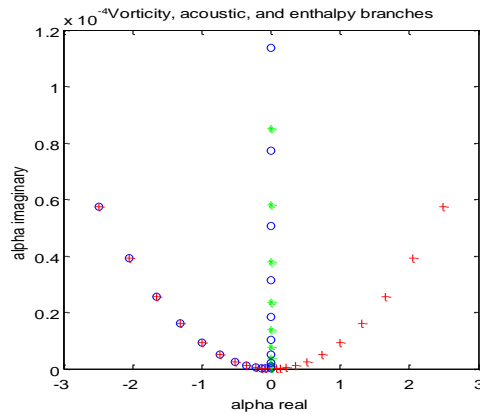
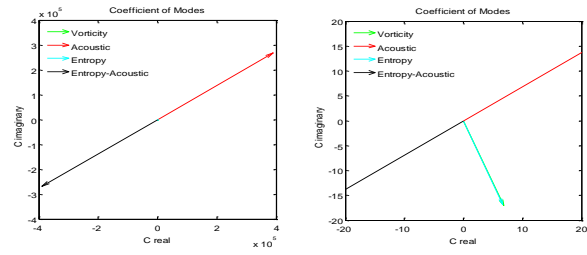


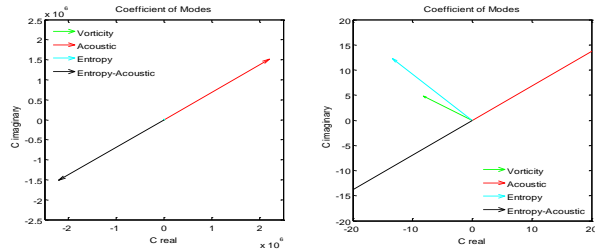
Figure 39 The plot of branch cuts of α in the complex plan: $\text{Re}=381,470$. The vorticity branch (green star) from $\lambda_{1,2}$, the acoustic branches (red cross) from $\lambda_{3,4}$, and the enthalpy branches (blue circle) from $\lambda_{5,6}$. Each branch has unlimited continuous of α but we only plotted ten in this figure.

The coefficients C of all four eigenvectors in four different wavenumbers are plotted at below:



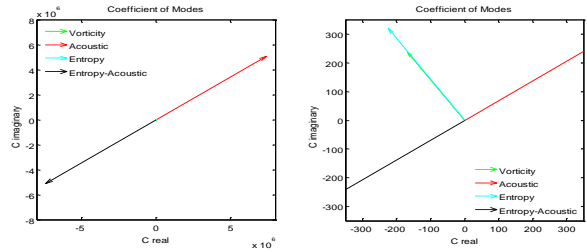
(a)

(b)



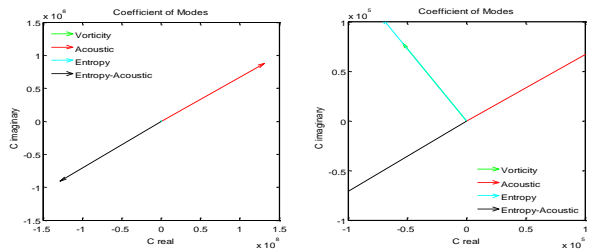
(c)

(d)



(e)

(f)



(g)

(h)

Figure 45 The coefficients C of the vorticity (green), acoustic (red), entropy (cyan), and entropy-acoustic (black) eigenvectors in the complex plane at $k = 0.3, 1.7, 5.7,$ and 100 : (a), (c), (e), and (g) are $10^4, 10^5, 10^4,$ and 10^3 times zoomed out of (b), (d), (f) and (h).

In Figure 45a, c, e, and g, the phase angle and amplitude of the acoustic signal is always ahead and the same as the entropy-acoustic signal. However, as the wavenumber become larger, the entropy-acoustic signal begins to delay more than π to acoustic signal. Physically, this may indicate that the entropy-acoustic signal appears later than the acoustic signal for small scale fluctuations. On the other hand, In Figure 45b, d, f, and h, we can see the amplitude of the voritcity and entropy signals in both cases are much smaller than the acoustic and entropy-acoustic signals. Also, the voritcity and entropy signals change significantly in their phase angle. At low wavenumber, they feature a delay of about $\frac{3}{2}\pi$ from the acoustic signal, but they are running over the entropy-acoustic signal and catching up to the acoustic signal when the wavenumber becomes larger. This may imply that the voritcity and entropy signals appear later than the acoustic and entropy-acoustic signals at large scale. Conversely, their signals appear earlier than the entropy-acoustic signal and running after the acoustic signal at small scale.

Besides, the energy storage (amplitude of the coefficient C) in each mode is of interest. This quantity is tabulated in Table 7.

Table 7 the energy storage in vorticity, acoustic, entropy, and entropy-acoustic modes with varying the parameter k

k	vorticity	acoustic	entropy	entropy-acoustic
0.2	0	0.5	0	0.5
0.3	0	0.5	0	0.5
1.7	0	0.5	0	0.5
5.7	0	0.5001	0	0.4999
100	0	0.5013	0	0.4980

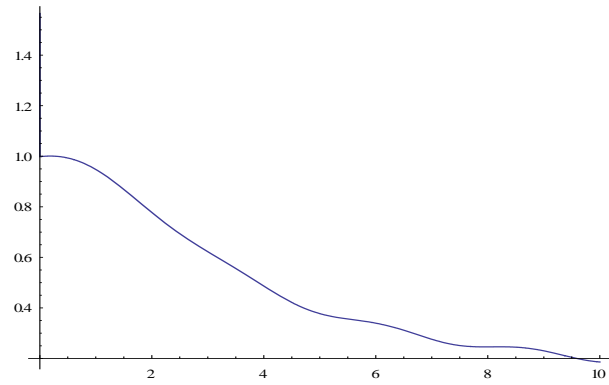
From Table 7, the energy storage in each mode is very stable, almost no change with varying of k . In fact, $k = 100$ is a very large wavenumber. By reviewing Figure 38, from $k = 0.2$ to $k = 1.2$, the fluctuation has been significantly increased, not even $k = 100$. The example $k = 100$ is just to show how stable the energy is stored in each mode, in percentage speaking.

For the second result, the growth of the MVG perturbation downstream of its trailing edge is analyzed by considering the combined evolution of the vorticity, the acoustic, the entropy, and the entropy-acoustic eigenvectors in the boundary layer. Since the coefficient $C(\alpha)$ of each eigenvector has been found, by following the downstream perturbation equation¹⁵ and assume only one wavenumber varying, α , any perturbation can be estimated as:

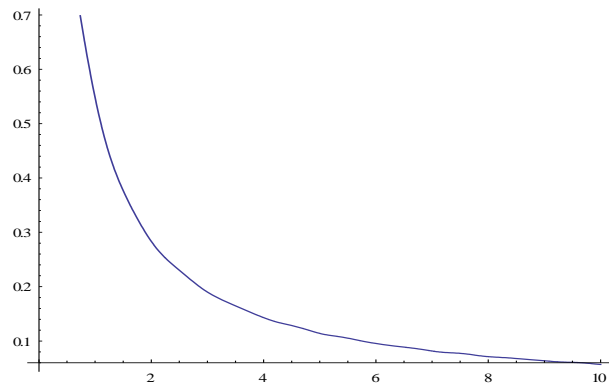
$$\phi = \sum_{\text{branch cuts along the branch cut}} \int C(\alpha)\phi_{\alpha}(y)e^{i\alpha x}d\alpha \quad (29)$$

We checked the height $y=0.125$ in the boundary layer, and integrate the four branches individually along their branch cuts. The results below showed of any perturbation evolution along the MVG downstream:

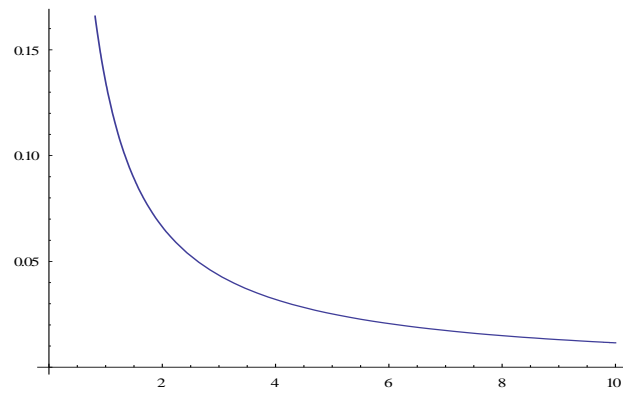
- (1) When Eq. (29) is integrated from $k = 0.2$ to $k = 5.7$ (low wavenumber)
- (2) When Eq. (29) is integrated from $k = 5.7$ to $k = 20$ (medium wavenumber)
- (3) When Eq. (29) is integrated from $k = 20$ to $k = 100$ (high wavenumber)



(a)



(b)



(c)

Figure 46 The MVG perturbation evolution (at $y=0.125$) downstream of the MVG, in the streamwise direction: At (a) low wavenumber, (b) medium wavenumber, and (c) high

wavenumber. The x axis is in the unit of boundary layer thickness. 1 boundary layer thickness is 5 mm. The MVG is at $x=0$.

Two observations arise naturally from Figure 46: first, the decaying nature downstream. The simulation shows all the integration with respect to k decaying downstream, at all scales. Second, the relationship between decaying rate and the scale sizes: the smaller scales (case 3) are found to decay much faster than the large scales (case 1).

Furthermore, when evaluating how all four modes interact to affect the MVG perturbation (see results in Figure 47), two observations can be made. First, the acoustic mode is found to be dominating in amplitude among all modes. The other three modes, the vorticity, entropy, and entropy-acoustic modes have relatively much smaller influence on the MVG perturbation. Second, the amplitudes of all modes were found to be either reducing or staying the same when the perturbation evolves from 5.5 mm to 6 mm downstream of the MVG; oppositely, the MVG amplitude is growing here. The situation is shown in Figure 47a and its amplified view in Figure 47b. Also, the vector compositions (for the situation at 5.5 mm and 6 mm) in the complex plane are shown in Figure 47c and 47d. The MVG amplitude growth is determined by the vector compositions of all these four modes. This analysis explains why it is possible to have the modes (component vectors) reduce their amplitude, but, after vector compositions, the MVG perturbation (composited vector) is growing.

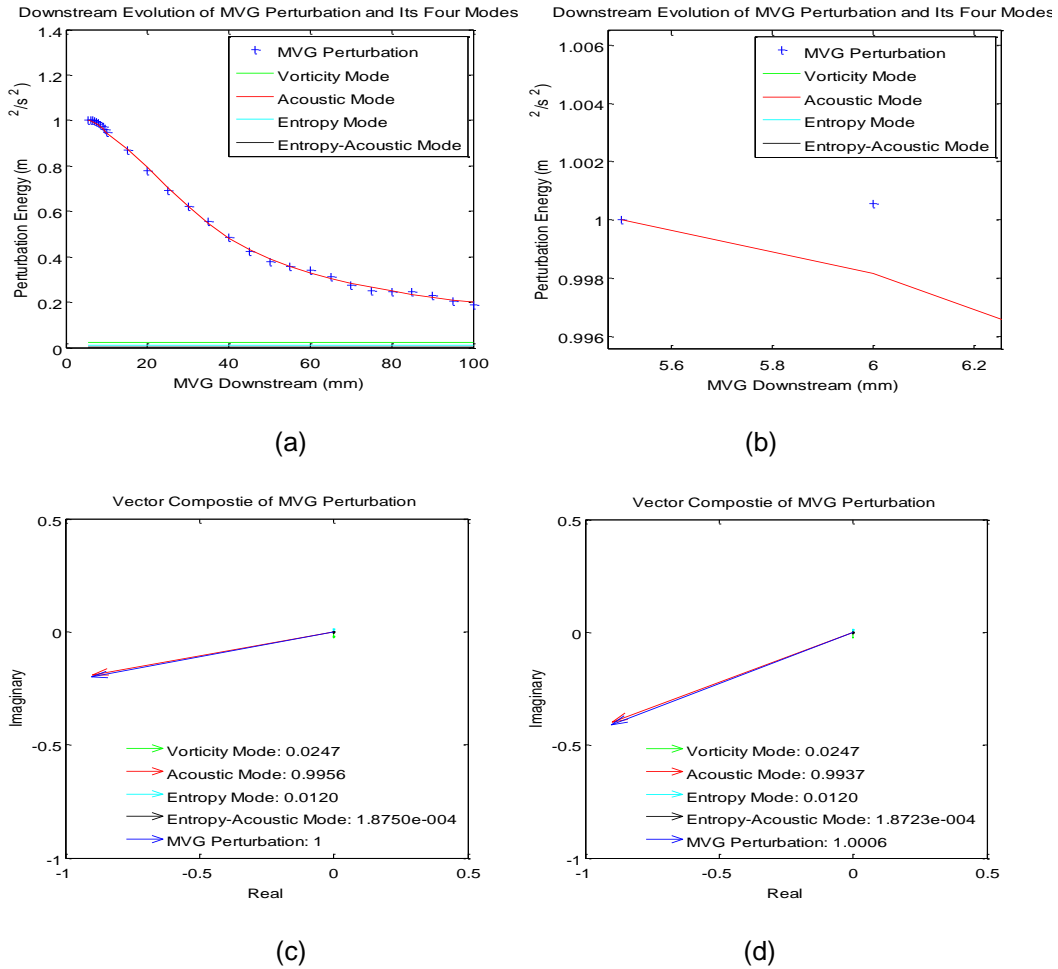


Figure 47 The interaction of vorticity, acoustic, entropy, and entropy-acoustic modes and its outcome in the MVG perturbation: (a) all four modes evolution at the MVG downstream, (b) zoom-in view to show the MVG perturbation is growing from 5.5 mm to 6 mm but the acoustic mode actually decaying in this region, and how the MVG perturbation formed by all four modes in the complex plane at (c) 5.5 mm and (d) 6 mm.

Finally, consider the comparison of the simulation and experiment result. The experimental velocity data from PIV are only available for one spanwise station, that is, 5 mm downstream of the MVG. Those measurements have been used as initial value inputs for the present simulation. The goal is to use the linearized Navier-Stokes

equation and those inputs (the streamwise and wall-normal velocity) to estimate the MVG perturbation at downstream locations. Since the PIV data are not available for further downstream, the pressure data¹⁸ are used for comparison.

The simulation result shows the MVG perturbation in perturbed velocity, hence, it is best to have experimental results in perturbed velocity as well. In order to turn the pressure data into the velocity one, a self-derived strong Reynolds analogy (SRA) has been applied. One of the SRA rule is turning the density data into velocity one, if the pressure fluctuation is constant:

$$\frac{\rho'}{\bar{\rho}} = (\gamma - 1)\bar{M}_{local}^2 \frac{u'}{\bar{u}} \quad (30)$$

If a calorically perfect gas is assumed, substituting the definition of speed of sound $a = \sqrt{\frac{\gamma P}{\rho}}$ into Eq. (30) the following relation is obtained:

$$\frac{P'}{\bar{P}} = (\gamma - 1)\bar{M}_{local}^2 \frac{u'}{\bar{u}} \quad (30i)$$

Eq. (30i) relates the pressure perturbation and velocity perturbation using, as coefficients, the experimentally evaluated mean flow. Now input the local Mach number and mean streamwise velocity (both are experimentally at the flat plate surface so it should satisfy the simulation work at $y=0.125$), the derived experimentally perturbed velocity is shown in Figure 48 below.

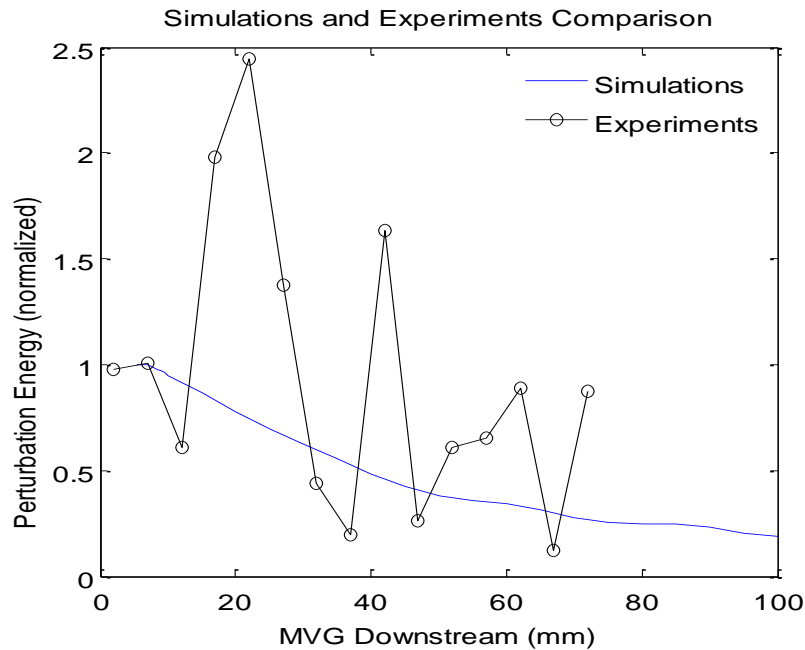


Figure 48 The comparison between the simulation and experiment work of MVG downstream perturbation evolution. The MVG trailing edge is at 0 mm. For simulation work, the data starts at 5 mm. For experimental work, and the pressure sensors are placed first at 2 mm and then every 5 mm downstream until 72 mm, totally 15 sensors. The shock wave and boundary layer interaction area is at 30-50 mm in the present work. The pressure measurements were done only on the flat plate with one MVG, without any shock wave and boundary layer interaction.

In Figure 48, the experimental data seems to have a decaying trend. However, the decay is not as smooth as the simulation analog. In Figure 47b, we have seen a very small perturbation increase at 6 mm, and this is the only increased evolution downstream of MVG in the simulation work. In the experiment, there is a small rise at 6 mm too, and at least two larger rises, at 22 mm and 42 mm, were observed. It is not clear at this point if the experimental growth is affected by measurement error given the large distance between data points.

Chapter 7

Conclusion And Future Work

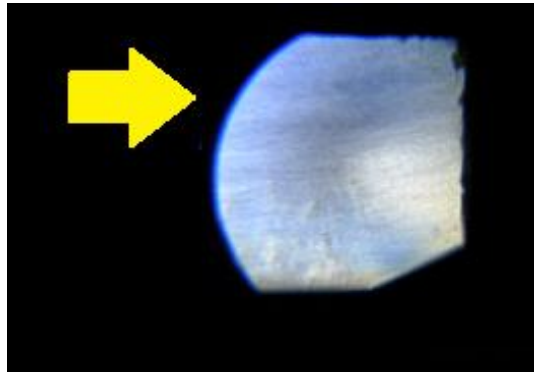
Both experimental and theoretical results yield perturbation decay not far downstream from the MVG: about 72 mm for experiments, and about 95 mm for simulation. The experiments display two distinguishable growths downstream of MVG, while the simulation predicted one small growth at the very beginning. Both works show trends that agree well with each other.

In the present experimental work, there is only PIV data at one station downstream of the MVG. A larger number of PIV stations will allow for a better comparison with experiments in the future. Therefore, the full streamwise, spanwise, and wall-normal properties can be obtained from PIV for to verify and validate the simulations. Experiments were performed also with 20° ramp. In section 4, the detailed turbulent boundary layer profiles were provided every 5 mm upstream of the SBLIs region. It is found that the profiles are distorted when closer to the SBLIs, and also a reverse profile was seen in the SBLIs. If more experiments can be run, more data for averaging can be obtained. Usually, the larger the averaging sample, the more precise trend is achieved. Also, along with considering only MVG or only ramp, the MVG combined ramp will be investigated in future analyses. Note that this was already done in surface flow visualization (section 5), but not yet using PIV. In section 5, the results and discussion about MVG combined ramp has shown how the MVG downstream vortices affect the shock wave and boundary layer interaction, in a statistical way. If the PIV work can be done with the MVG combined ramp case, it will be very interesting to see how the vortices interact with the separation bubble, in detail. Meanwhile, the data can be input to the linearized Navier-Stokes equations for simulation work.

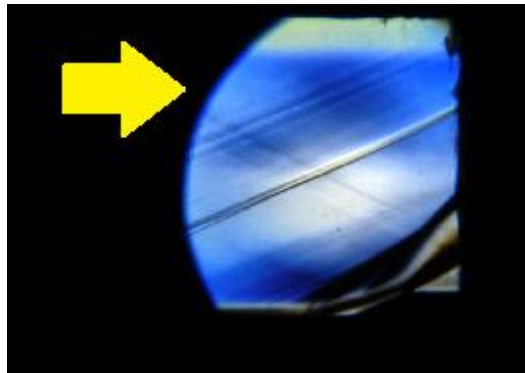
For simulation work, we plan to extend the direct system to three-dimensions. The spanwise wavenumber was assumed constant in this paper. In the future for three-dimensional simulations, the evolution of MVG downstream perturbation will be affected by spanwise wavenumber as well. Also, the physics of the adjoint system will be investigated in the future. The adjoint was only used as a mathematical tool to derive a bi-orthogonal projection in the present research. Notice that the use of the bi-orthogonality relationship in the compressible regime required a clever trick to eliminate the streamwise wavenumber from the denominator. The proposed approach assumes that the streamwise wavenumber can be neglected in the denominator, since the other term has a large Reynolds number (381470) factor as determined from the experimental work. Future research will focus on other ways to fabricate the bi-orthogonality without neglecting the streamwise wavenumber in the denominator of the residual function of the shooting method.

Finally, the study of separated ramp-induced shock wave boundary layer interaction with upstream MVG at Mach 2.5 is an interesting research topic. It will be beneficial in the future if the experimental and simulation work can be compared, for all cases: MVG alone, ramp, and MVG combined ramp. A comprehensive study along these lines can be very practical and also academic at the same time.

Appendix A
The Schlieren Optics Result



(a)



(b)

The Schlieren optics result of oblique shock wave generators during the test: (a) unstart, and (b) start.

Appendix B

MATLAB Program for Image Processing (PIV part)

I The code fragment of defining the flat plate surface.

```
[B]=imread('directory'); % Set B as the matrix
gry=rgb2gray(B); % Turn RGB scale to the gray scale
gry1=imadjust(gry,[5/255 170/255],[0 1]); % The contrast enhancement
h=[ -1 -2 -1; 0 0 0; 1 2 1 ]; % The Sobel operator
A=filter2(h,gry1); % Setup edge detection
A(797:886,:)=0;%Remove the bottom margin
imshow(A); % Show the image
impixelinfo % Show the pixel information
%following code was looking for the first non-zero pixel in all 741 column
for i=2:741;%i=1 is the black side line>>remove
eval(['A' num2str(i) '=find(A(end:-1:1,i)>0,1)']);%A(clonum,row)
end
b=[A2:A741]; % y axis. Note that b=[A2 A3 ... A741]
x=2:741; % x axis
plot(x,b)
```

II The code fragment of boundary layer velocity profiles stitching.

```
c=zeros(57,741); %this is for the storage of velocity vectors from 57 images
%%%%%%%%%% this part is the extend code from the part in Figure 10
%%%%%%%%%%
for k=20:76; [B]=imread(['directory\Window_B000',num2str(k),'.bmp']);
gry=rgb2gray(B);
gry1=imadjust(gry,[5/255 170/255],[0 1]);
h=[ -1 -2 -1; 0 0 0; 1 2 1 ];
A=filter2(h,gry1);
A(780:886,:)=0;%Remove the bottom margin
    for i=1:741;%(i=1 is the black side line>>remove):Not in this case
        eval(['A' num2str(i) '=find(A(end:-1:1,i)>0,1)']);%A(clonum,row)
    end
b=[A1 A2...A741]; %plot(x,b);%This cause the image up side down and right side
left
b1=-((b-770)*(-24.5-(-16)))/(29-770)+24.5);% turn pixel to mm. it makes up side
down back to normal
x=1:741;
x1=-((707-x)*(-19-(-11)))/(707-7)+19);%turn pixel to mm. it makes right side left
```

```

back to normal
j=k-19;
c(j,:)=b;
plot(x1,b1)
hold on
end
%%%%%%%%%%%%%%%%%%%%%%%%%%%%%%%%%%%%%%%%%%%%%%%%%%%%%%%%%%%%%%%%%%%%%%%%
vary=c(:,363); %seeking the y variations @x=-15.1429mm(x=363pixel, check this
everytime because x might be changed due to how you export data from
DaVis);This can aslo check which surfaces are way too low
vary(find(vary<300))=[]; %reject the exposure pictures and far away surface
locations out @x=-15.1429mm
M=mean(vary);
diff=vary-M;
diffinmm=0.5*diff/44;
diffinmm_fit_to_index_j=[-0.2254 -0.1345 -0.1345 -0.1799 -0.0436 0.3201
0.5473 -0.1799 0 0.0928 0.0473 0 -0.1799 -0.1345 -0.1345 0.0928 -0.1345 -
0.1345 0.0473 0.0019 -0.1345 0.0019 -0.0436 -0.1799 -0.2254 0.2292 -0.1345 -
0.2254 -0.1799 0.0473 -0.0436 -0.2254 -0.2254 -0.089 0.2746 0 -0.1799 0.1837 -
0.089 0.0928 0 -0.3617 0 0 0.0019 0.1383 0.1383 0 0.3655 0.0928 -0.1799 0 0 -
0.089 0.0473 0.5928 0.8655]; % The stitching reference for each fluctuation (unit
in mm)
%imported from the txt
B=zeros(21228,57);
C=zeros(21228,57);
S=zeros(1,57);
for
k=[20,21,22,23,24,25,26,27,29,30,32,33,34,35,36,37,38,39,40,41,42,43,44,45,46,
47,48,49,50,51,52,53,54,56,57,58,59,61,64,65,66,68,69,70,73,74,75,76];
[E]=load(['directory\B000',num2str(k),'.txt']);
j=k-19;
j(find(j<0))=[];
B(:,j)=E(:,2);
C(:,j)=E(:,3);
    for i=1:115
        y(i)=B(i*183+74,j)+diffinmm_fit_to_index_j(j);%@x=-15.1429mm(after
stitching)
        BLV(i)=C(i*183+74,j);%@x=-15.1429mm
    end
end

```

```
plot(BLV,y,'*')  
S(1,j)=C(18923,j); %extract velocity @y=-20.5726 from #25-#44  
hold on  
end
```

Appendix C

MATLAB Program for Image Processing (SFV part)

I The commands which upload a image and show the image information

```
[B]=imread('directory');% Set B as the matrix
imshow(B);% Show the image
impixelinfo % Show the pixel information
```

II The demonstration in the code fragment for gray scaling, contrast enhancement, and Sobel edge detection

```
[B]=imread('directory');% Set B as the matrix
gry=rgb2gray(B);% Turn RGB scale to the gray scale
gry1=imadjust(gry,[75/255 170/255],[0 1]);% The contrast enhancement
h=[ -1 -2 -1; 0 0 0; 1 2 1 ];% The Sobel operator
A=filter2(h,gry1);% Setup edge detection
```

III The demonstration in the code fragment

```
% Look for the first non-zero pixel in row 74 to 471
for i=74:471
eval(['A' num2str(i) '=find(A(i,:),1)']);
end
b=A471:A74; % x axis. Note that b=[A471 A470 ... A74]
y=74:471;% y axis
plot(b,y) % plot
```

IV The code of a straight line

```
b=578;% The x axis
y=74:471;% The y axis
plot(b,y)% Plot
```

V The code of straight line with zigzag.

```
A=rand(398,1);% Apply the random flctuations
y=74:471;% The y axis
```

```
B=2*A+578;% Amplify and shift the random fluctuations to around the location of "exp  
lines"  
plot(B,y)% Plot the straight line with zigzag
```

VI The code of a chainsaw line

```
z=[515 579 515 579 515 579 ... 515 579];% The x axis. Two numbers 515 and 579 take  
turns added to z until z has 398 digit numbers  
y=74:471;% The y axis  
plot(z,y)% Plot the chainsaw line
```

VII The code fragment for defining the zigzag index which is sensitive to the small
fluctuates.

```
for j=1:150;% Repeat the loop 150 times (350-200=150)  
Q(j)=abs(B(j+1)-B(j));% The pixels (fluctuates) difference between the neighbor  
elements of the line.  
end;U=sum(Q)% Sum of all fluctuates
```

VIII The code fragment for defining the zigzag index which is sensitive to the large
fluctuates

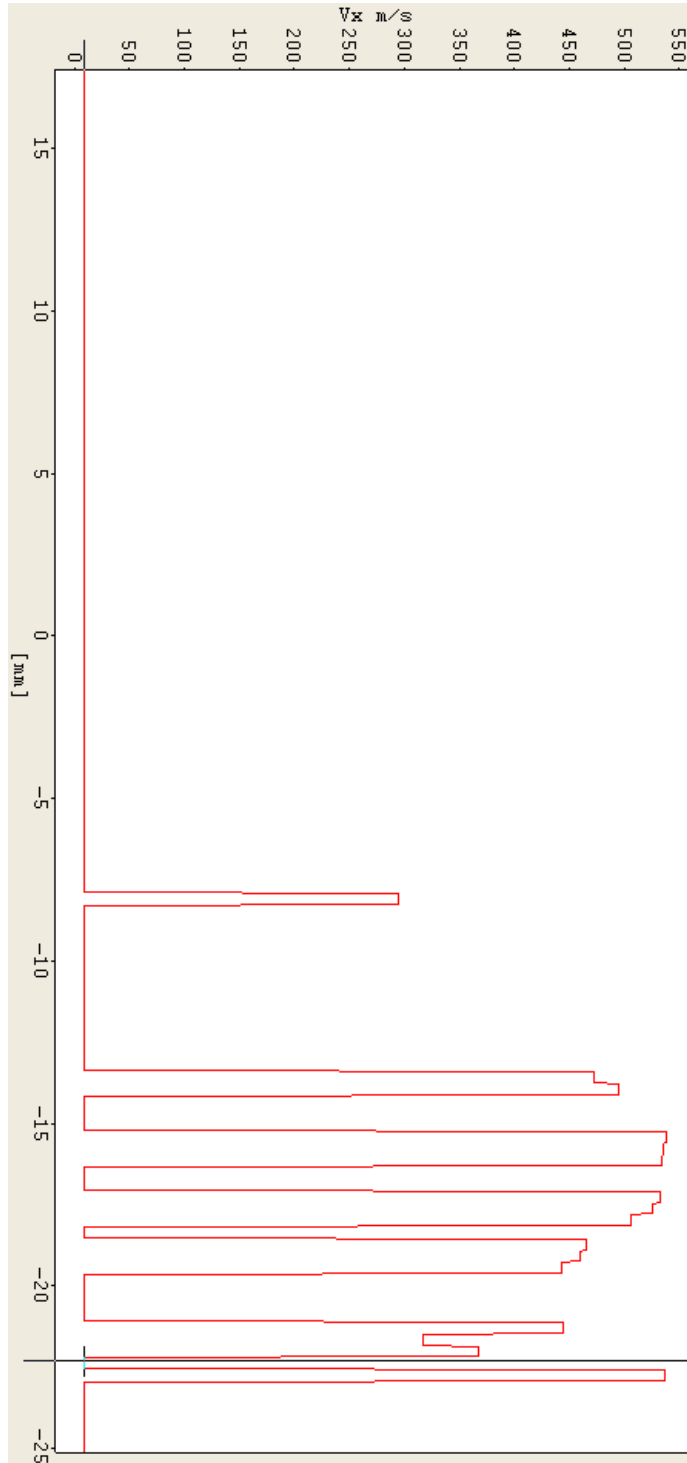
```
for j=1:391;% Repeat the loop 391 times (Caution: Not 398.)  
Q(j)=abs(B(j+7)-B(j));% The pixels (fluctuates) difference between every other 7  
neighbor elements of the line.  
end;U=sum(Q);% Sum of all fluctuates
```

Appendix D

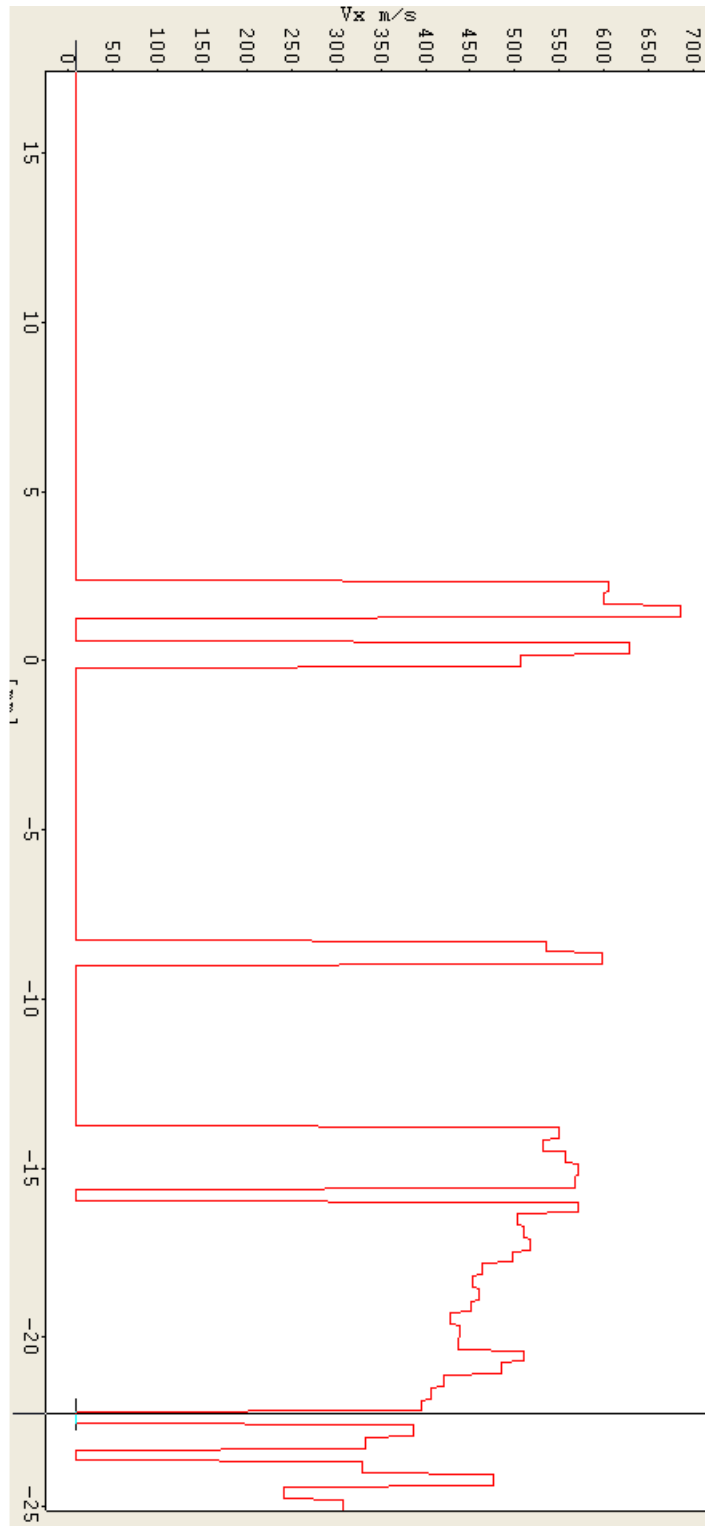
Boundary Layer Velocity Profile from PIV

I. The boundary layer velocity profile on the flat plate (flow is from left to right)

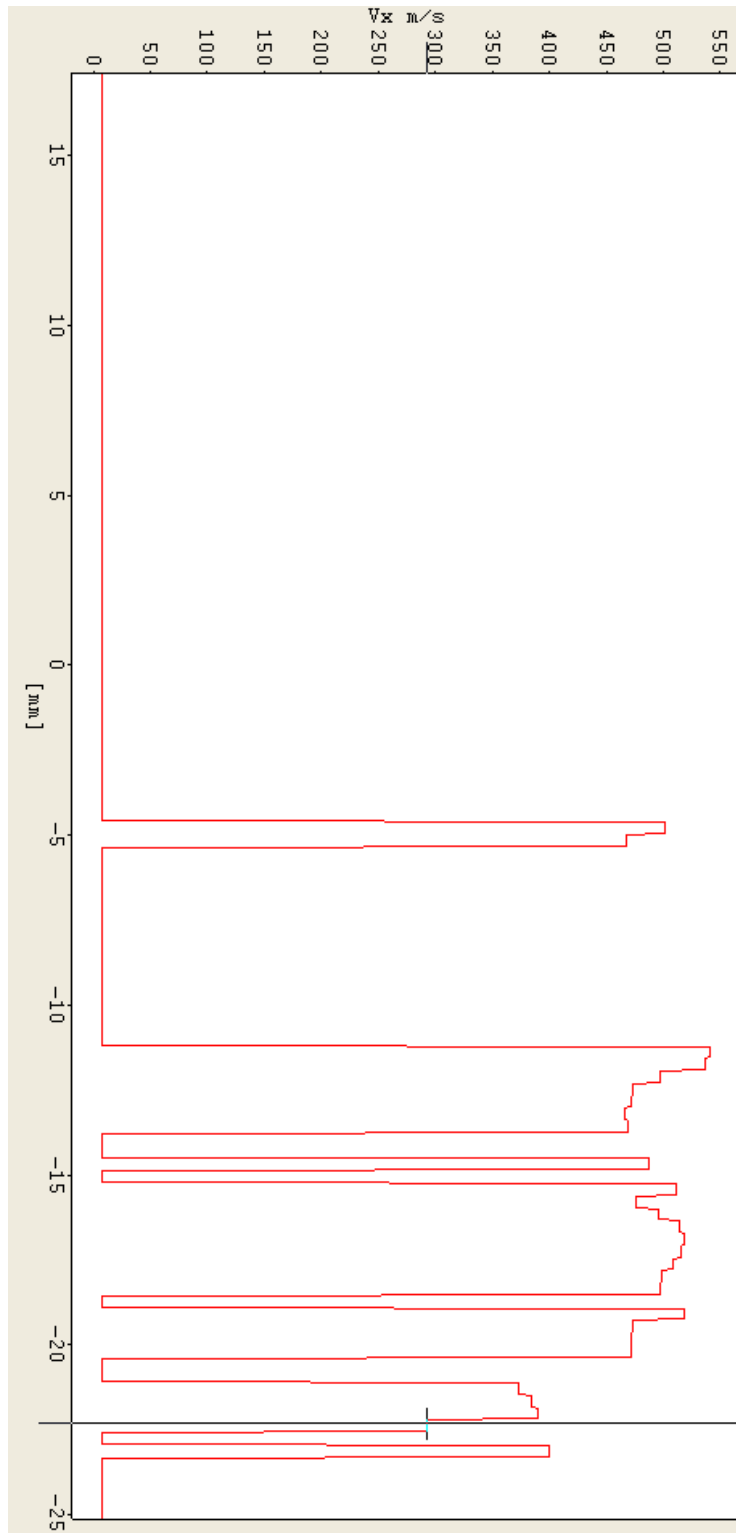
(a) A randomly chosen instantaneous image.



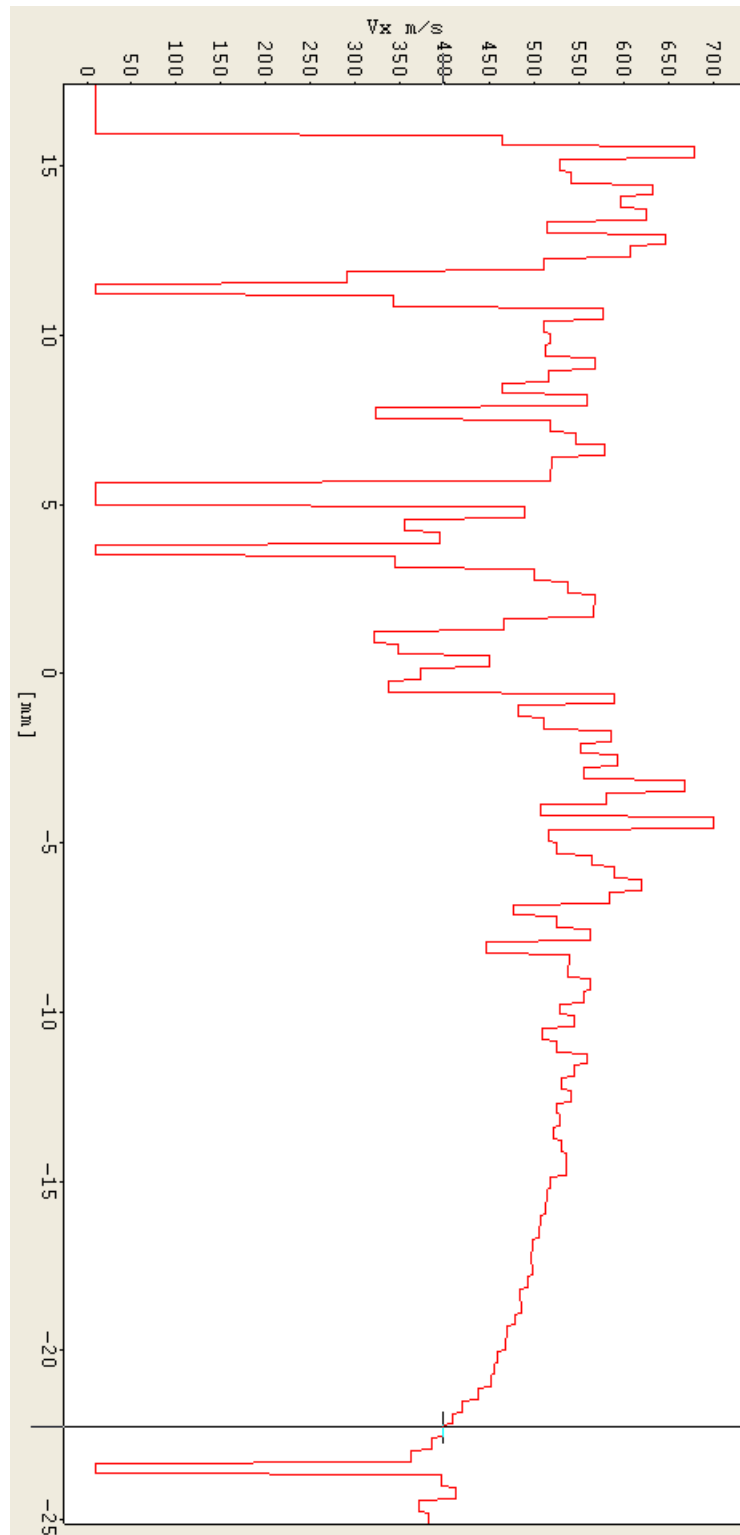
(b) Another instantaneous image after 0.2 seconds.



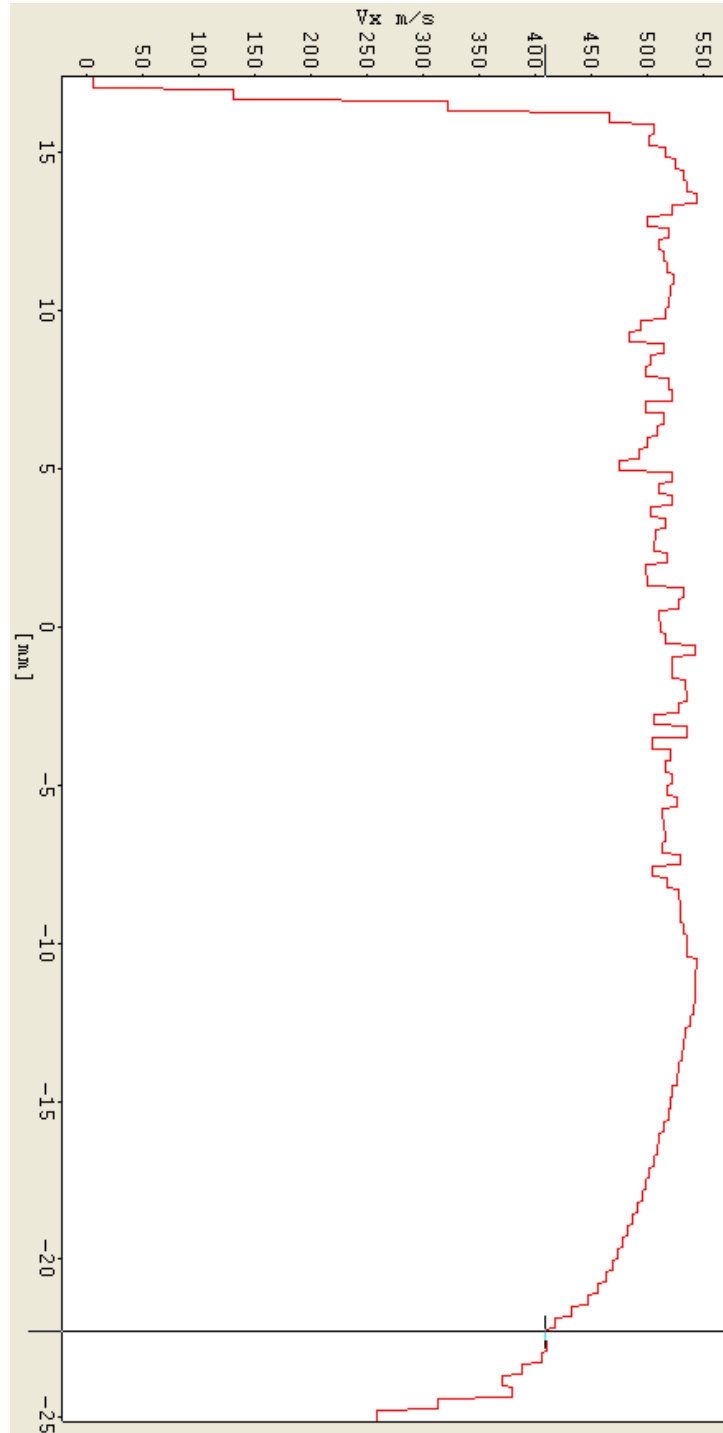
(c) Another instantaneous image after 0.4 seconds.



(d) The image after time averaging of 75 images. Each of the images was 0.2 seconds apart.

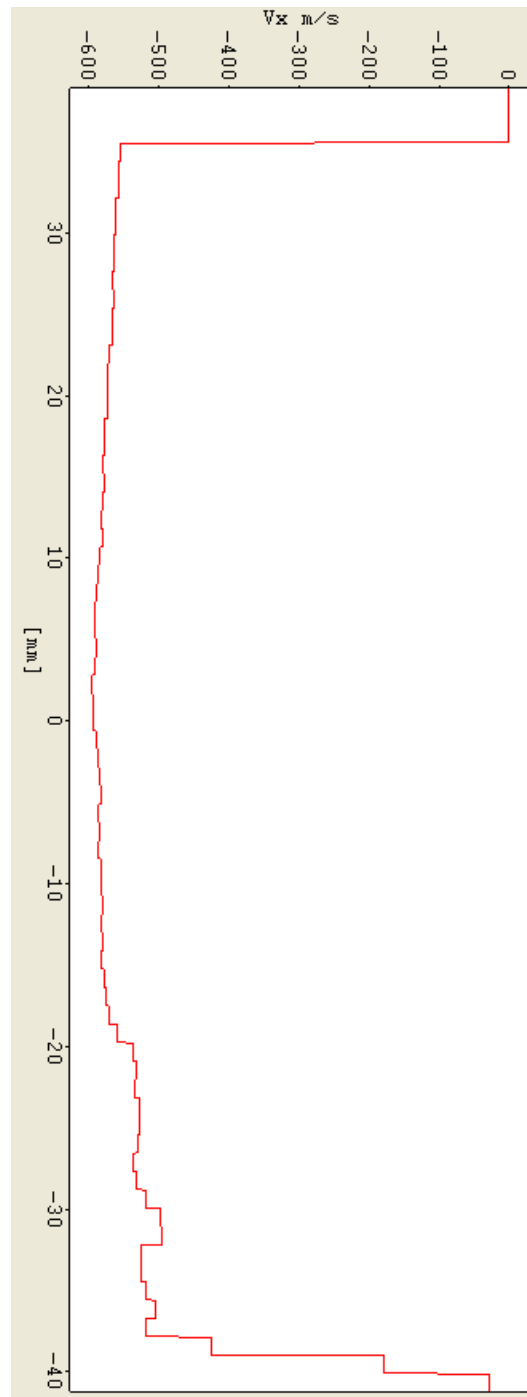


(e) The image after time averaging of 75 images and space averaging of a certain area of flow field.

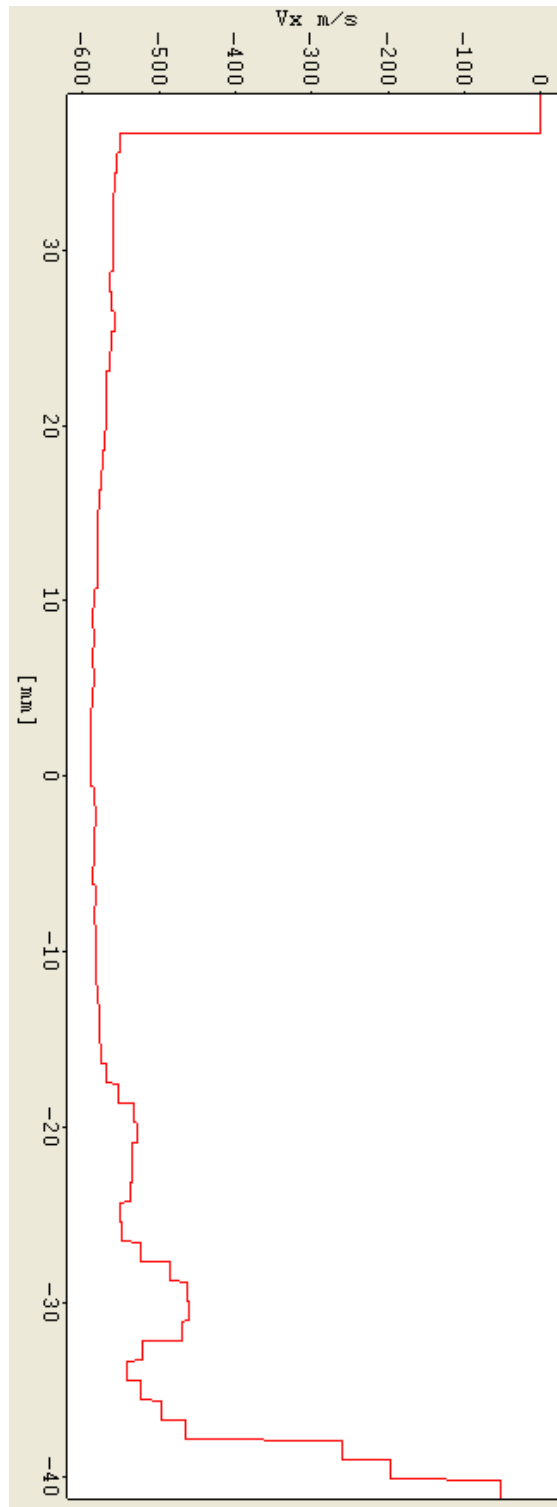


II The boundary layer velocity profile on the 20° ramp (439 images averaged, and flow is from right to left).

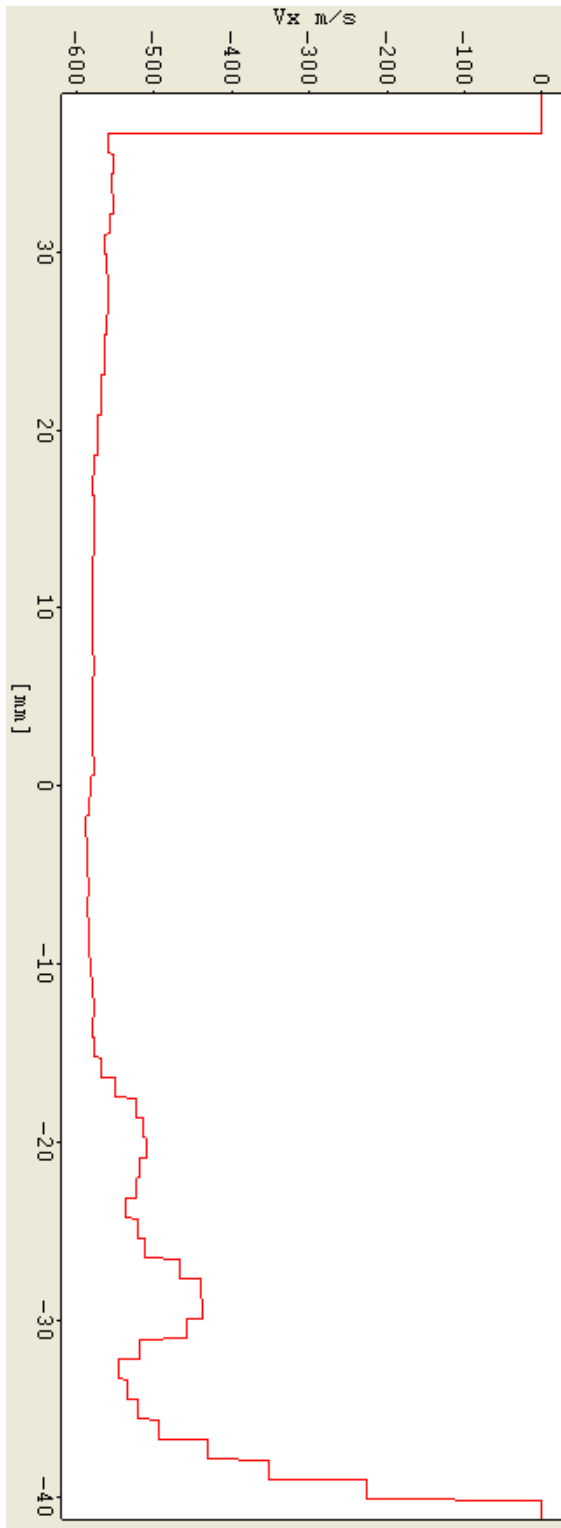
(a) 50 mm upstream of the ramp corner



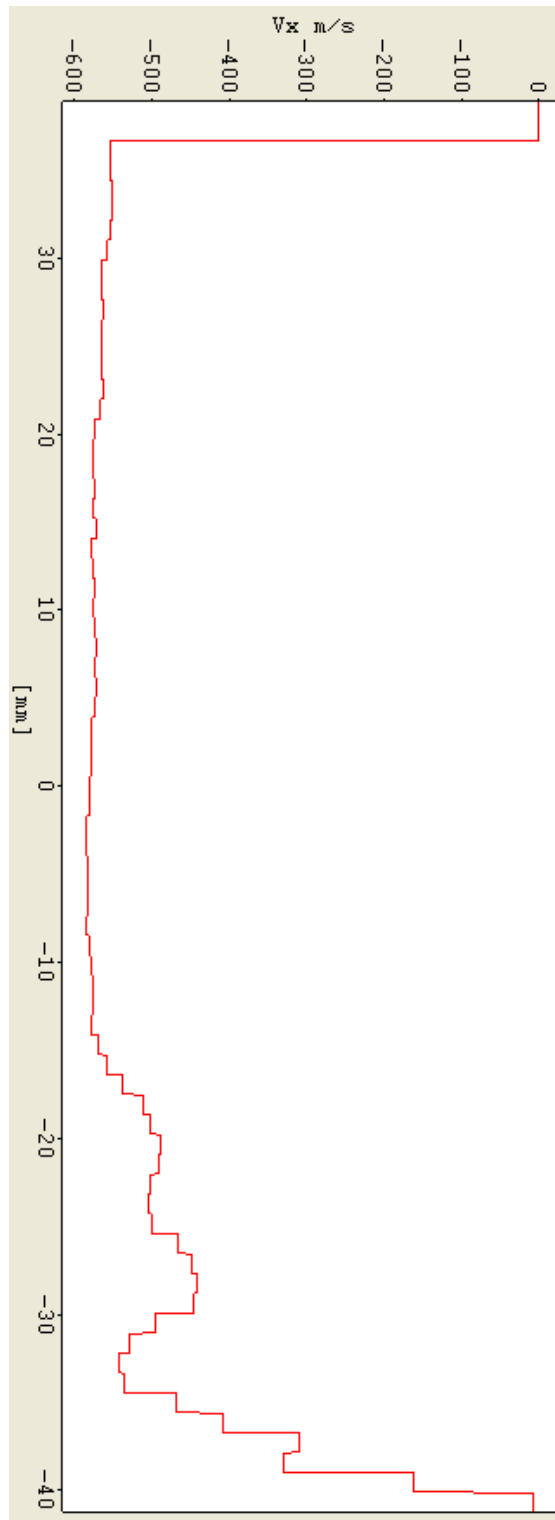
(a) 45 mm upstream of the ramp corner



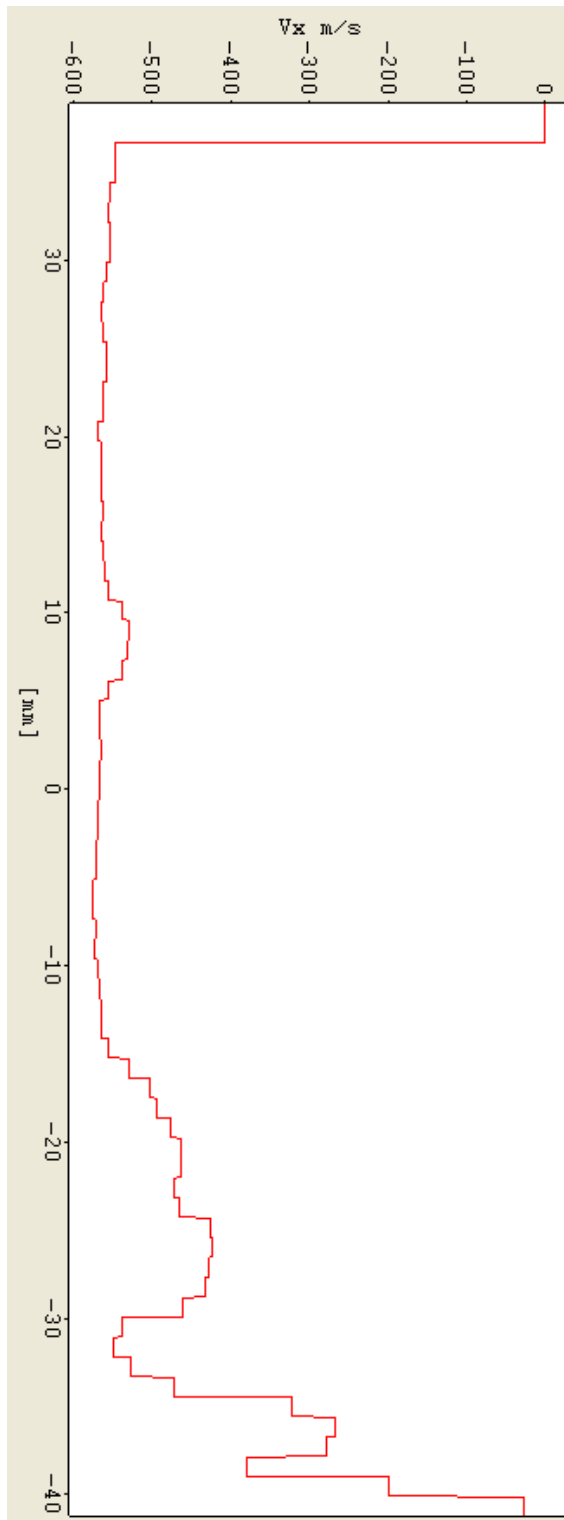
(c) 40 mm upstream of the ramp corner



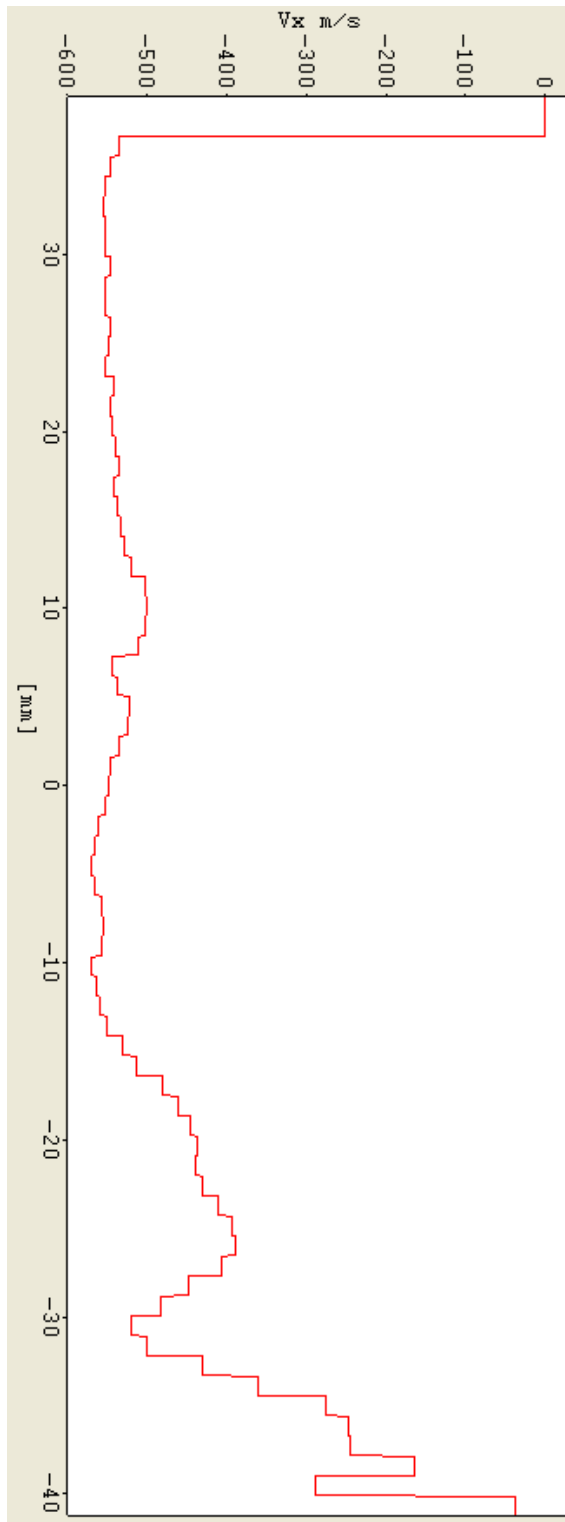
(d) 35 mm upstream of the ramp corner



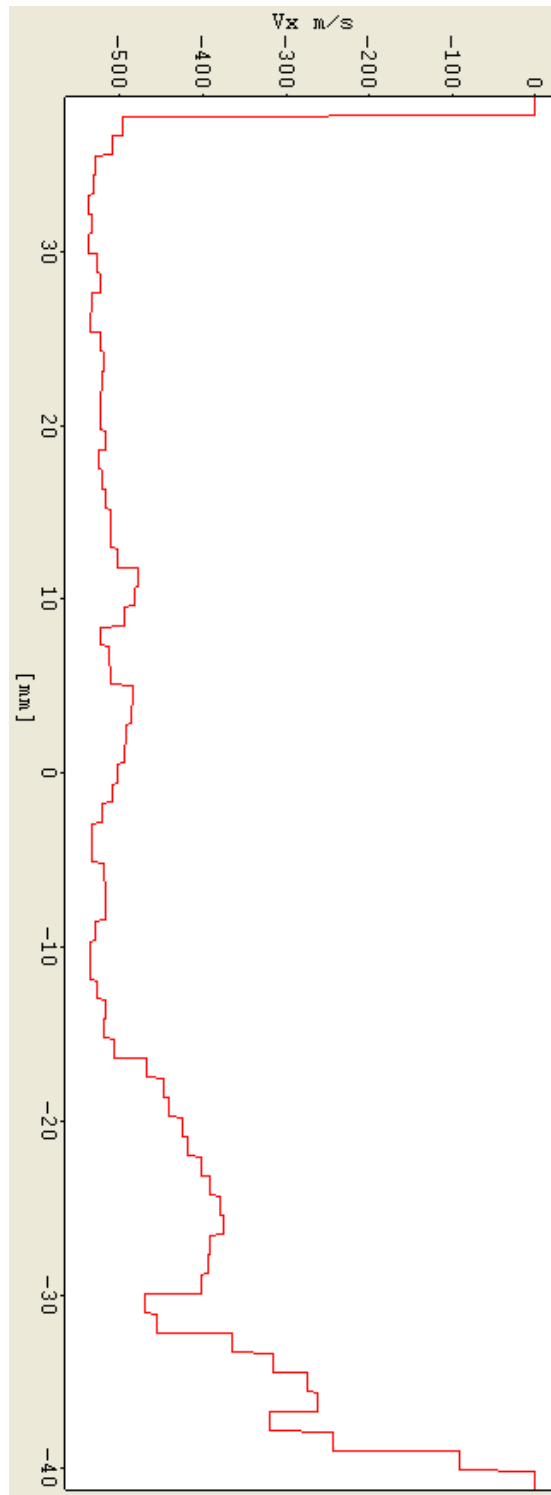
(e) 30 mm upstream of the ramp corner



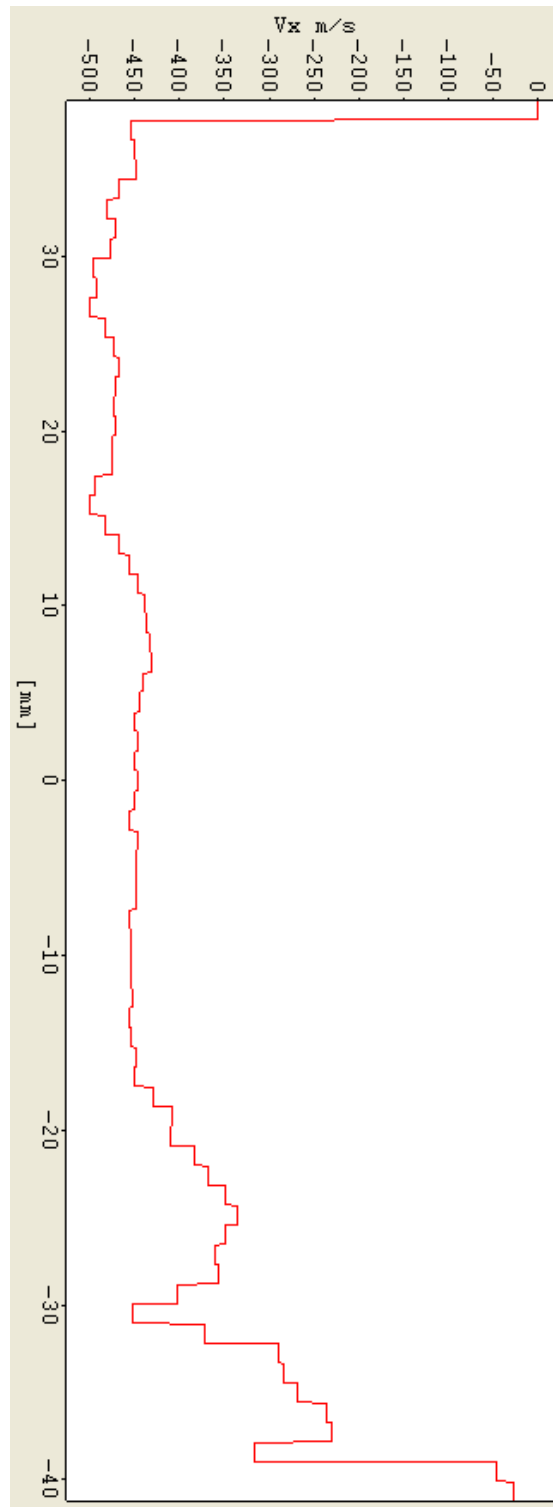
(f) 25 mm upstream of the ramp corner



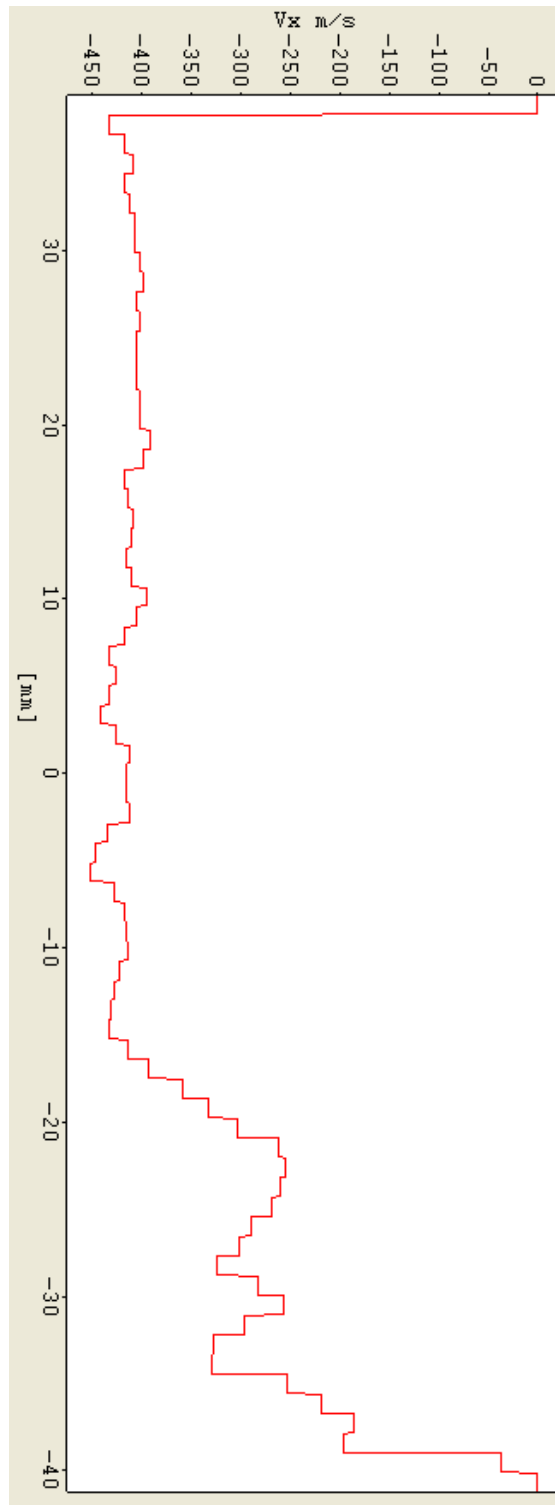
(g) 20 mm upstream of the ramp corner



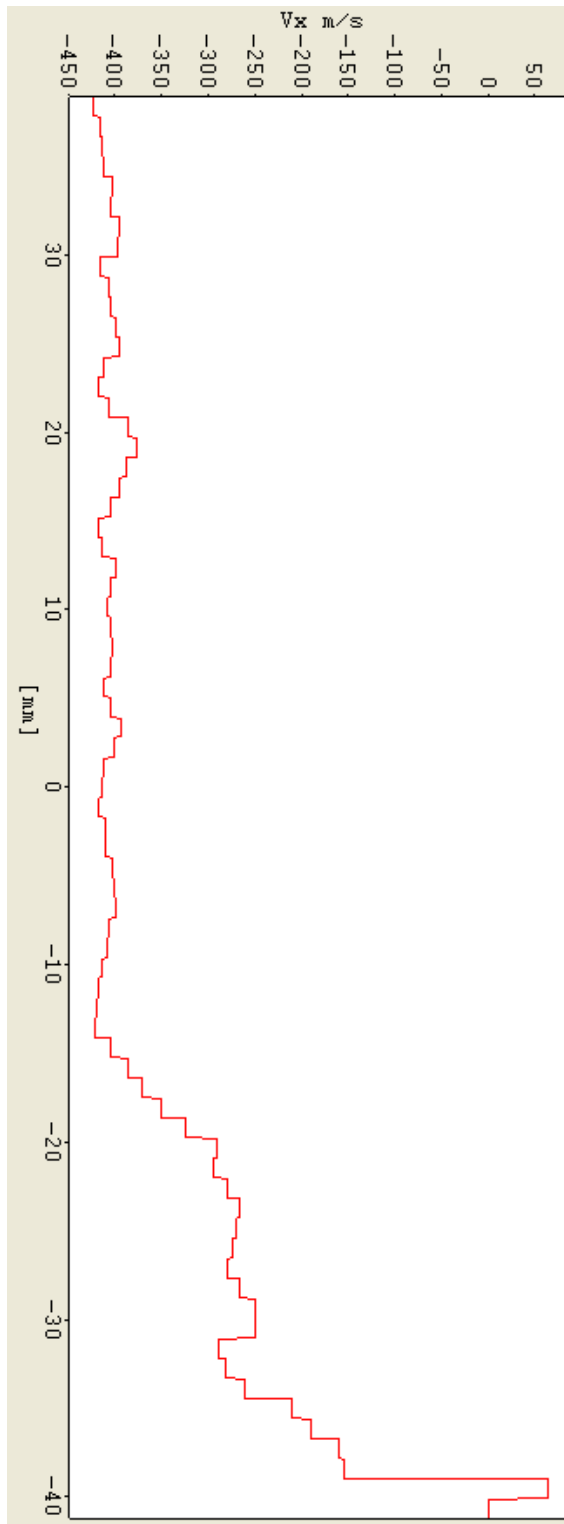
(h) 15 mm upstream of the ramp corner



(i) 10 mm upstream of the ramp corner

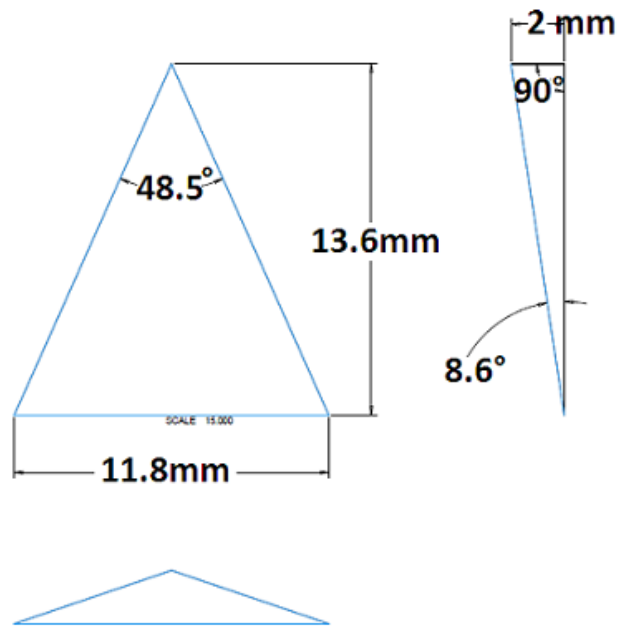


(j) 5 mm upstream of the ramp corner

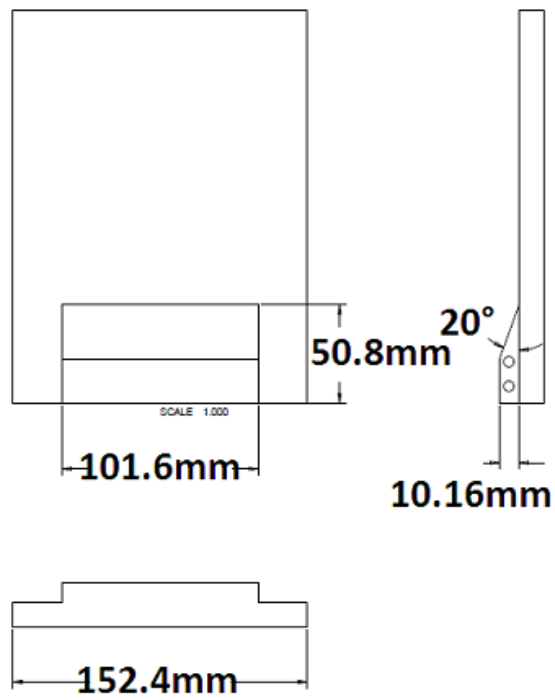


Appendix E
Pro-E drawings

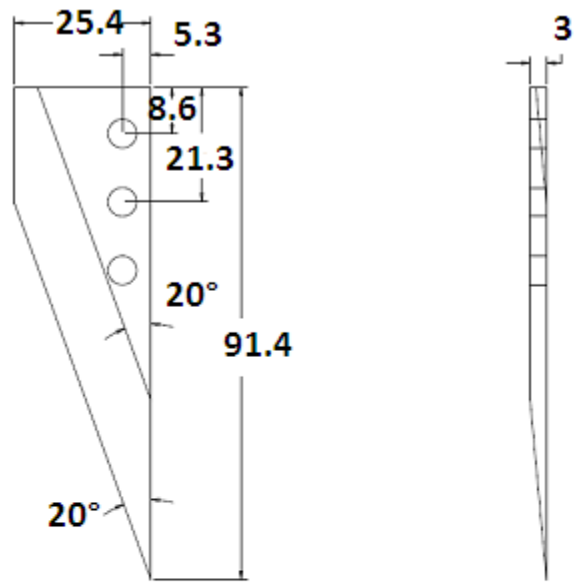
I The engineering drawing of the MVG



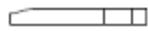
II The engineering drawing of 20° ramp



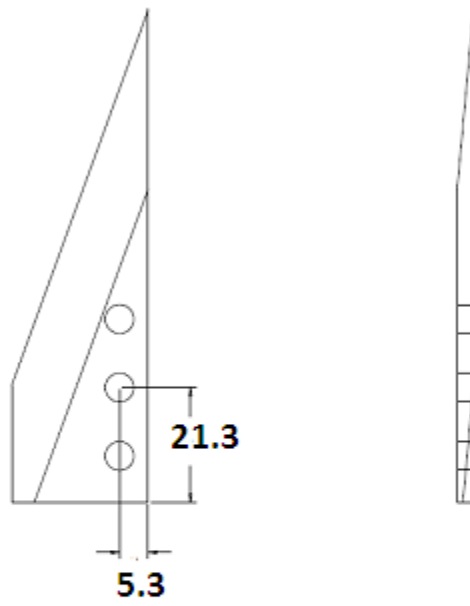
III The engineering drawing of long fence pair



ϕ 1/4-28



Unit: mm



**All other dimensions
reference to "fence
long." Unit in mm.**

Appendix F

Matrices and Terms of the Linearized Navier-Stokes Direct and Adjoint Equations

I Related matrices in section 6.2 (the direct eigenfunctions)

$$\chi = \frac{1}{\frac{Re}{\mu_s} + i\gamma M^2(\alpha U_s - i\omega)}$$

$$L_0 = \begin{bmatrix} 0 & 0 & 0 & 0 & 0 & 0 \\ 0 & 0 & 0 & 0 & 0 & 0 \\ 0 & 0 & 0 & 0 & 0 & 0 \\ 0 & 0 & -r \frac{\mu_s}{Re} & 0 & 0 & 0 \\ 0 & 0 & 0 & 0 & 0 & 0 \\ 0 & 0 & 0 & 0 & 0 & 0 \end{bmatrix}$$

$$H_{10} = \begin{bmatrix} 0 & 0 & 0 & 0 & 0 & 0 \\ \frac{Re}{\mu_s} \rho_s & 0 & 0 & 0 & 0 & 0 \\ 0 & 0 & 0 & -\frac{1}{P_s} & -\frac{1}{T_s} & 0 \\ 0 & 0 & -\rho_s & 0 & 0 & 0 \\ 0 & 0 & 0 & 0 & 0 & 0 \\ 0 & 0 & 0 & -\frac{RePr}{\mu_s}(\gamma - 1)M^2 & \frac{PrRe}{\mu_s} \rho_s & 0 \end{bmatrix}$$

H_{11}

$$= \begin{bmatrix} 0 & 0 & 0 & 0 & 0 & 0 \\ 0 & -\frac{1}{\mu_s} \frac{\partial \mu_s}{\partial y} & \frac{Re \rho_s}{\mu_s} \frac{\partial U_s}{\partial y} & 0 & -\frac{1}{\mu_s} \mu'_s \frac{\partial^2 U_s}{\partial y^2} & -\frac{1}{\mu_s} \mu'_s \frac{\partial U_s}{\partial y} \\ 0 & 0 & -\frac{1}{\rho_s} \frac{\partial \rho_s}{\partial y} & 0 & 0 & 0 \\ 0 & 0 & 0 & 0 & \frac{\mu_s}{Re} \mu'_s \frac{\partial^2 U_s}{\partial x \partial y} & 0 \\ 0 & 0 & 0 & 0 & 0 & 0 \\ 0 & -Pr(\gamma - 1)M^2 \frac{\partial U_s}{\partial y} & \frac{PrRe \rho_s}{\mu_s} \frac{\partial T_s}{\partial y} & 0 & -\mu'_s \left(\frac{\partial U_s}{\partial y} \right)^2 \frac{Pr}{\mu_s} (\gamma - 1)M^2 - \frac{1}{\mu_s} \mu'_s \frac{\partial^2 T_s}{\partial y^2} & -\frac{1}{\mu_s} \mu'_s \frac{\partial T_s}{\partial y} \end{bmatrix}$$

$$H_2 = \begin{bmatrix} 0 & 0 & 0 & 0 & 0 & 0 \\ \frac{Re}{\mu_s} \rho_s U_s & 0 & -\frac{1}{\mu_s} \frac{\partial \mu_s}{\partial y} & \frac{Re}{\mu_s} & 0 & 0 \\ -1 & 0 & 0 & -\frac{U_s}{P_s} & \frac{U_s}{T_s} & 0 \\ 0 & 0 & -\rho_s U_s & 0 & \frac{\mu_s}{Re} \mu_s' \frac{\partial U_s}{\partial y} & 0 \\ 0 & 0 & 0 & 0 & 0 & 0 \\ 0 & 0 & -2Pr \frac{\partial U_s}{\partial y} (\gamma - 1) M^2 & -\frac{PrRe}{\mu_s} (\gamma - 1) M^2 U_s & \frac{PrRe \rho_s}{\mu_s} U_s & 0 \end{bmatrix}$$

$$H_3 = \begin{bmatrix} 0 & 0 & 0 & 0 & 0 & 0 \\ 0 & 0 & -(m+1) & 0 & 0 & 0 \\ 0 & 0 & 0 & 0 & 0 & 0 \\ (m+1) \frac{\mu_s}{Re} & 0 & 0 & 0 & 0 & 0 \\ 0 & 0 & 0 & 0 & 0 & 0 \\ 0 & 0 & 0 & 0 & 0 & 0 \end{bmatrix}$$

$$H_4 = \begin{bmatrix} 0 & 0 & 0 & 0 & 0 & 0 \\ -r & 0 & 0 & 0 & 0 & 0 \\ 0 & 0 & 0 & 0 & 0 & 0 \\ 0 & \frac{\mu_s}{Re} & 0 & 0 & 0 & 0 \\ 0 & 0 & 0 & 0 & 0 & 0 \\ 0 & 0 & 0 & 0 & -1 & 0 \end{bmatrix}$$

II Related matrices in section 6.5 (the adjoint eigenfunctions)

$$\chi = 1 - i\alpha \frac{rU_s\mu_s}{P_s Re}$$

$$L_0 = \begin{bmatrix} 0 & 0 & 0 & 0 & 0 & 0 \\ 0 & 0 & 0 & 0 & 0 & 0 \\ 0 & 0 & 0 & 0 & 0 & 0 \\ 0 & 0 & -\frac{r\mu_s}{\rho_s Re} & 0 & 0 & 0 \\ 0 & 0 & 0 & 0 & 0 & 0 \\ 0 & 0 & 0 & 0 & 0 & 0 \end{bmatrix}$$

$$H_{10} = \begin{bmatrix} 0 & 0 & 0 & 0 & 0 & 0 \\ 0 & 0 & 0 & 0 & 0 & 0 \\ 0 & 0 & 0 & 0 & 0 & 0 \\ 0 & 0 & 0 & 0 & 0 & 0 \\ 0 & 0 & 0 & 0 & 0 & 0 \\ 0 & 0 & 0 & 0 & 0 & 0 \end{bmatrix}$$

$$H_{11} = \begin{bmatrix} 0 & 0 & 0 & 0 & 0 & 0 \\ 0 & -\frac{1}{\mu_s} \frac{\partial \mu_s}{\partial y} & 0 & 0 & \frac{2(\gamma-1)M^2}{\mu_s} \frac{\partial \mu_s}{\partial y} \frac{\partial U_s}{\partial y} + 2(\gamma-1)M^2 \frac{\partial^2 U_s}{\partial y^2} & 2(\gamma-1)M^2 \frac{\partial U_s}{\partial y} \\ 0 & 0 & 0 & 0 & 0 & 0 \\ \frac{\partial U_s}{\partial y} & 0 & 0 & 0 & \frac{\partial T_s}{\partial y} & 0 \\ 0 & 0 & 0 & 0 & 0 & 0 \\ 0 & \frac{Pr}{\mu_s} \frac{\partial \mu_s}{\partial \theta} \frac{\partial U_s}{\partial y} & 0 & 0 & -\frac{(\gamma-1)M^2 Pr}{\mu_s} \frac{\partial \mu_s}{\partial \theta} \left(\frac{\partial U_s}{\partial y}\right)^2 & -\frac{1}{\mu_s} \frac{\partial \mu_s}{\partial y} + \frac{1}{\mu_s} \frac{\partial \mu_s}{\partial \theta} \frac{\partial T_s}{\partial y} \end{bmatrix}$$

H_2

$$= \begin{bmatrix} 0 & 0 & 0 & 0 & 0 & 0 \\ \frac{Re}{\mu_s} \rho_s U_s & 0 & -\frac{1}{\mu_s} \frac{\partial \mu_s}{\partial y} & \frac{\rho_s Re}{\mu_s} & 0 & 0 \\ 1 & 0 & 0 & \frac{\rho_s U_s}{P_s} & U_s & 0 \\ \frac{r+m}{\rho_s Re} \frac{\partial \mu_s}{\partial y} & \frac{\mu_s}{\rho_s Re} (m+r+1) & -U_s & \frac{r U_s}{P_s Re} \frac{\partial \mu_s}{\partial y} & \frac{-2(\gamma-1)M^2 \mu_s}{\rho_s Re} \frac{\partial U_s}{\partial y} + \frac{r U_s}{\rho_s Re} \frac{\partial \mu_s}{\partial y} & \frac{r U_s \mu_s}{\rho_s Re} \\ 0 & 0 & 0 & 0 & 0 & 0 \\ 0 & 0 & Pr \frac{\partial \mu_s}{\partial \theta} \frac{\partial U_s}{\partial y} & -\frac{Pr Re \rho_s U_s}{T_s \mu_s} & \frac{Pr Re \rho_s}{\mu_s} U_s & 0 \end{bmatrix}$$

$$H_3 = \begin{bmatrix} 0 & 0 & 0 & 0 & 0 & 0 \\ 0 & 0 & -(m+1) & 0 & 0 & 0 \\ 0 & 0 & 0 & 0 & 0 & 0 \\ 0 & 0 & 0 & \frac{r U_s \mu_s}{P_s Re} & 0 & 0 \\ 0 & 0 & 0 & 0 & 0 & 0 \\ 0 & 0 & 0 & 0 & 0 & 0 \end{bmatrix}$$

$$H_4 = \begin{bmatrix} 0 & 0 & 0 & 0 & 0 & 0 \\ -r & 0 & 0 & 0 & 0 & 0 \\ 0 & 0 & 0 & 0 & 0 & 0 \\ 0 & 0 & \frac{\mu_s}{\rho_s Re} & 0 & 0 & 0 \\ 0 & 0 & 0 & 0 & 0 & 0 \\ 0 & 0 & 0 & 0 & -1 & 0 \end{bmatrix}$$

$$H_0^T \begin{bmatrix} 0 & 1 & 0 & 0 & 0 & 0 & 0 & 0 & 0 \\ \frac{Re}{\mu_s T_s} \alpha^2 + i\alpha U_s & \frac{-D\mu_s}{\mu_s} & i\alpha \left(\frac{-D\mu_s}{\mu_s} \right) & i\alpha \frac{\rho_s Re}{\mu_s} + \alpha^2 (1+m) \frac{\rho_s U_s}{P_s} & \frac{2(\gamma-1)M^2 D\mu_s D U_s}{\mu_s} + 2(\gamma-1)M^2 D^2 U_s + \alpha^2 (1+m)U_s & 2(\gamma-1)M^2 D U_s \\ i\alpha & 0 & 0 & i\alpha \frac{\rho_s U_s}{P_s} & i\alpha U_s & 0 \\ \frac{i\alpha}{\rho_s Re} (r+m)D\mu_s & i\alpha \frac{\mu_s}{\rho_s Re} (r+m+1) & -i\alpha U_s - \alpha^2 \frac{\mu_s}{\rho_s Re} & \frac{i\alpha}{P_s} \frac{r U_s}{D_s Re} D\mu_s & \frac{D T_s + i\alpha \left[\frac{-2(\gamma-1)M^2}{\rho_s Re} D U_s \mu_s + \frac{r U_s}{\rho_s Re} D \mu_s \right]}{\mu_s} & \frac{i\alpha}{P_s} \frac{r U_s \mu_s}{\rho_s Re} \\ \chi & \chi & \chi & \chi & \chi & \chi \\ 0 & 0 & 0 & 0 & 0 & 0 \\ 0 & \frac{Pr}{\mu_s} D U_s & i\alpha Pr \mu_s D U_s & \frac{-i\alpha Re \rho_s U_s}{T_s \mu_s} & -\frac{(\gamma-1)M^2 Pr \mu_s (D U_s)^2}{\mu_s} + i\alpha \frac{Re Pr \rho_s U_s}{\mu_s} + \alpha^2 & \frac{D\mu_s}{\mu_s} (-1 + DT_s) \end{bmatrix}$$

III The boundary layer properties U_s , T_s , and μ_s and their derivatives in matrix H_0 in section 6.6.1

$$U_s = -2.2105y^3 + 2.491y^2 + 0.7292y - 0.0531$$

$$\frac{\partial U_s}{\partial y} = \frac{13263}{2000}y^2 + \frac{2491}{500}y + \frac{1823}{2500}$$

$$\frac{\partial^2 U_s}{\partial y^2} = \frac{2491}{500} - \frac{13263}{1000}y$$

$$T_s = 1 + (\gamma - 1) \frac{M^2}{2} \left[1 - \left(-\frac{4421}{2000}y^3 + \frac{2491}{1000}y^2 + \frac{1823}{2500}y - \frac{531}{10000} \right)^2 \right]$$

$$\frac{\partial T_s}{\partial y} = -\frac{5 \left(-\frac{13263}{2000}y^2 + \frac{2491}{500}y + \frac{1823}{2500} \right) \left(-\frac{4421}{2000}y^3 + \frac{2491}{1000}y^2 + \frac{1823}{2500}y - \frac{531}{10000} \right)}{2}$$

$$\mu_s = \frac{-729 \left[\frac{9}{4} - \frac{5 \left(-\frac{4421}{2000}y^3 + \frac{2491}{1000}y^2 + \frac{1823}{2500}y - \frac{531}{10000} \right)^2}{4} \right]^{\frac{3}{2}}}{500 \left[\frac{5 \left(-\frac{4421}{2000}y^3 + \frac{2491}{1000}y^2 + \frac{1823}{2500}y - \frac{531}{10000} \right)^2}{4} - \frac{2253}{20} \right]}$$

$$\frac{\partial \mu_s}{\partial y}$$

$$= \frac{10935 \left[\frac{9}{4} - \frac{5 \left(-\frac{4421}{2000}y^3 + \frac{2491}{1000}y^2 + \frac{1823}{2500}y - \frac{531}{10000} \right)^2}{4} \right]^{\frac{1}{2}} \left(-\frac{13263}{2000}y^2 + \frac{2491}{500}y + \frac{1823}{2500} \right) \left(-\frac{4421}{2000}y^3 + \frac{2491}{1000}y^2 + \frac{1823}{2500}y - \frac{531}{10000} \right)}{4 \left[625 \left(-\frac{4421}{2000}y^3 + \frac{2491}{1000}y^2 + \frac{1823}{2500}y - \frac{531}{10000} \right)^2 - 56325 \right]}$$

$$+ \frac{911250 \left[\frac{9}{4} - \frac{5 \left(-\frac{4421}{2000}y^3 + \frac{2491}{1000}y^2 + \frac{1823}{2500}y - \frac{531}{10000} \right)^2}{4} \right]^{\frac{3}{2}} \left(-\frac{13263}{2000}y^2 + \frac{2491}{500}y + \frac{1823}{2500} \right) \left(-\frac{4421}{2000}y^3 + \frac{2491}{1000}y^2 + \frac{1823}{2500}y - \frac{531}{10000} \right)}{\left[625 \left(-\frac{4421}{2000}y^3 + \frac{2491}{1000}y^2 + \frac{1823}{2500}y - \frac{531}{10000} \right)^2 - 56325 \right]^2}$$

$$\frac{\partial \mu_s}{\partial \theta} = \frac{(2187\sqrt{T_s})}{1000(T_s + \frac{552}{5})} - \frac{(729T_s^{\frac{3}{2}})}{500(T_s + \frac{552}{5})^2}$$

References

- ¹ Lin, J. C. "Review of Research on Low-Profile Vortex Generators to Control Boundary Layer Separation," *Progress in Aerospace Science*, Vol. 38, 2002, pp. 389-420.
- ² Lu, F. K., Li, Q., Shih, Y., Pierce, A. J. and Li, C., "Review of Micro Vortex Generators in High-Speed Flow," AIAA paper 2011-0031, 2011.
- ³ Lim, T. T., "On the Role of Kelvin–Helmholtz-Like Instability in the Formation of Turbulent Vortex Rings," *Fluid Dynamics Research*, Vol. 21, No.1, 1997, pp. 47–56.
- ⁴ Pierce, A. J., "Experimental Study of Micro-Vortex Generators at Mach 2.5," MSAE thesis, University of Texas at Arlington, 2010.
- ⁵ Anderson, B. H., Tinapple, J. and Surber, L., "Optimal Control of Shock Wave Turbulent Boundary Layer Interactions Using Micro-Array Actuation," AIAA paper 2006-3197, 2006.
- ⁶ Pitt Ford, C. W. and Babinsky, H., "Micro-Ramp Control for Oblique Shock Wave / Boundary Layer Interactions," AIAA paper 2007-4115, 2007.
- ⁷ Carpenter, P. W. and Tabakoff, W., "Survey And Evolution of Supersonic Base Flow Theories," The Institute of Space Sciences University of Cincinnati, Ohio, October 1968.
- ⁸ Herrin, J. L., Dutton, J. C., "Supersonic base flow experiments in the near wake of a cylindrical afterbody," *AIAA Journal*, Vol. 32, No. 1, 1994, pp. 77-83.
- ⁹ Anderson, J. D., "Modern compressible flow with historical perspective," McGraw-Hill Professional, 2003.
- ¹⁰ Simon, F., Deck, S., Guillen, P., Sagaut, P., "Hybrid RANS/LES Simulations of Supersonic Base Flow," *Symposium on hybrid RANS-LES Methods*, Stockholm, July 2005.

- ¹¹ Babinsky, H., Li, Y., and Pitt Ford, C. W., "Microramp Control of Supersonic Oblique Shock-Wave/Boundary-Layer Interactions," *AIAA Journal*, Vol. 47, No. 3, 2009, pp. 668–675.
- ¹² Pierce, A. J., Lu, F. K., Bryant, D. S., and Shih, Y., "New Developments in Surface Oil Flow Visualization," AIAA paper 2010-4353, 2010.
- ¹³ Fedorov, A., Tumin, A., "Initial-Value Problem for Hypersonic Boundary-Layer Flows," *AIAA Journal*, Vol. 41, No. 3, March 2003, pp. 379–389.
- ¹⁴ Grosch, C. E., Salwen, H., "The continuous spectrum of the Orr-Sommerfeld equation. Part 1. The spectrum and the eigenfunctions," *Fluid Mechanics Journal*, Vol. 87, Part 1, 1978, pp. 33–54.
- ¹⁵ Denissen, A. N., "Roughness-induced Transient Growth: Continuous-spectrum Receptivity and Secondary Instability Analysis," Ph.D dissertation, Texas A&M University, May 2011.
- ¹⁶ Denison, Marie F.C., "Compressibility Effects On The Non-linear Receptivity Of Boundary Layers To Dielectric Barrier Discharges," MSAE thesis, University of Texas at Arlington, May 2013.
- ¹⁷ Barone, F. M., "Receptivity of Compressible Mixing Layers," Ph.D dissertation, Stanford University, May 2003.
- ¹⁸ Shih, Yusi, "Mean Pressure Measurements of Micro-Vortex Generator at Mach 2.5," MSAE thesis, University of Texas at Arlington, Fall 2010.
- ¹⁹ Li, Q. and Liu, C., "LES for Supersonic Ramp Control Flow Using MVG at $M = 2.5$ and $Re_\theta = 1440$," AIAA Paper 2010–0592, 2010.
- ²⁰ Blinde, P. L., Humble, R. A., van Oudheusden, B. W., and Scarano, F., "Effects of Micro-Ramps on a Shock Wave/Turbulent Boundary Layer Interaction," *Shock Waves*, Vol. 19, No. 6, 2009, pp. 507–520.

Biographical Information

Yusi Shih was born in a traditional family in Taiwan. He likes to spend time with friends, meet new people, and travel around the world. He is also a fan of Bill Gates, Albert Einstein, and Scarlett Johansson. The subject theoretical physics was his dream career. Now, he is interested in space explorations and hope that he can participate in it as soon as possible for his life career.